UNIVERSITY OF SOUTHAMPTON

FACULTY OF NATURAL AND ENVIRONMENTAL SCIENCES

Chemistry

Exploring Heterogeneous Bimetallic Nanoparticle Catalysts for Sustainable Oxidations

by

Sivan Van Aswegen

Thesis for the degree of Master of Philosophy

March 2017

UNIVERSITY OF SOUTHAMPTON

ABSTRACT

FACULTY OF NATURAL AND ENVIRONMENTAL SCIENCES

Chemistry

Thesis for the degree of Master of Philosophy

EXPLORING HETEROGENEOUS BIMETALLIC NANOPARTICLE CATALYSTS FOR SUSTAINABLE OXIDATIONS

by Sivan Van Aswegen

Prior work in the group has focused on developing the synthesis and activation of supported monometallic noble metal nanoparticle (Au, Pt and Pd) copper chlorophosphate frameworks (CuClPs), and exploring their potential as oxidation catalysts. Herein, bimetallic variants (AuPt/CuClP, PtPd/CuClP and AuPd/CuClP) have been synthesised, characterised and employed in catalytic reactions. Characterisation by TEM and XPS revealed the presence of small, metallic nanoparticles in the bimetallic CuClP materials, with the AuPt/CuClP sample containing the smallest and most uniform particles. The bimetallic AuPt/CuClP material was found to be highly active in the aerobic oxidation of KA-oil, with the catalyst reduced at 300 °C giving the most promising result (89 mol % conversion, > 99 % selectivity to cyclohexanone). The AuPt/CuClP catalyst reduced at 300 °C showed the most promise, achieving the highest conversion of the monometallic and bimetallic CuClP catalysts, while also showing an increased stability over a range of temperatures compared to the monometallic analogues. Through physical mixture tests, the nature of the bimetallic nanoparticles in the AuPt/CuClP catalyst reduced at 250 °C was probed and predicted to contain discrete sites, however the increased thermal stability of the AuPt/CuClP reduced at 300 °C alluded to a synergistic interaction between the Au and Pt species, suggesting the possibility of alloyed nanoparticle sites.

The catalytic potential of the CuClP materials was further explored in the oxidation of valerolactam, the hydrogenation of furfural, the Beckmann rearrangement of cyclohexanone oxime, and the Baeyer-Villiger oxidation of cyclohexanone. However, the presence of unexpected acid-catalysed products gave rise to the consideration of the inclusion of weak Lewis acid sites in the CuClP framework, although acid characterisation is required in order to confirm this.

Table of Contents

List of Tables

List of Figures

List of Equations

DECLARATION OF AUTHORSHIP

I, ...

declare that this thesis and the work presented in it are my own and has been generated by me as the result of my own original research.

.....

.....

I confirm that:

1. This work was done wholly or mainly while in candidature for a research degree at this University;
2. Where any part of this thesis has previously been submitted for a degree or any other qualification at this University or any other institution, this has been clearly stated;
3. Where I have consulted the published work of others, this is always clearly attributed;
4. Where I have quoted from the work of others, the source is always given. With the exception of such quotations, this thesis is entirely my own work;
5. I have acknowledged all main sources of help;
6. Where the thesis is based on work done by myself jointly with others, I have made clear exactly what was done by others and what I have contributed myself;
7. None of this work has been published before submission.

Signed: .....

Date:.....

Acknowledgements

I would like to take a moment to acknowledge all of the people who have given their time and experience to help me along the way with this work. First and most importantly, I would like to thank my supervisor, Dr Robert Raja, whose guidance and endless new ideas have been a strong driving force. His understanding and support over the last few weeks has been particularly evident, for which I am very grateful. I would also like to thank my industrial sponsors, Dr Alan Levy and Dr Scott Keenan, and the rest of the Honeywell team for all of their insight, helpful suggestions, and funding. This project would not have taken off, were it not for you all, so thank you!

The Raja group deserve a huge shout out, as these fantastic people are what makes the experience. I would particularly like to thank Dr Matthew Potter for being my mentor and my closest friend. His advice and support has been instrumental in my development as a chemist, and his expert knowledge he was always happy to lend. All of his guidance, in every respect, has been so important to me, and for that, I am so thankful! I would also like to thank Arran Gill, who took me under his wing towards the beginning of my project, for helping me find my feet. Your insight to the project was incredibly helpful, and our discussions were valued greatly. Further thanks goes to Stephanie Newland for always being happy to help and for putting up with my endless stream of questions, and William Webb for his help and ability to bounce ideas between. I am also very thankful for the hard work of my two project students, Tammy Nimmo and Jack Parsons. Your extra pair of hands was much appreciated. Thank you to the rest of the Raja group for all of the good times: Chris H, Thomas, Steph C, Angnieszka, Elpi, Danni, Cameron, Natalie, Allison, Ioli and Paven.

Lastly, I would like to thank the help of all of my collaborators: Dr Mark Light, Dr Neil Wells and Julie Herniman from the University of Southampton, Dr Gillian Collins from University College Cork, Dr Georgious Kyriakou from Aston University, Dr Peter Wells, Dr Emma Gibson and Scott Rogers from the Research Complex at Harwell.

Definitions and Abbreviations

AC-STEM – aberration-corrected scanning transmission electron microscopy

ADF – annular dark-field

AlPO – aluminophosphate

BET – Brunauer-Emmett-Teller

CuClP – copper chlorophosphate

DRIFTS – diffuse reflectance infrared Fourier transform spectroscopy

EDX – energy-dispersive X-ray spectroscopy

EXAFS – extended X-ray absorption fine structure spectroscopy

FID – flame ionisation detector

FTIR – Fourier transform infrared spectroscopy

GC – gas chromatography

HP – hierarchically porous

KA-oil – ketone-alcohol oil, a mixture of cyclohexanone and cyclohexanol

NP – nanoparticle

PXRD – powder X-ray diffraction

SAPO – silicon aluminophosphate

SEM – scanning electron microscopy

SM – starting material

TEM – transmission electron microscopy

TOF – turnover frequency

TON – turnover number

TPD – temperature programmed desorption spectroscopy

TPR – temperature programmed reduction spectroscopy

UV-Vis – ultraviolet-visible spectroscopy

VOC – volatile organic compound

WHSV – weight hourly space velocity

XAS – X-ray absorption spectroscopy

XPS – X-ray photoelectron spectroscopy

Chapter 1: Introduction

1.1 Sustainable Chemistry

The chemical industry forms an integral part of the modern global economy; the discovery of new medicines and vaccines has significantly improved the quality of life, while technical advances have led to the development of new materials for manufacture and construction. However despite the benefits provided by the chemical industry it is often negatively associated with pollutants and chemical waste, causing environmental damage and serious health problems. The industry's reliance on fossil fuels and high energy inputs also poses a problem, and as a result the development of sustainable chemical processes is of paramount importance. The notion of 'green chemistry' was established in 1998 by Paul Anastas and John Warner as an approach to carrying out chemistry in a sustainable manner without adverse environmental side effects, and the twelve principles are highlighted in Table 1.1[1].

1	Waste prevention instead of remediation
2	Atom efficiency
3	Lass hazardous/toxic chemicals
4	Safer products by design
5	Innocuous solvents and auxiliaries
6	Energy efficient by design
7	Preferably renewable raw materials
8	Shorter syntheses (avoid derivation)
9	Catalytic rather than stoichiometric reagents
10	Design products for degradation
11	Analytical methodologies for pollution prevention
12	Inherently safer processes

Table 1.1: Twelve principles of green chemistry.

The idea of green chemistry represents the importance of carrying out chemical design, manufacture and disposal avoiding the use or generation of hazardous substances, and hence replacing environmentally impacting chemical processes with less polluting alternatives. This can be achieved by the design of processes to be energy efficient, to maximise atom economy, to utilise benign reagents and solvents, and to minimise waste production. This necessary quest for sustainable chemical processes can be realised through the utilisation of catalysis; a fundamental part of chemistry that is intrinsically linked with green chemistry, through providing lower energy pathways, or by improving the selectivity profile for reactions.

1.1 Catalysis

Catalysis is of fundamental importance to the modern chemical industry, with over 90 % of all manufacturing processes employing catalysts at some stage[2]. Shriver and Atkins defines a catalyst as "a substance that increases the rate of a reaction but is not itself consumed"[3], and goes on to highlight that catalysts are playing an increasing role in achieving a cleaner environment, through the destruction of pollutants, such as in the utilisation of carbon dioxide[4], and the development of more efficient industrial processes.

The rate at which any given reaction will proceed by is determined by both kinetics and thermodynamics, and the reaction progression is determined by the Gibbs free energy (ΔG), as shown by Equation 1.1.

$$\Delta G = \Delta H - T\Delta S$$

Equation 1.1: Gibbs free energy equation, where H is enthalpy (kJ mol^{-1}), T is temperature (K), S is entropy (kJ mol^{-1} K^{-1}), and G is Gibbs free energy (kJ mol^{-1}).

In order for a process to be thermodynamically favoured, the Gibbs free energy for the reaction must be negative. In addition to this, a reaction also needs to overcome an energy barrier in order to progress, and as such, the kinetics of a reaction is inherently linked to the activation energy, E_A. It is worth noting that a catalyst cannot affect the position of equilibrium as this is under thermodynamic control, however it does affect the rate at which it is achieved. A catalyst works by providing an alternative reaction pathway, thus lowering the activation energy of a process with respect to the uncatalysed reaction, as shown by the blue and red profiles in Figure 1.1.

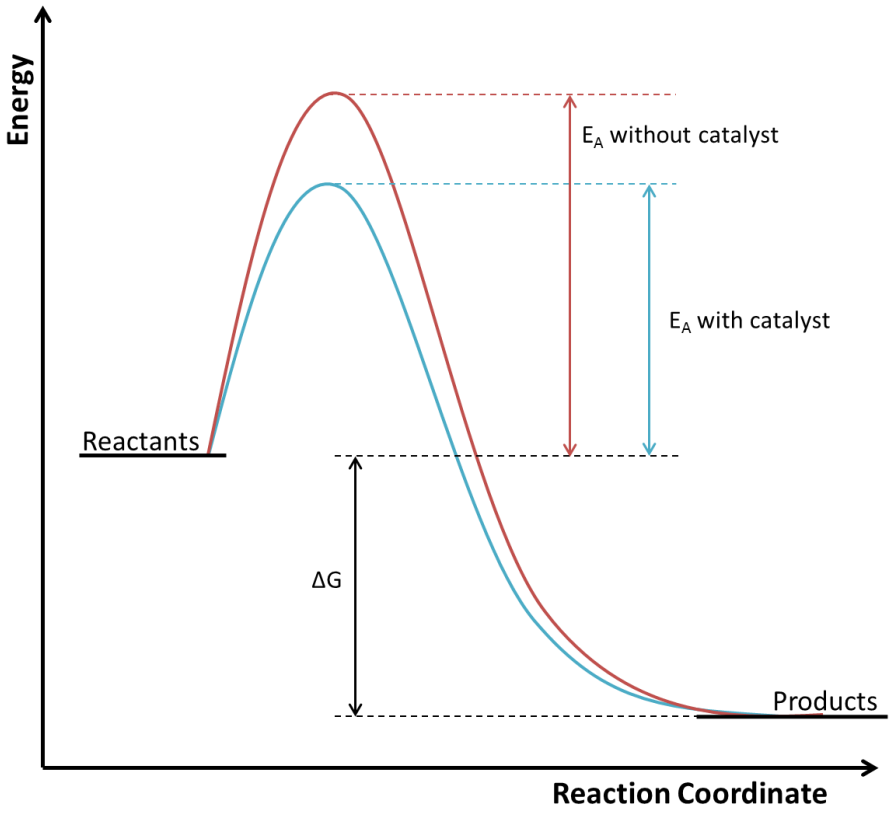

Figure 1.1: Energy level diagram for a reaction showing the catalysed (blue) and uncatalysed (red) pathways.

Masel[5] details that the activation energy of a process can be reduced in a variety of different ways, by designing catalysts to help initiate reactions, to stabilise intermediates, or to hold reactants in close proximity. Catalysts can also be designed to block side reactions, improving the overall selectivity of a process towards the desired product.

There are two distinct types of catalysts: heterogeneous, where the catalyst is in a different phase to the reaction medium, and homogeneous, where the catalyst is in the same phase. The use of homogeneous catalysts is attractive as they often achieve very high activities due to lesser mass transfer restrictions. However, despite the often improved activity of homogeneous catalysts, they require separation steps in order to remove them from the product, often rendering the process less environmentally friendly and more costly than heterogeneous catalysis. As a result, heterogeneous catalysis is often more favourable. Examples of industrial heterogeneous catalysis include the Haber process for the production of ammonia using metallic iron with small quantities of potassium salts on an alumina support, and the Contact process using vanadium (V) oxide in the manufacture of sulfuric acid[6].

1.2 Supported Nanoparticles in Catalysis

Many heterogeneous catalysts rely on surface interaction in order to function, and as such a large available surface area, giving rise to more sites for adsorption and reaction, is key. A catalyst can be designed to have a large surface area in two distinct ways. Firstly, the catalyst can be made porous in nature, allowing substrates to gain access to an internal as well as an external surface area. Secondly, one can maximise the surface area to volume ratio of the catalyst, often achieved by making the particles as small as possible. If these strategies are performed on the nanoscale, then high surface area nanomaterials can be created.

Nanoparticles are defined by having one or more dimensions in the nanometre size range (1 – 100 nm)[7], and are often, but not exclusively, nanometre sized metallic clusters dispersed within a porous matrix. There is huge scope for the use of supported metallic nanoparticles in a variety of different applications, including gene delivery[8], antimicrobial wound dressings[9], glucose biosensors[10], hydrogen sorption materials for fuel cells[11], and catalysis[12]. Noble metal nanoparticles have been of particular interest in the area of catalysis, with a particular focus on oxidation, hydrogenation and C-C coupling reactions. Qualitative examples of metal nanoparticles used in catalysis are exhibited in Table 1.2 below.

Table 1.2: Examples of catalytic transformations using monometallic nanoparticles.

Metal	Process	Substrate	Ref.
Pt	Oxidation	Carbon Monoxide	[13,14]
		Benzylic Alcohols	[15]
		VOCs	[14]
		D-Glucose	[14]
	Hydrogenation	Ethylene	[16]
		Propyne	[17]
		Chloronitrobenzene	[18]
		Benzene	[19]
		Toluene	[14]
	Dehydrogenation	Propane	[14,20,21]
		Ethane	[22]
		Cyclohexane	[23]

Au	Oxidation	Benzyl Alcohol Cinnamyl Alcohol Carbon Monoxide Hydrogen	[24,25] [25] [26–28] [12]
	Epoxidation	Propylene	[29]
	Hydrogenation	Butadiene Acetylene	[30] [31]
Pd	Oxidation	Benzyl Alcohol 1-Phenylethanol	[32] [33]
	Hydrogenation	Olefins	[34]
	C-C Coupling	Suzuki Cross Coupling C2 Arylation of Indoles	[35] [36]
Rh	Oxidation	Propylene	[37]
	Hydrogenation	Cyclohexene Benzene	[38] [38]
Ag	Oxidation	Benzyl Alcohol	[24]
	C-C Coupling	A3 Coupling	[39]
Ni	Hydrogenation	Crotonaldehyde	[40]
Ru	Oxidation	Ethanol VOCs	[41] [42]
Co	Formylation	1-Octene	[11]
Cu	Oxidation	Phenol	[43]
	Hydrogenation	Cyclooctene	[44]

VOCs = volatile organic compounds.

As well as monometallic nanoparticles, bimetallic variants have also received a lot of interest, with key qualitative examples shown in Table 1.3 below.

Table 1.3: Examples of catalytic transformations using bimetallic nanoparticles.

Metal	Process	Substrate	Ref.
AuPt	Selective Sensor	NO_X	[45]
	Electrooxidation	Methanol	[46]
		Glucose	[47]
	Electroreduction	Oxygen	[48]
	Water-Gas Shift	Carbon Monoxide	[49]
PtPd	Oxidation	Carbon Monoxide	[50]
	Hydrogenation	Toluene	[51]
		Naphthalene	[52]
AuPd	Oxidation	Benzyl Alcohol	[53,54]
		Cinnamyl Alcohol	[54]
		Hydrogen	[55]

Nanoparticles are of interest due to their differing physicochemical properties compared to their bulk counterparts. Bulk metals are typically ductile, having high electrical and thermal conductivities due to electron delocalisation within the bulk material, however these properties are not typically seen in metal nanoparticles as this delocalisation is not observed. These changes in properties are known as quantum size effects and they are most noticeable when particle sizes fall below 10 nm. The effects arise from the narrowing of the conduction and valence bands in very small particles, producing a gap between them and hence causing metallic behaviour to be lost[56]. As such, nanoparticles tend to be highly active centres which are thermodynamically unstable due to a combination of their high surface energy and large surface areas, and so have a tendency to agglomerate into larger particles over time.

In order to produce small and stable nanoparticles it is necessary to stabilise the particles by either coating the surface in surfactant (e.g. thiols[57,58]) and polymers (polyvinylpyrrolidone (PVP)[16], polyvinyl alcohol (PVA)[59], etc.), or to immobilise them on porous materials[15,60]. Surfactants act to cover the surface using micelle-like behaviour and can prevent particle growth from continuing past a certain size, the dimensions of which can be controlled by the concentration of surfactant. The

size of nanoparticles can also be controlled by limiting particle growth to a particular size regime through immobilisation on porous supports with defined pore sizes, which also acts to reduce particle aggregation. Typically metallic nanoparticles are supported on dense phase oxidic supports, such as silica[61], alumina[37], titania[26] and ceria[62] owing to their high thermal and chemical stabilities, moderate surface areas, and ease of preparation and further functionalisation, however there has recently been a drive towards supporting nanoparticles on nanoporous materials due to their increased surface areas and porous natures. Typical nanoparticle syntheses exploit the two methods of stabilisation mentioned above, with the most common syntheses being impregnation[63], deposition-precipitation[64] and colloidal deposition[65].

Impregnation is perhaps the simplest approach, involving the wetting of the solid support with a solution containing the metal precursor. The material is then dried and subsequently thermally treated by reduction under hydrogen to form metal nanoparticles. Typically, nanoparticles produced by this method tend to have a broad size distribution and can be difficult to tune to a particular size regime due to poor control over nanoparticle growth and as a result of the increased chance of nanoparticle sintering at elevated temperatures. The use of the deposition-precipitation method bypasses the problems of thermal reduction, and involves adjusting the pH of a solution containing the metal precursor and the support through the addition of hydroxide. This addition achieves complete precipitation of the metal hydroxide, which is subsequently deposited onto the surface of the support, which acts as a nucleating agent[66]. Despite avoiding the problems associated with thermal reduction, this method has been reported to induce the collapse of fragile supports due to the high surface tension of the liquid solutions used[67]. Colloidal deposition entails the pre-formation of metal nanoparticles as a colloid in solution, most commonly through the use of polymer stabilising agents, followed by deposition onto a support. The formation of nanoparticles before deposition allows a greater control of their size through the use of stabilising agents, and so is synthetically more useful; however these stabilisers remain on the surface of the nanoparticles after synthesis, and as such can block potential adsorption sites for catalysis. Less common nanoparticle synthesis methods include physical methods such as ultrasound sonication[68], microwave irradiation[27] and pulsed laser ablation[28]. Recently, a novel nanoparticle synthesis approach has been reported wherein $[AuCl_4]^-$ anions were found to be extruded out of the channels of a copper chlorophosphate framework on calcination[69], with further characterisation by Hinde *et al.* proving this extrusion to be a novel method for the generation of gold nanoparticles with a size distribution of 2 – 10 nm[70].

1.3 Copper Chlorophosphates

Copper chlorophosphates are part of a family of microporous (pore diameter < 2 nm) framework materials possessing CU-2 topology, first being reported in 1999 by Huang *et al.*[71]. These frameworks have the general formula $[A_XCu_6(P_2O_7)_4Cl_Y].[MX_4]$ (A = K, Rb, Cs, $[NH_4]$; M = Cu, Au, Pt, Pd; X = Cl, Br) and were initially synthesised using molten salt templating methods at temperatures between 500 – 800 °C.

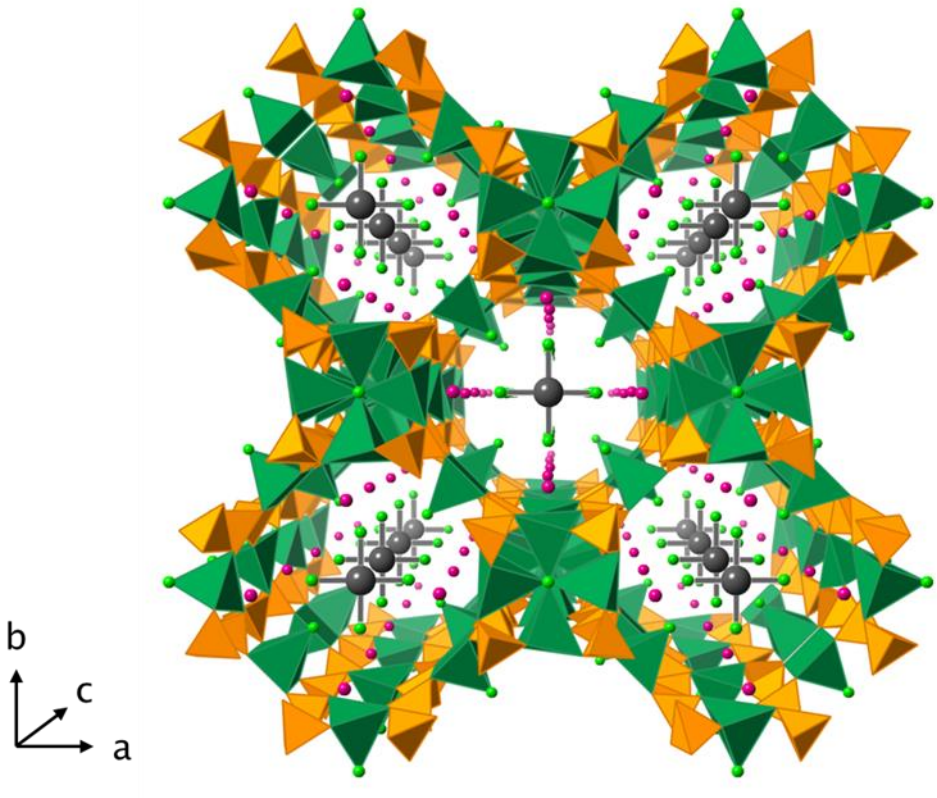

Figure 1.2: Crystallographic representation of the CU-2 topology of the $[A_XCu_6(P_2O_7)_4Cl_Y].[MX_4]$ copper chlorophosphate framework reproduced from Hinde *et al.*[72] (Cu – green polyhedra, P – orange polyhedra, M – grey spheres, Cl – green spheres, A – pink spheres; oxygen omitted for clarity).

The crystal structure of the CU-2 framework of copper chlorophosphate is shown in Figure 1.2 and is composed of a μ^4 chloride ion (green spheres) connecting four CuO_4 tetrahedra (green polyhedra), which are linked by pyrophosphate, P_2O_7, groups (orange polyhedra) and square planar CuO_4 groups (green polyhedra) to form 1D chains. These chains are cross-linked by further P_2O_7 and square planar CuO_4 groups to form a square grid with 1D channels ca. 12.7 Å in diameter. The copper chlorophosphates are a series of complex anion-inclusion compounds that contain weakly

coordinated square planar MCl_4 groups (e.g. $[CuCl_4]^-$) that stack neatly on one another in the 1D channels. The MCl_4 groups are surrounded by cations (A) within the channel, which have a weak interaction with the MCl_4 groups and the negatively charged framework. It has been hypothesised that this salt lattice acts as a templating agent for the inorganic framework[71], and as such this template can be removed leaving the framework intact, although some A cations will remain in order to balance the negatively charged framework.

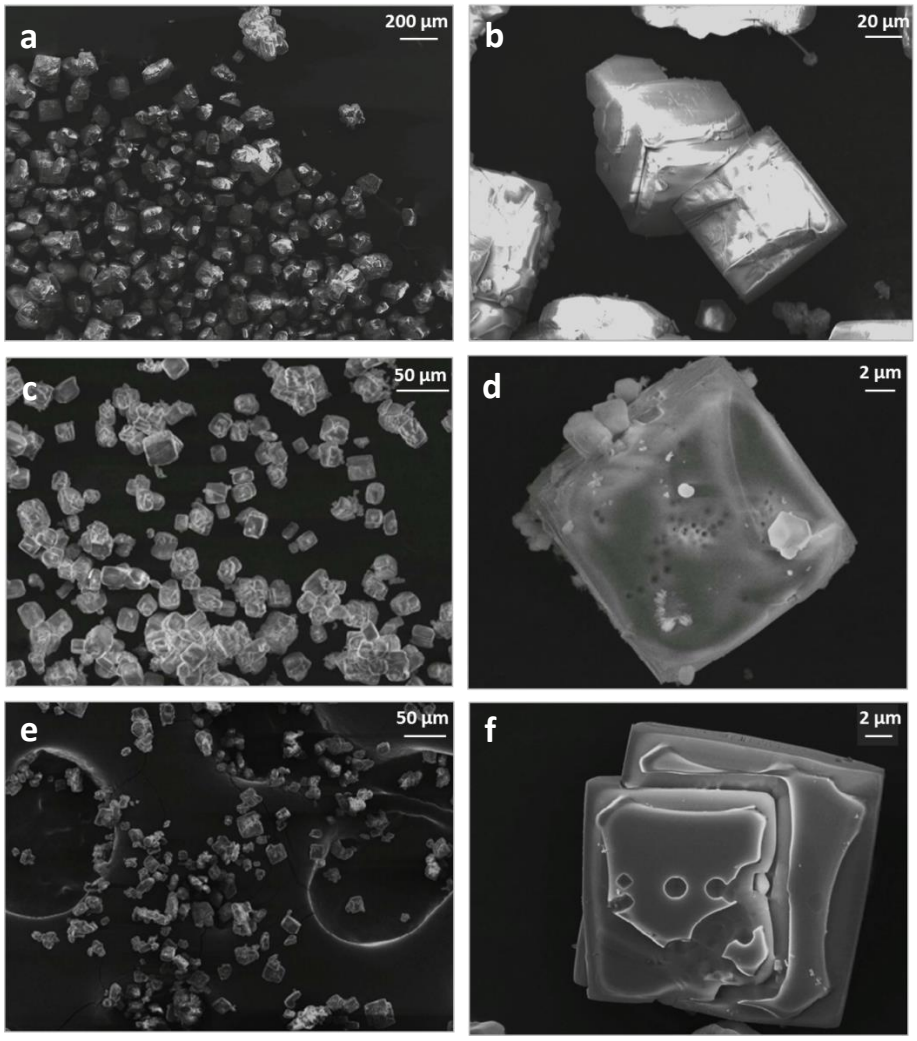

Figure 1.3: SEM micrographs of as-synthesised $[AuCl_4]^-$ supported (a – b), $[PtCl_4]^{2-}$ supported (c – d) and $[PdCl_4]^{2-}$ supported (e – f) copper chlorophosphates.

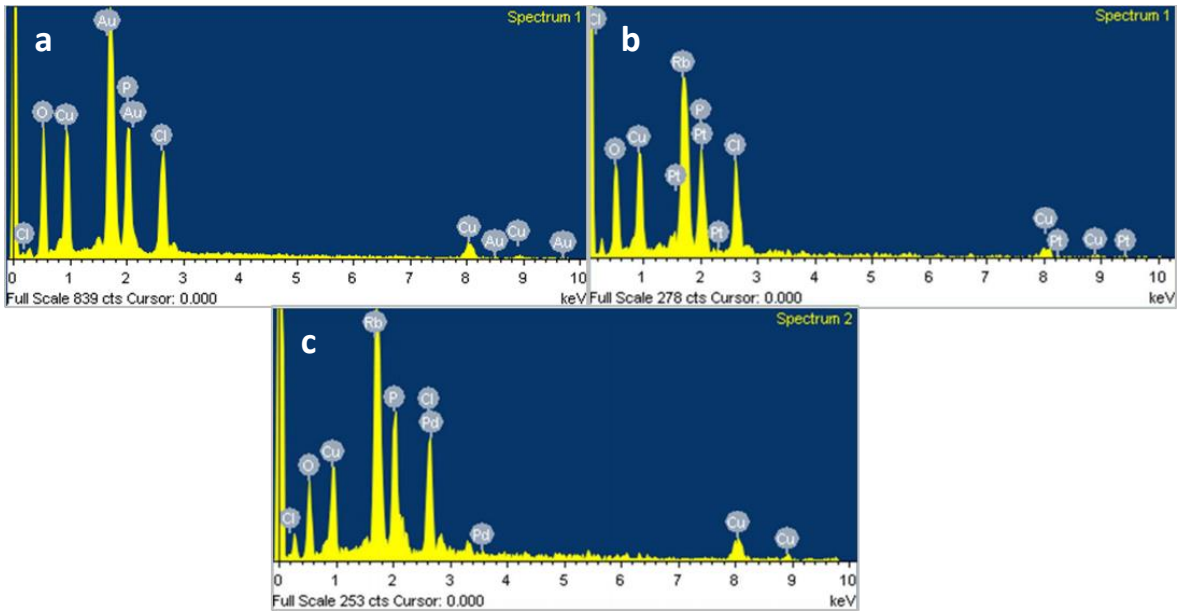

Figure 1.4: EDX spectra of as-synthesised $[AuCl_4]^-$ supported (a), $[PtCl_4]^{2-}$ supported (b) and $[PdCl_4]^{2-}$ supported (c) copper chlorophosphates.

Recent developments by Williams *et al.*[69] facilitated the first hydrothermal syntheses of the copper chlorophosphate materials, greatly reducing the temperatures at which the materials could be synthesised. The work was successful in synthesising the K, Rb and Cs analogues of the framework, as well as demonstrating that complex anions such as $[AuCl_4]^-$, $[PtCl_4]^{2-}$ and $[PdCl_4]^{2-}$ could be incorporated into the channels. A further study found that calcination of the $[AuCl_4]^-$ doped framework caused the $[AuCl_4]^-$ anions to be ejected from the channels, as confirmed by the loss of electron density observed through single crystal x-ray diffraction. Later, Hinde *et al.*[70] found this calcination process to be a novel means for depositing gold nanoparticles onto the surface of the copper chlorophosphate support, and subsequently extended this procedure to Pt and Pd analogues with similar success. Initial characterisation by scanning electron microscopy (SEM) displayed the homogeneous crystal morphologies for all three samples, as shown in Figure 1.3, while energy-dispersive X-ray spectroscopy (EDX) confirmed the presence of the noble metals, as shown in Figure 1.4. Transmission electron microscopy (TEM) characterisation proved these nanoparticles to be within the range of 2 – 10 nm, as shown in Figure 1.5.

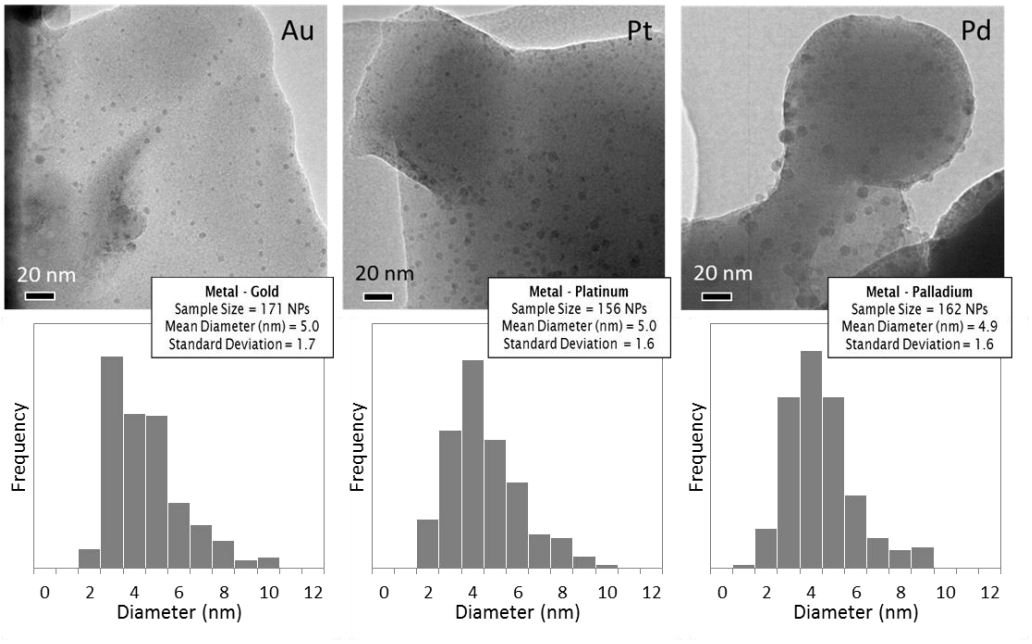

Figure 1.5: TEM images of calcined copper chlorophosphate framework materials showing nanoparticles and respective particle size distributions reproduced from Hinde *et al*.[70].

Later, Hinde *et al*.[72] reported that Pt and Pd nanoparticles tended to be more difficult to form via calcination in comparison to Au, as shown by the initial extended X-ray absorption fine structure (EXAFS) measurements in Figure 1.6. The EXAFS data for the calcined Au material showed evidence of metallic Au, although the similarity with the Au reference foil indicated mostly larger nanoparticles with more bulk properties. In contrast, the EXAFS data for the Pt and Pd material matched closely with the respective precursor chloride standards, highlighting the fact that only a small quantity of chlorometallate anions had been extruded to form nanoparticles. It is well-known that $[AuCl_4]^-$ can be thermally reduced in the presence of most gases[73], which would allow Au nanoparticles to form during the calcination process, however it was concluded that Pt and Pd most likely require more specific reducing conditions in order to form nanoparticles. Following this, a reduction procedure was developed, whereby the materials were reduced under a flow of hydrogen at 200 °C in order to improve the likelihood of extruding metallic nanoparticles from the copper chlorophosphate framework with an aim to improving the catalytic efficiency of the catalysts. This new procedure gave rise to smaller, more uniformly sized nanoparticles within the range of 2 – 5 nm, as shown by annular dark-field (ADF) aberration-corrected scanning transmission electron microscopy (AC-STEM) characterisation in Figure 1.7.

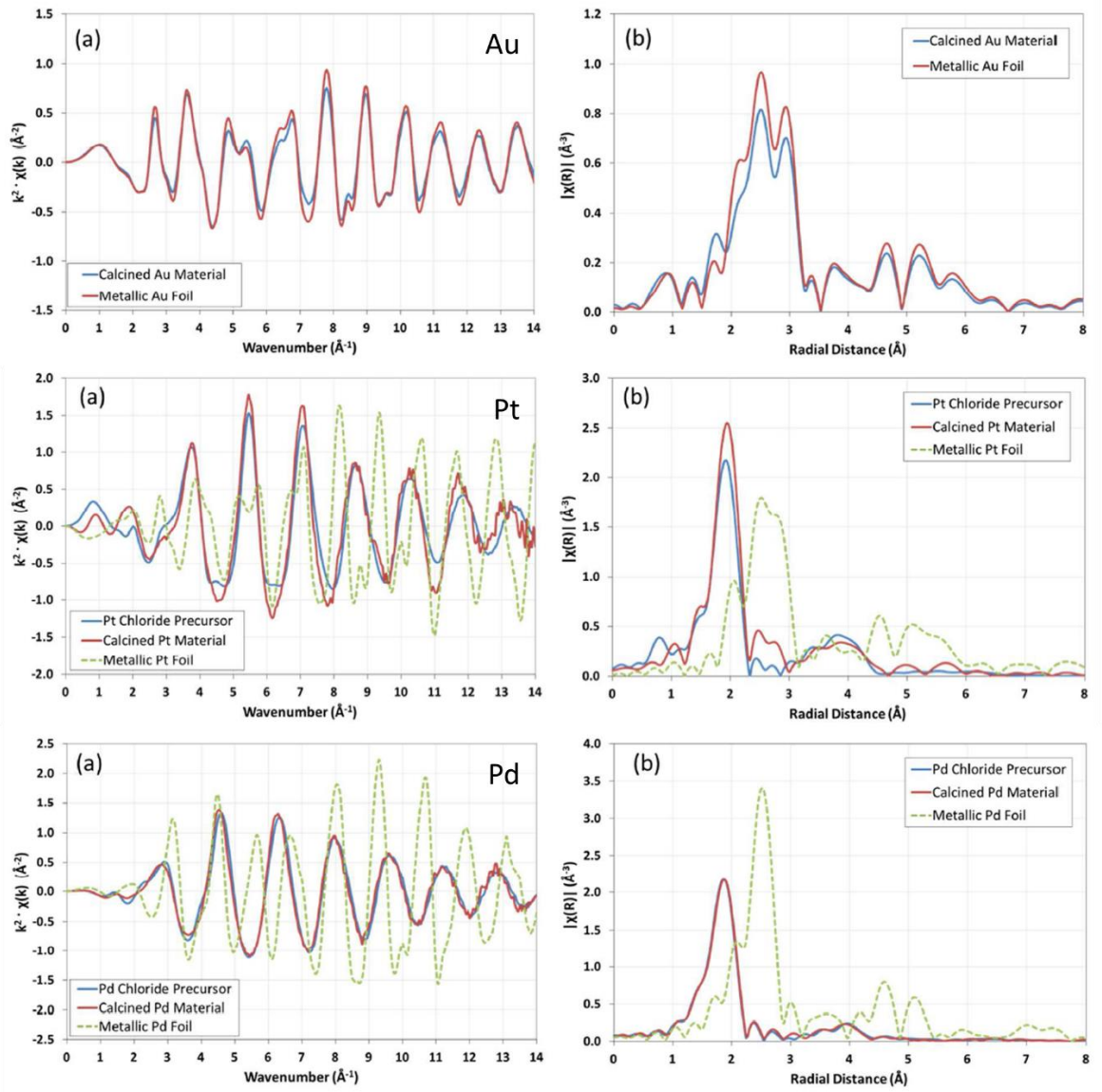

Figure 1.6: Non-fitted EXAFS spectra of Au, Pt and Pd calcined materials alongside reference materials, including k^2-weighted k-space plot (all a) and Fourier transform of EXAFS (all b), reproduced from Hinde *et al.*[72].

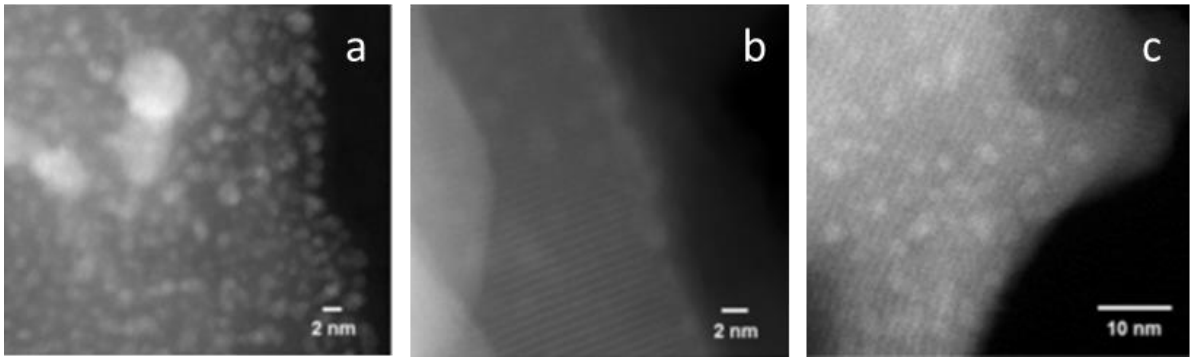

Figure 1.7: ADF AC-STEM images of reduced Pt (a), Pd (b) and Au (c) copper chlorophosphate materials, reproduced from Gill *et al*.[74].

The differences between the two activation procedures was perhaps most obvious when comparing the catalytic trends for the calcined and reduced materials. Originally, all three calcined catalysts achieved comparable levels of conversion (approx. 40 – 50 mol %) in the oxidation of vanillyl alcohol (see Figure 1.8), with similar selectivities for the aldehyde product (approx. 70 %). Initially this observation seemed reasonable as Au, Pt and Pd nanoparticles have all previously shown high activity for the oxidation of vanillyl alcohol[75–77], and the size distributions of the nanoparticles were all similar. However, on reduction the conversions achieved were much higher (approx. 70 mol % for Au and Pd, and 100 mol % for Pt), and the selectivities were slightly boosted for the aldehyde product (approx. 70 – 80 %). The stark contrast between the two activation procedures was highlighted most by the turnover numbers achieved, as shown in Figure 1.9. This increase in the activity was most likely the result of the higher propensity for the metal chloride precursor to be reduced under a reducing atmosphere, promoting the formation of metallic nanoparticles.

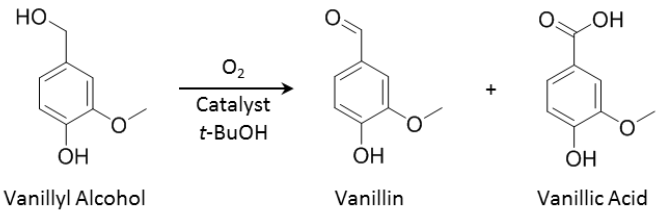

Figure 1.8: Oxidation of vanillyl alcohol to vanillin and vanillic acid.

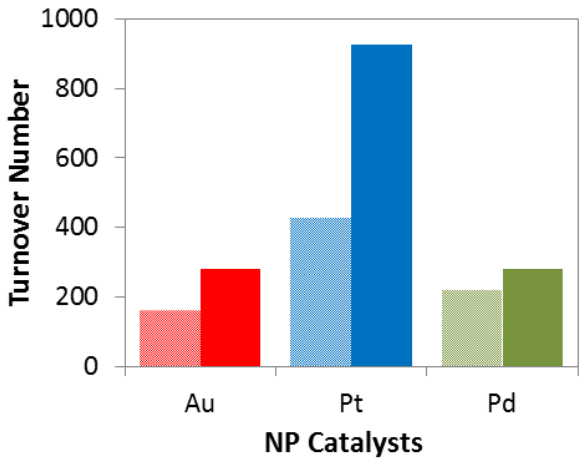

Figure 1.9: Comparison of catalytic turnover number for Au (red), Pt (blue) and Pd (green) calcined (patterned) and reduced (solid) catalysts in the oxidation of vanillyl alcohol, reproduced from Hinde *et al*.[72].

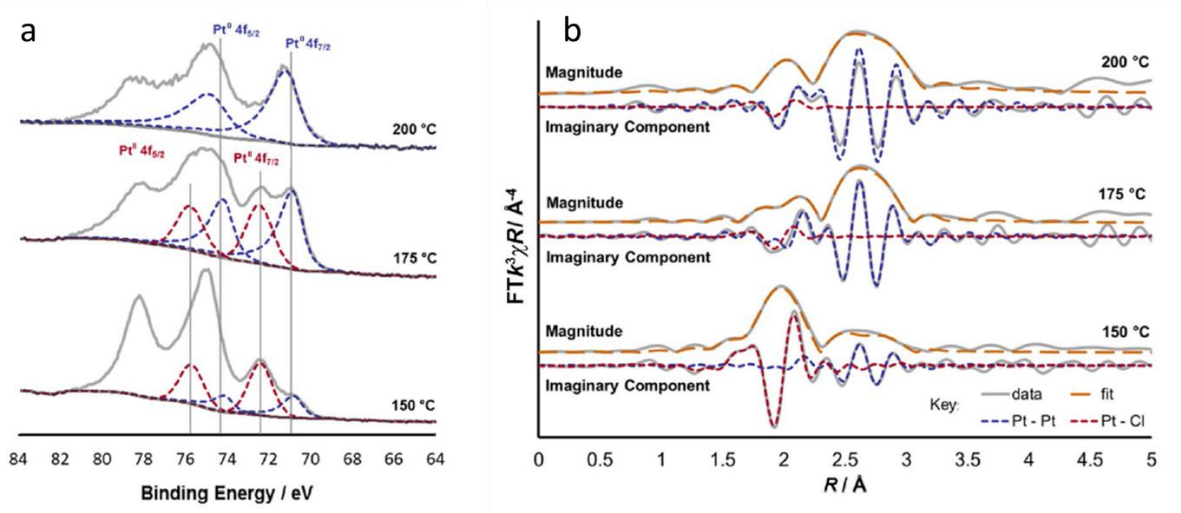

Figure 1.10: (a) XPS spectra of the reduced Pt copper chlorophosphate showing the transition from Pt^{II} (red dashed line) and Pt^{0} (blue dashed line) to Pt^{0} with increased reduction temperature, and (b) magnitude and imaginary component of the k^3-weighted Fourier transform for the EXAFS data for the Pt material reduced under different activation temperatures. Reproduced from Gill *et al*.[74].

Alongside the catalytic data, X-ray photoelectron spectroscopy (XPS) and EXAFS data also allude to the increased extrusion in the reduced catalysts. For the reduced Pt material, XPS data collected for

a range of activation temperatures (see Figure 1.10a) shows the transition from a mixture of Pt^{II} and Pt^0 at the surface, to Pt^0 with an increase in activation temperature, and as a result it was hypothesised that an activation temperature of 200 °C was sufficient for complete reduction of the Pt precursors to form nanoparticles. The EXAFS data collected (see Figure 1.10b and Figure A. 1 in the appendix) exhibits a similar trend, showing the progressive reduction of the Pt precursor with activation temperature across the bulk of the sample.

Similarly to the Pt material, the XPS data collected for the reduced Au material (see Figure 1.11a) shows the transition from a mixture of Au^{III} and Au^0 at the surface of the material, to Au^0 with increasing activation temperature. In contrast, the EXAFS data (see Figure 1.11b and Figure A. 2 in the appendix) shows only one component (Au-Cl), indicating that a significant component of the reduced samples is the Au precursor. However, despite there being no observable metallic component in the EXAFS data, some nanoparticle formation is clearly observed from the TEM and XPS data. As EXAFS is a bulk technique, it is possible that this inconsistency in the data may be explained by the presence of a significant quantity of the $[AuCl_4]^-$ precursor remaining throughout the material, with only a very small fraction of metallic Au nanoparticles forming on the surface of the material, as detected by XPS. It is also worth considering that the XPS data could be misleading, with XPS being found to photoreduce Au^{III} to Au^0 under the beam[78]. If this were the case, the Au^0 contribution could be artificially boosted by photoreducing the nanoparticle precursor to give the impression of forming more metallic Au nanoparticles. However, as the presence of metallic Au nanoparticles has been confirmed by TEM, it is likely that some nanoparticles are present, even if their occurance could be boosted in the XPS data through potential photoreduction of the precursor.

In contrast, the XPS collected for the reduced Pd material (see Figure 1.12a) show the mixture of Pd^{II} and Pd^0 that remains over each activation temperature. The corresponding EXAFS data (see Figure 1.12b and Figure A. 3 in the appendix) is in agreement, with a large contribution from the Pd precursor and a minor contribution from metallic Pd.

From the XPS and EXAFS data, it was noted that the Pt copper chlorophosphate material appeared to be more susceptible to nanoparticle formation by extrusion than the Au or Pd analogues. As such, it is likely that the Au and Pd materials might require higher activation temperatures in order to achieve complete extrusion.

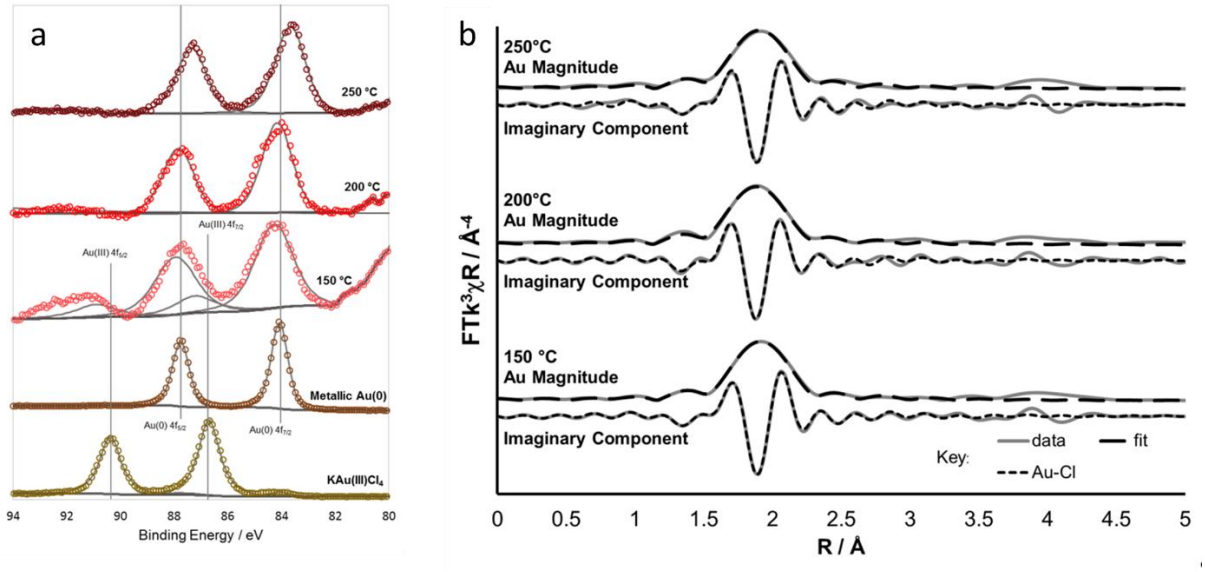

Figure 1.11: (a) XPS spectra of the reduced Au copper chlorophosphate showing the transition from Au^{III} and Au^0, to Au^0 with increased reduction temperature, and (b) magnitude and imaginary component of the k^3-weighted Fourier transform for the EXAFS data for the Au material reduced under different activation temperatures. Reproduced from Gill *et al.*[74].

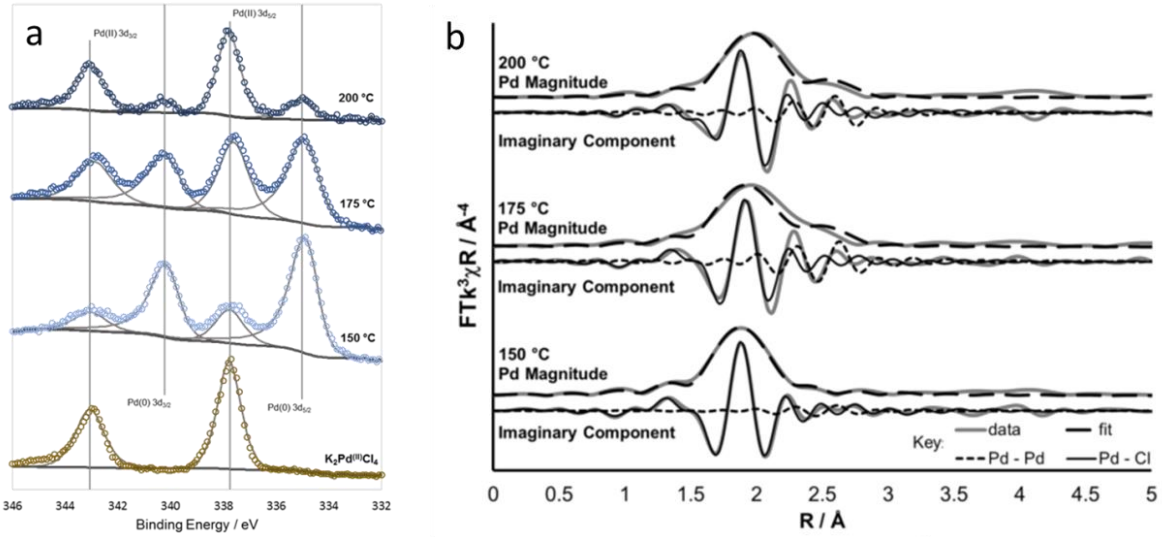

Figure 1.12: (a) XPS spectra of the reduced Pd copper chlorophosphate showing the mixture of Pd^{II} and Pd^0 that remains over each activation temperature, and (b) magnitude and imaginary component of the k^3-weighted Fourier transform for the EXAFS data for the Pd material reduced under different activation temperatures. Reproduced from Gill *et al.*[74].

Currently the monometallic copper chlorophosphate materials have been developed to be activated under a reducing atmosphere, with studies showing the reduction process yields more active catalysts compared to the initial calcination process, most likely through a greater extent of nanoparticle formation. The Pt copper chlorophosphate material showed a higher propensity to form metallic nanoparticles under these reducing conditions, whereas the Pd materials displayed a mixture of oxidation states in all samples, suggesting incomplete reduction to form metallic nanoparticles on the surface of the support. The Au copper chlorophosphate showed complete reduction to metallic Au when reduced to 250 °C, however the EXAFS data suggested that incomplete extrusion had occurred in this sample. As such, the Pt material proved to be the most promising for generating small, uniform metallic nanoparticles. The monometallic copper chlorophosphates (Pt in particular) have been successful in the oxidation of a variety of different alcohols, including benzyl alcohol[70,79], vanillyl alcohol[72] and KA-oil[74] (ketone-alcohol oil, a mixture of cyclohexanone and cyclohexanol), and as such provide a basis for exploring the prospect of bimetallic copper chlorophosphate materials for catalysis. From here on in, the copper chlorophosphate material will be abbreviated to CuClP.

1.4 KA-Oil Oxidation

Cyclohexanone is a vital chemical intermediate in the production of plastics, with over 2.8 million metric tons primarily converted to the Nylon precursors, adipic acid and ε-caprolactam, the general processes of which are outlined in Figure 1.13 below.

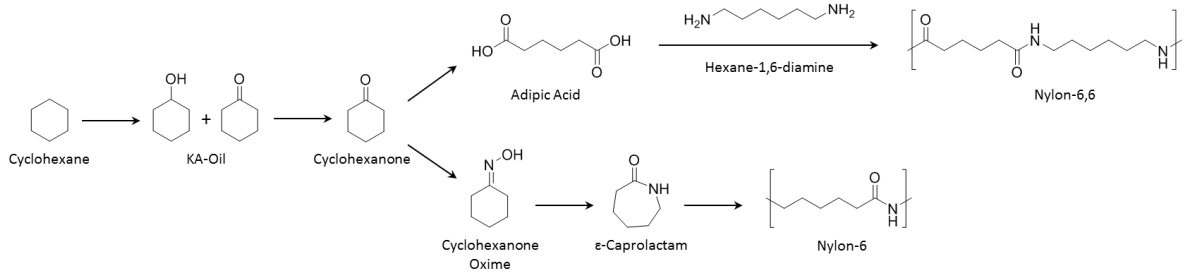

Figure 1.13: General schematic outlining the manufacture of Nylon-6,6 and Nylon-6 from cyclohexane.

Cyclohexanone is mainly produced by the hydrogenation of phenol[80,81] and by the oxidation of cyclohexane[82,83]; however both industrial routes produce a mixture of cyclohexanol and cyclohexanone, known as KA-oil. Due to the similar boiling points of the components in KA-oil

(156 °C and 161 °C for cyclohexanone and cyclohexanol respectively[84]), complex and costly distillation procedures are required in order to separate them, and thus it would be desirable to directly and selectively produce cyclohexanone from the mixture of KA-oil. Industrially, the oxidation of cyclohexanol requires stoichiometric amounts of inorganic oxidants (e.g. Cr(III) salts), harmful solvents and high temperatures[85], and so there is great interest in providing a route that is more environmentally benign.

Significant research has been dedicated to the oxidation of cyclohexanol to cyclohexanone using benign oxidants, such as hydrogen peroxide and air, and through dehydrogenation processes. Note that in the literature (see Table 1.4, pg. 21), both the oxidation of cyclohexanol and the dehydrogenation of cyclohexanol is explored to produce cyclohexanone. Typically, oxidation reactions involve the addition of an oxygen atom to a substrate, and dehydrogenation reactions involve the removal of hydrogen atoms from the substrate. However, as dehydrogenation reactions are a type of oxidation, the oxidation of cyclohexanol can be described as an oxidative dehydrogenation process, where the substrate is dehydrogenated by the metal catalyst, and the adsorbed hydrogen atoms are then oxidised[86]. In accordance with the 12 principles of green chemistry, molecular oxygen or air are ideal oxidants; however, their use can be limited due to the challenge in activating them for reaction. Fortunately, metal nanoparticle catalysts have shown a propensity for activating oxygen[87,88], and as such have been widely investigated in the aerobic oxidation of cyclohexanol. Although not extensive, a brief overview of some of the literature exploring the oxidation of cyclohexanol can be seen in Table 1.4 (pg. 21). There is very limited research on using KA-oil as a feedstock, with only one case (to my knowledge) converting KA-oil to cyclohexanone. As such, the conversion of KA-oil to cyclohexanone will be explored in this work, with hopes to circumvent the need to separate cyclohexanol prior to oxidation to cyclohexanone in industry.

Prior work by Gill *et al.*[74] (see Figure 1.14) using the monometallic CuClP materials has shown the Pt/CuClP material to be the most active, with the catalyst activated at 200 °C achieving a cyclohexanone yield of ca. 55 %. Minimal conversions were achieved using the Au and Pd analogues, as reflected by the low yields of cyclohexanone, suggesting that these materials were less effective at activating oxygen in the air for the oxidation of the alcohol.

It is generally accepted that oxidation reactions undertaken by most heterogeneous metal or metal oxide oxidation catalysts proceed via heterolytic pathways[89], where the bonding pair of electrons is split unevenly. For gold catalysts, Abad *et al.*[90] proposed that the aerobic oxidation of alcohols occurs via the adsorption of the alcohol to form a metal-alcoholate species, which will undergo

abstraction of the β-hydride to the surface of the metal, liberating the desorbed carbonyl product. The surface hydrides are then rapidly oxidised by activated adsorbed superoxo-species (formed by the adsorption of O_2 on the surface of the metal) to form water whilst regenerating the adsorption sites on the catalyst. Using this information, a mechanism for the oxidation of cyclohexanol using oxygen can be proposed (see Figure 1.15).

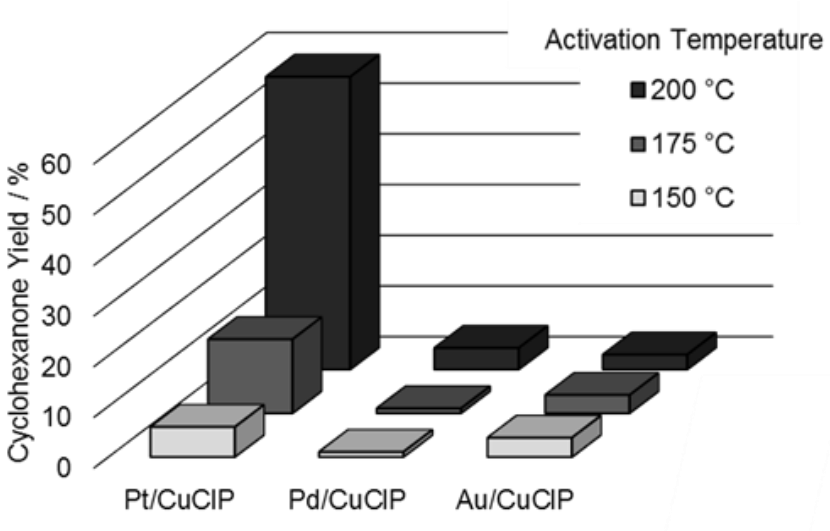

Figure 1.14: Comparison of cyclohexanone yields obtained for the monometallic copper chlorophosphate (CuClP) materials activated at a range of reduction temperatures; reproduced from Gill *et al*.[74].

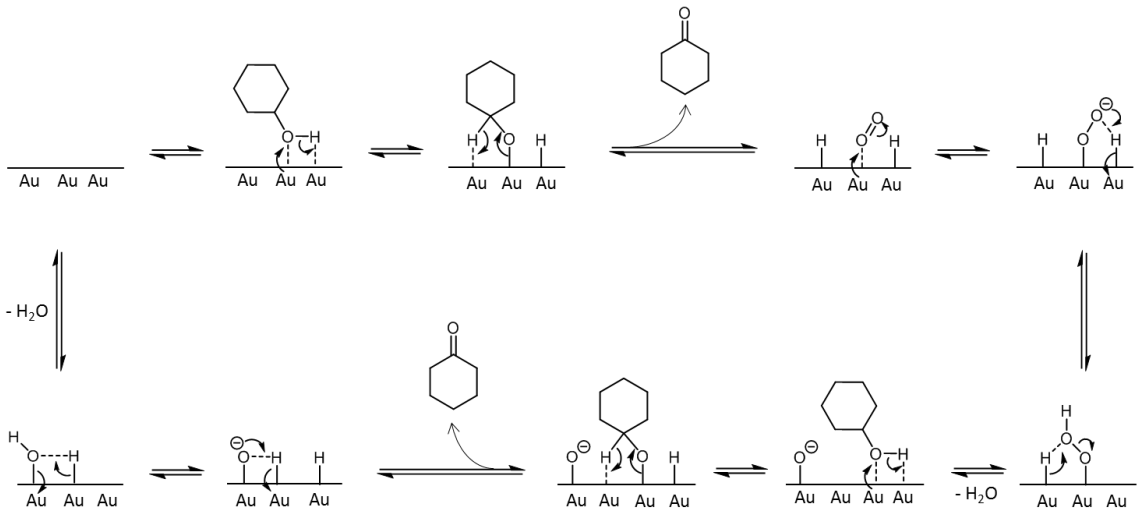

Figure 1.15: Proposed mechanism for the aerobic oxidation of cyclohexanol using a gold catalyst.

Many challenges lay ahead in the oxidation of KA-oil, most notably in the effective activation of molecular oxygen to afford high activities in the aerobic oxidation of cyclohexanol. It is desirable to develop a system where high conversions can be obtained whilst also maintaining a high selectivity for cyclohexanone when utilising KA-oil as the feedstock. Ideally the source of molecular oxygen would come from air, and the process itself should utilise lower temperatures and less harmful solvents than traditional industrial processes. With this in mind, the aerobic oxidation of KA-oil will be explored in the vapour phase, in a solvent-free process.

Table 1.4: Oxidation and dehydrogenation of cyclohexanol (or KA-oil) to cyclohexanone.

Catalyst		Process	Substrate	Oxidant	Temperature / °C	Time / hr	Conversion / mol %	Cyclohexanone Selectivity / %	Ref.
Active Species	Support								
DPPH	WO_3 / Al_2O_3	Batch	Cyol	O_2	80	4	81	12	[91]
Cs	$H_{0.5}PW_{12}O_{40}$	Batch	Cyol	H_2O_2	90	4	14	> 99	[92]
WO_3	-	Batch	Cyol	H_2O_2	70	2	100	> 99	[93]
Cr	13X	Batch	Cyol	TBHP	90	10	98	92	[94]
Cu	$La_2O_2CO_3$	Batch	Cyol	*	150	8	91	> 99	[95]
Mn	MCM-41	Continuous	Cyol	Air	350	2	90	50	[96]
Pt	Solution	Batch	Cyol	O_2	80	24	88	89	[97]
Au	TiO_2	Batch	Cyol	H_2O_2	90	1	87	> 99	[98]
Mn	AlPO-5	Batch	Cyol	H_2O_2	60	3	86	51	[99]
Ru	$Co(OH)_2$ / CeO_2	Batch	Cyol	O_2	60	8	83	98	[100]
RuO_2	Silicotungstate	Batch	Cyol	O_2	110	48	83	81	[101]
H_2WO_4	-	Batch	Cyol	H_2O_2	90	1	82	> 99	[102]
Cu	ZnO / C	Continuous	Cyol 95:5 Cyone	*	290	6	80	75	[103]

CoO	SBA-15	Batch	Cyol	TBHP	83	24	80	†	[104]
FeO	MIL-101	Microwave	Cyol	H_2O_2	120	0.25	77	> 99	[105]
Cr	AlPO-5	Batch	Cyol	H_2O_2	60	3	71	50	[99]
Ti	TS-1	Batch	Cyol	H_2O_2	60	3	67	> 99	[99]
Cr	FAU	Batch	Cyol	TBHP	60	23	64	†	[106]
Pd	CeO_2	Batch	Cyol	O_2	120	12	58	98	[107]
V_2O_5	$KMn_8O_{16}.nH_2O$	Batch	Cyol	TBHP	90	8	49	> 99	[108]
Ti	Beta	Batch	Cyol	H_2O_2	65	3	44	55	[109]
RuO_2	FAU	Batch	Cyol	O_2	80	4	43	> 99	[110]
Au	Fe_3O_4 / SiO_2	Batch	Cyol	O_2	100	6	42	> 99	[111]
Cu	MgO / Cr_2O_3	Continuous	Cyol	*	200	-	38	> 99	[112]
Au	SiO_2	Batch	Cyol	O_2	80	4	38	> 99	[113]
Cu	$Cl/C_{12}H_8N_2$	Batch	Cyol	O_2	60	6	33	78	[114]
Cu	CeO_2	Continuous	Cyol	*	350	1	32	86	[115]
Ni	CeO_2	Continuous	Cyol	*	350	1	26	93	[115]
V_2O_5	$KMn_8O_{16}.nH_2O$	Batch	Cyol	H_2O_2	90	8	26	> 99	[108]

Pt	Ca-ZSM-5	Batch	Cyol	Air	25	20	22	82	[116]
Pt	Mg-ZSM-5	Batch	Cyol	Air	25	20	21	86	[116]
Au	Polystyrene	Batch	Cyol	O_2	25	24	10	> 99	[117]
Ti	Beta	Batch	Cyol	H_2O_2	65	5	10	> 99	[118]
Ag	-	Continuous	Cyol	Air	580	-	10	90	[119]
Pt	SiO_2	Batch	Cyol	Air	25	20	5	90	[116]
TiFe	MCM-41	Continuous	Cyol	*	240	-	86	63	[120]
PtCo	Al_2O_3	Continuous	Cyol	*	250	-	80	28	[121]
AuPd	SiO_2	Batch	Cyol	Air	80	24	62	> 99	[122]
AuCu	SiO_2	Batch	Cyol	O_2	80	4	49	> 99	[113]
CuNi	CeO_2	Continuous	Cyol	*	350	1	42	90	[115]
MgMnTi	Hydrotacite-like hydroxides	Batch	Cyol	O_2	100	2	4	> 99	[123]

Cyol = cyclohexanol, Cyone = cyclohexanone, DPPH = 1,1-diphenyl-2-picrylhydrazyl, TBHP = *tert*-butyl hydroperoxide; * dehydrogenation reaction; † data not included. Table has been arranged into non-metal (orange highlight), metallic (blue highlight), monometallic transition metal (white highlight), bimetallic (grey highlight) and trimetallic (green highlight) catalysts.

1.6 Aims and Objectives

To synthesise bimetallic variants of the copper chlorophosphate materials, and explore the effect of reduction temperature on the extrusion of nanoparticles from the framework through TEM and XPS.

Following this, probe the catalytic potential of these materials for the oxidation of the industrially significant feedstock, KA-oil, realising the following goals:

- Utilise air as a benign oxidant in the aerobic oxidation of KA-oil
- Selectively produce cyclohexanone in high yield
- Employ a solvent-free vapour phase process, using lower temperatures and less harmful reagents than traditional industrial processes

To probe the nature of the bimetallic nanoparticles through physical mixture tests, as well as the influence of the support on the activity of the nanoparticle catalysts.

Explore the catalytic potential of copper chlorophosphate materials in other significant reactions, such as the oxidation of valerolactam, the hydrogenation of furfural, the Beckmann rearrangement of cyclohexanone oxime, and the Baeyer-Villiger oxidation of cyclohexanone.

Chapter 2: Experimental Methods

2.1 Synthesis of Materials

All chemicals were purchased from Sigma Aldrich or Fisher Scientific and used without further purification. Gases were sourced from BOC Industrial Gases and used as supplied.

2.1.1 Hydrothermal Synthesis of Monometallic Copper Chlorophosphate Frameworks (3.5 wt. %) – $[Rb_9Cu_6(P_2O_7)_4Cl].[MCl_4]Cl_x$, (M = Au, Pt or Pd; x = 3 for Au, or 2 for Pt & Pd)

Copper(II) fluoride (framework metal source; 117 mg, 1.15 mmol), rubidium chloride (counterion; 28.0 mg, 2.32 mmol) and a source of metal chloride salt (nanoparticle precursor; gold(III) chloride hydrate (26.6 mg, 0.068 mmol, to give 3.5 wt. %), potassium tetrachloroplatinate(II) (28.4 mg, 0.068 mmol, to give 3.5 wt. %), potassium tetrachloropalladate(II) (40.9 mg, 0.125 mmol, to give 3.5 wt. %)) were accurately weighed out and ground in an agate pestle and mortar for 2 minutes to homogenise. The mixture was added to the Teflon® liner of a custom-made 23 mL hydrothermal vessel, and orthophosphoric acid (phosphorous source; 85 wt. % in water, 0.20 mL, 2.9 mmol) was added dropwise wetting the entire contents. The mixture was sonicated for 5 minutes to encourage mixing. Rubidium hydroxide (counter ion and base; 50 wt. % in water, 0.24 mL, 2.4 mmol) was added dropwise (CAUTION – HF gas produced) wetting the entire contents and the mixture was sonicated for 10 – 15 minutes until the mixture was homogenous. The hydrothermal vessel was sealed and heated to 175 °C for 48 hours in a convection oven. The vessels were allowed to cool naturally before collecting the product by filtration, washing with deionised water (100 mL) and drying overnight at 80 °C. Products formed as brilliant green cuboid crystals for Au and Pt materials, and as light brown crystals for the Pd material. A flow chart of the process is shown in Figure 2.1.

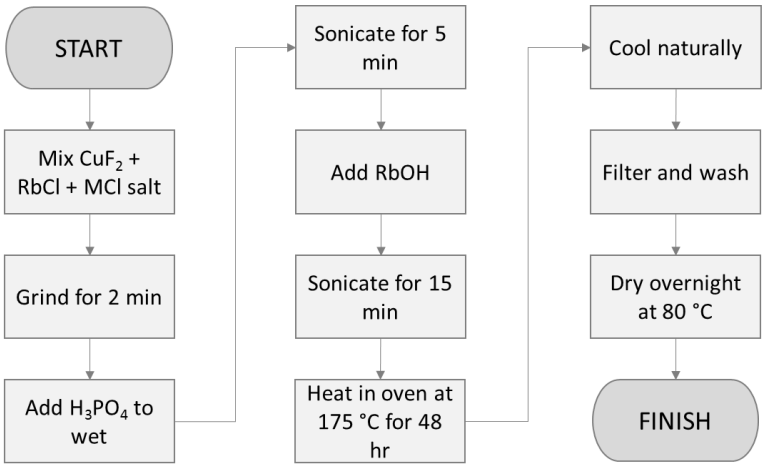

Figure 2.1: Flow diagram of the hydrothermal synthesis of the CuClP materials.

2.1.2 Hydrothermal Synthesis of Bimetallic Copper Chlorophosphate Frameworks (7 wt. %)

A similar procedure was followed for the synthesis of the bimetallic copper chloropyrophosphates, however two sources of metal chloride salts (nanoparticle precursors; gold(III) chloride hydrate (26.6 mg, 0.068 mmol, to give 3.5 wt. %), potassium tetrachloroplatinate(II) (28.4 mg, 0.068 mmol, to give 3.5 wt. %), potassium tetrachloropalladate(II) (40.9 mg, 0.125 mmol, to give 3.5 wt. %)) were used. Products formed as brilliant green cuboid crystals for AuPt material, and as light brown/green crystals for the AuPd and PtPd materials.

2.1.3 Thermal Activation of the Copper Chlorophosphate Frameworks

As-synthesised materials were activated in reducing conditions under a 150 mL min^{-1} flow of 5 % H_2/N_2 for 2 hours at a specified temperature. After reduction, the Au/CuClP, Pt/CuClP and AuPt/CuClP materials appear progressively darker with temperature, while the Pd/CuClP, AuPd/CuClP and the PtPd/CuClP materials change from light brown/green to darker khaki green from 150 to 200 °C, and then black at temperatures higher than 250 °C where the framework degrades, as confirmed by powder X-ray diffraction analysis.

2.2 Reaction Parameters

All chemicals were purchased from Sigma Aldrich or Fisher Scientific and used without further purification. Gases were sourced from BOC Industrial Gases and used as supplied.

2.2.1 Vapour Phase Oxidation of KA-Oil

Catalytic reactions were carried out in a cylindrical quartz fixed-bed reactor (4 mm in diameter) with a quartz frit. The reactor was packed with a 1 inch layer of glass beads (1 mm diameter) and packed with pelletized catalyst (0.20 g), before a further layer of glass beads were added to 1 inch from the top of the reactor tube. The catalyst was pre-treated at 200 °C under a 25 mL min^{-1} flow of air for 1 hour. A liquid feed of KA-oil (1:1 mixture of cyclohexanol and cyclohexanone) was fed via an electronic syringe pump into the reactor at a flow rate of 15 µL min^{-1}, and the system was left to equilibrate for 1 hour. Aliquots of the reaction mixture were taken hourly and samples for analysis were made up in a 1:1 ratio with a 1.96 M solution of the internal standard triethylene glycol dimethyl ether in acetone. Samples were diluted using acetone and analysed using gas chromatography (GC). A simplified schematic of the fixed-bed reactor set-up used is shown in Figure 2.2.

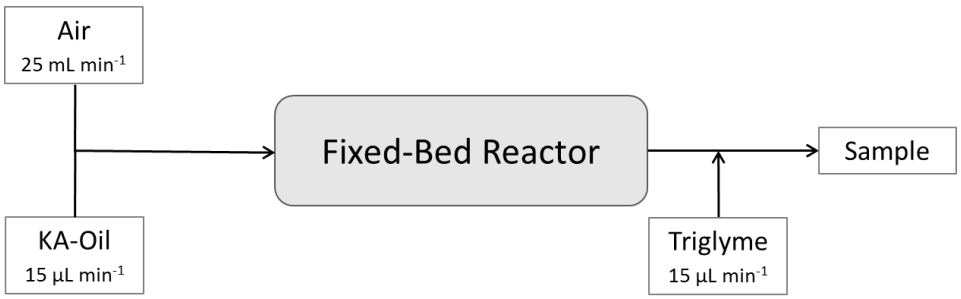

Figure 2.2: Schematic of fixed-bed reactor set-up for the vapour phase oxidation of KA-oil.

2.2.2 Liquid Phase Beckmann Rearrangement of Cyclohexanone Oxime

Cyclohexanone oxime (0.10 g, 0.88 mmol), anhydrous chlorobenzene (0.10 g, 0.89 mmol, internal standard) and catalyst (0.10 g, dried under vacuum) were added to anhydrous benzonitrile (20 mL) in a 3-necked round bottom flask, and stirred under reflux and nitrogen at 130 °C for 7 hours. Samples were taken hourly, diluted in ethanol and analysed using GC.

2.2.3 Liquid Phase Baeyer-Villiger Oxidation of Cyclohexanone

Cyclohexanone (0.17 g, 1.75 mmol), hydrogen peroxide (35 wt. % in water, 0.08 mL, 1.17 mmol), triethylene glycol dimethyl ether (0.09 g, 0.50 mmol, internal standard) and catalyst (0.08 g) were added to dioxane (5 mL) and the reaction mixture was stirred under reflux at 90 °C for 24 hours. Samples were taken hourly and analysed using GC.

2.2.4 Liquid Phase Oxidation of δ-Valerolactam

δ-Valerolactam (58.5 mg, 0.590 mmol), chlorobenzene (22.5 mg, 0.200 mmol) and catalyst (20.0 mg) were added to *tert*-butanol (3 – 5 mL). *tert*-Butyl hydroperoxide (6.0 M in decane, 0.24 mL, 1.2 mmol) was added and the reaction mixture was stirred under reflux at 80 °C for 24 hours. After the reaction, a sample of the crude reaction mixture (0.5 mL) was prepared for NMR analysis by removing the solvent and dissolving in deuterated chloroform.

2.3 Characterisation Techniques

2.3.1 Gas Chromatography (GC)

Gas chromatography (GC) is an analysis technique used to separate chemical components based on particular properties, most commonly boiling point and polarity. As such, GC can be used to monitor

the progress of organic reactions by representing components as individual peaks, the area of which can be used to quantify the molar concentrations present though a series of calibrations.

GC works by injecting a liquid or gaseous sample into a heated injection port, where the sample is vapourised before being carried into the heated column (stationary phase) by the carrier gas, helium. Each component will move through the column at different rates depending on their affinity to the stationary phase, and as a result will separate from one another and elute from the column at different times. As the components elute from the column they reach the flame-ionisation detector (FID) where they are burnt in a mixture of hydrogen and air to generate a small current. This current is detected by the FID and the signal generated gives rise to a chromatogram.

In order to quantify the molar concentrations of components present in a sample, the area of a GC peak can be linked to the number of moles injected by determining the response factor (β) of the instrument for the particular compound, as shown in Equation 2.1.

$$Moles\ (X) = \beta_X \times Area\ (X)$$

Equation 2.1: Equation for relating the area of a GC peak to the number of moles of a component (X) through the response factor (β).

Due to variations in instrument response it is common practice to measure the response factor of each compound relative to a known quantity of a single reference compound, known as a standard, giving rise to a relative response factor (γ). As long as the moles of the standard compound remain constant and known, it is possible to calculate the number of moles of each component through the relationship shown in Equation 2.2.

$$\frac{Moles\ (X)}{Moles\ (Std)} = \frac{\beta_X}{\beta_{Std}} \times \frac{Area\ (X)}{Area\ (Std)} = \gamma_{\frac{X}{Std}} \times \frac{Area\ (X)}{Area\ (Std)}$$

Equation 2.2: Equation for relating the area of a GC peak relative to a standard (Std) to the number of moles of a component (X) through the relative response factor (γ).

To obtain relative response factors, a set of calibration solutions are made containing a range of concentrations of a component (X) and a constant concentration of the standard (Std), and each solution is injected into the GC three times in a random order in order to avoid sample

contamination or bias. The data is plotted with the area ratio (Area (X) / Area (Std)) on the x-axis and the molar ratio (Moles (X) / Moles (Std)) on the y-axis, and the gradient of the straight line produced gives the relative response factor, $\gamma_{X/Std}$ (see Figure 2.3).

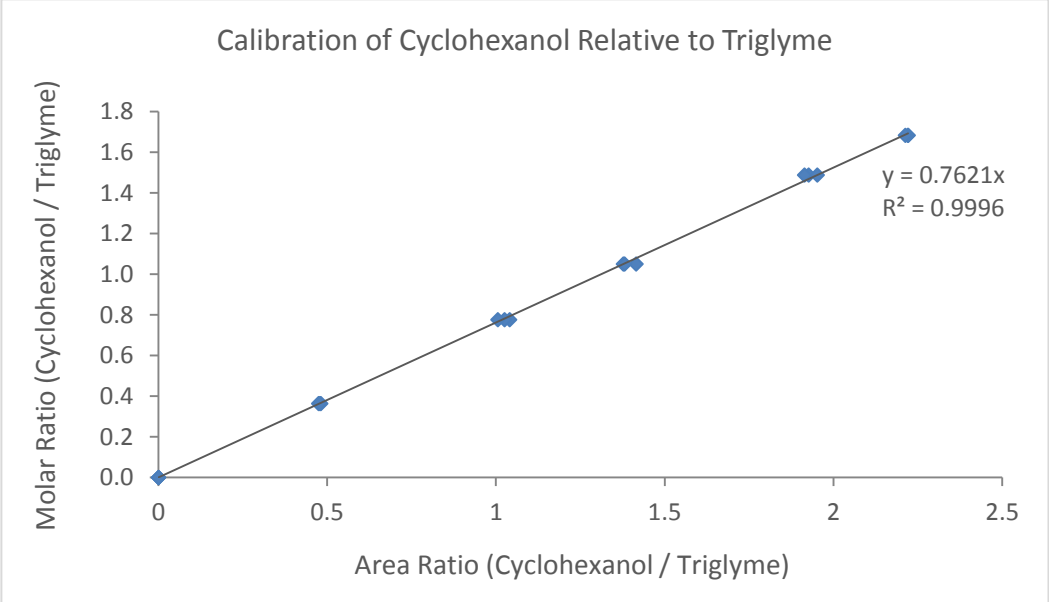

Figure 2.3: GC calibration of cyclohexanol relative to triethylene glycol dimethyl ether (triglyme) standard.

Quantifying Catalytic Activity

It is important to be able to define catalytic activity in order to enable comparisons of catalytic systems within the literature. The concepts of conversion and selectivity are perhaps the most useful in terms of assessing the effectiveness of a catalyst for a particular process, with the conversion describing how much reactant has reacted, and the selectivity describing the ratio of how much desired product was formed compared to the undesired products. These concepts are defined in Equation 2.3 and Equation 2.4. Note that in this report the selectivity of the product cyclohexanone will be calculated using the difference in the initial and final number of moles, as cyclohexanone will be present from the start of the reaction.

$$Conversion\ (mol\ \%) = \frac{Initial\ Moles\ SM\ (mol) - Final\ Moles\ SM\ (mol)}{Initial\ Moles\ SM\ (mol)} \times 100\ \%$$

Equation 2.3: Equation for calculating the mole percentage conversion, defined as the loss of starting material (SM).

$$Selectivity\ (\%) = \frac{Moles\ of\ Desired\ Product\ (mol)}{\sum Moles\ of\ All\ Products\ \ (mol)} \times 100\ \%$$

Equation 2.4: Equation for calculating the percentage selectivity, defined as the percentage the desired product is found to be of all produced products.

The yield is also an important measure of the efficacy of a catalyst, with the yield detailing how much desired product was formed. However, it is important to consider the mass balance of a system when determining the percentage yield as sometimes substrate losses may occur through routes other than the formation of product, which are undetectable (decomposition, formation of non-volatile products, etc.). The above equations assume that the total number of moles within a system remains constant; however, in reality this is not always the case, and the mass balance is a measure of the discrepancy between the initial number of moles and the number of moles calculated during analysis. Taking the mass balance into account, the calculation for the percentage yield is shown in Equation 2.5.

$$Yield\ (\%) = \frac{Moles\ of\ Product\ (mol)}{Initial\ Moles\ of\ SM\ (mol)} \times Mass\ Balance\ (\%)$$

Equation 2.5: Equation for calculating the percentage yield of a product taking into account the mass balance.

While the terms conversion, selectivity and yield are useful, they do not give any information about the efficiency of the catalyst itself. As such, it would be beneficial to present turnover numbers (TON) and turnover frequencies (TOF) alongside these terms. The turnover number is a measure of mole conversion with respect to the number of active species present, while the turnover frequency is this ratio per unit time, and these concepts are defined in Equation 2.6 and Equation 2.7. Accurate turnover frequencies were determined in this report using metal loadings measured by inductively coupled plasma optical emission spectroscopy (ICP-OES).

$$TON = \frac{Moles\ SM\ (mol) \times \left(\frac{Conversion\ (\%)}{100\ \%}\right)}{Moles\ of\ Catalyst\ Active\ Species\ (mol)}$$

Equation 2.6: Equation for calculating the turnover number (TON), described as the total number of catalytic cycles completed per active site.

$$TOF\ (hr^{-1}) = \frac{TON}{time\ (hr)}$$

Equation 2.7: Equation for calculating the turnover frequency (TOF), described as the total number of catalytic cycles completed per active site per unit time (hr).

The use of turnover number and turnover frequency alongside conventional conversion and selectivity allows for a more complete evaluation of a catalyst's performance, and in taking into account the loading and amount of catalyst used, they allow different systems to be compared directly.

Catalysis samples were analysed using a PerkinElmer Clarus 480 gas chromatograph with a FID using an Elite 5 column. Products were identified against authenticated standards and quantified by calibration to obtain response factors against an internal standard.

2.3.2 Gas Chromatography Mass Spectrometry (GC-MS)

GC-MS is an analytical technique that allows components in a mixture to be separated before analysis using mass spectrometry. As such, GC-MS can be used to identify compounds in a mixture, and if calibrations are used, the concentration can be quantified.

GC-MS works in a similar way to GC, in which the different components of a mixture are separated based on boiling point and polarity. As individual components elute from the GC column, they enter an electron ionisation detector where they are bombarded with electrons causing them to fragment. These fragments usually carry a + 1 charge, and as such the mass to charge ratio (M/Z) represents the molecular weight of each fragment. A quadrupole magnet focuses each of the fragments through a slit and into a detector, covering a range of M/Z values and giving rise to a mass spectrum.

Samples were analysed using a ThermoQuest Finnigan Trace MS 2000 series gas chromatograph mass spectrometer with FID using an RTX5 column.

2.3.3 Nuclear Magnetic Resonance (NMR) Spectroscopy

NMR spectroscopy is widely used to determine the identity of compounds through providing information on the physical and chemical properties of atoms within a molecule. NMR can also be used to monitor the progress of reactions provided the identity of all components can be determined, and the peaks of interest do not overlap.

NMR can be utilised in a similar way to GC, whereby the appearance and disappearance of peaks relating to starting materials and products can be followed in order to determine the progress of a reaction. In order to do this a peak that disappears from the starting material must be identified, along with the appearance of another in the product. These peaks must be assigned and integrated. The ratio of these peaks to a standard peak (from a known quantity of an internal standard) allows the quantisation of the components in the reaction mixture, allowing conversions and selectivities to be calculated. This method is limited to simple reaction mixtures where all of the components are known and do not overlap. As such, NMR has not been used extensively to monitor reactions in this work.

Solution NMR spectra were recorded using a Bruker AVIIIHD 400 FT-NMR spectrometer in $CDCl_3$. Chemical shifts for proton spectra are reported on the delta scale, in ppm, referenced to tetramethylsilane (TMS).

2.3.4 Powder X-Ray Diffraction (PXRD)

X-ray diffraction is a non-destructive technique used to reveal information about the crystal structure and chemical composition of a sample. XRD depends on the elastic scattering of X-rays by electrons in atoms, with the distance between crystallographic planes being related to the wavelength of an X-ray by Bragg's law. Bragg's law defines the conditions for the reflection of X-rays by a crystal lattice, as illustrated in Figure 2.4, where d_{hkl} is the distance between crystallographic planes in a lattice, and θ_B is the Bragg angle.

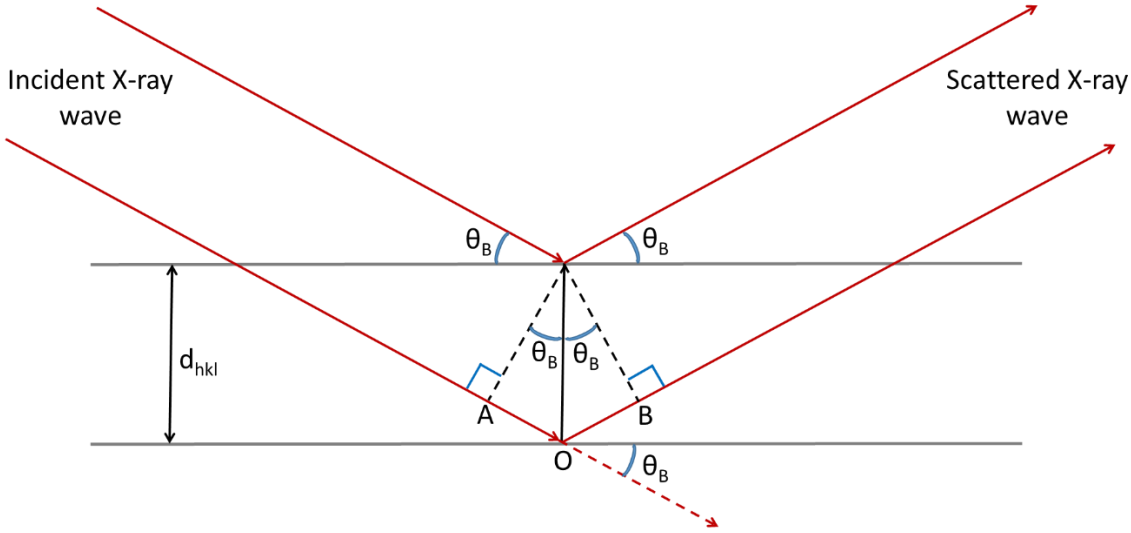

Figure 2.4: Derivation of Bragg's law, where dhkl is the distance between crystallographic planes and θ_B is the Bragg angle.

Constructive interference occurs between the scattered X-ray waves when the path-length difference (AO + OB) is equal to an integer value of the wavelength, AO + OB = nλ, i.e. when the waves are in phase, and this path-length difference can be expressed using Bragg's equation (see Equation 2.8).

$$n\lambda = 2d\ \sin\theta$$

Equation 2.8: Equation describing Bragg's law, where n is an integer, λ is the wavelength, d is the spacing between crystallographic planes, and θ is the angle of incidence of constructive interference.

When the incident angle, θ, satisfies Bragg's law a reflection will be observed at 2θ in the diffraction pattern, however if the scattered waves are out of phase destructive interference occurs and no peak is observed. Each set of hkl planes give rise to reflections at different angles, producing a unique pattern for each material. Indexing the diffraction data by assigning peaks to hkl planes and considering systematic absences allows the determination of basic crystallographic information, such as lattice parameters and types.

In order to gain this information, powder samples are finely ground and compressed into a sample holder to ensure a random distribution of crystallite orientations. The X-ray source and the detector move relative to one another to scan through a range of 2θ, the data of which is then commonly represented by plotting the diffraction angle (2θ) against the intensity to give rise to a diffraction pattern.

PXRD patterns were collected using a Bruker D2 Phaser diffractometer using Cu Kα1 and Cu Kα2 radiation, where average λ = 1.5418 Å.

2.3.5 Brunauer-Emmett-Teller (BET) Adsorption Measurement

Gas adsorption is a powerful tool used for probing the surface areas and pore volumes of nanoporous materials by adsorbing a probe molecule (typically nitrogen) onto the surface of a material and monitoring the change in pressure. For a system in equilibrium (see Equation 2.9), the adsorption of a probe molecule can be described using the Langmuir model, where the adsorption of the first monolayer (surface coverage, θ) can be related to the number of adsorption sites (N) and the pressure (P) (see Equation 2.10, Equation 2.11 and Equation 2.12) using the Langmuir equation (see Equation 2.13).

$$A_{(g)} + S \leftrightarrow AS$$

Equation 2.9: Equation describing the adsorption and desorption of an adsorbate at equilibrium, where $A_{(g)}$ is the gaseous adsorbate, S is the empty adsorption site and AS is the site occupied by the adsorbate.

$$Rate_{ads} = k_a PN(1-\theta)$$

Equation 2.10: Equation describing the rate of adsorption, $Rate_{ads}$, where k_a is the rate constant of adsorption, P is the pressure, N is the number of adsorption sites and θ is the surface coverage.

$$Rate_{des} = k_d N\theta$$

Equation 2.11: Equation describing the rate of desorption, $Rate_{des}$, where k_d is the rate constant of desorption, N is the number of adsorption sites and θ is the surface coverage.

$$At\ equilibrium, \qquad k_a PN(1-\theta) = k_d N\theta$$

Equation 2.12: Equation describing the rate of adsorption and desorption at equilibrium, where k_a is the rate constant of adsorption, k_d is the rate constant of desorption, P is the pressure, N is the number of adsorption sites and θ is the surface coverage.

$$\theta = \frac{kP}{1+kP}$$

Equation 2.13: Langmuir equation describing the surface coverage, θ, of an adsorbate using the Langmuir model, where k is rate constant of absorption over desorption (k_a/k_d), and P is the pressure.

However, the over-simplified Langmuir model assumes that all adsorption sites are equivalent and that the adsorbed molecules do not interact, forming only a monolayer on the surface. As such, a more realistic model is required that reflects the likelihood of non-uniform multilayer adsorption at low pressures. The BET model is an extension of the Langmuir model that assumes that gas molecules adsorb in infinite layers, and can be described by the following equation (see Equation 2.14).

$$\frac{P}{V_a(P-P^0)} = \frac{1}{V_m C} + \frac{(C-1)}{V_m C}\left(\frac{P}{P^0}\right)$$

Equation 2.14: The Brunauer-Emmett-Teller (BET) equation, where P is the pressure of the adsorbate, P^0 is the saturation pressure of the adsorbate, V_a is the molecular volume of the adsorbate, V_m is the molecular volume of the gas required to form a monolayer, and C is the BET constant which is related to the energy of adsorption.

BET surface areas were determined by nitrogen adsorption-desorption isotherms using Micromeritics ASAP 2020. BET nitrogen adsorption measurements were performed at liquid nitrogen temperature, with samples by degassed under vacuum overnight prior to measurements.

2.3.6 Transmission Electron Microscopy (TEM)

Electron microscopy provides a powerful tool for imaging materials in very high resolution, allowing information to be gained regarding the morphology of a sample through the use of scanning electron microscopy (SEM), and crystallinity and electron density within a sample using transmission electron microscopy (TEM). Electron microscopy primarily relies on the elastic and inelastic scattering of electrons from the interaction of a high energy electron beam with a sample, with SEM utilising back-scattered electrons from elastic collisions and secondary electrons generated from inelastic scattering. SEM achieves high-resolution images by scanning an electron beam over the surface of a sample and collecting the scattered electrons, with the 3-dimensional images built up with the brightness being proportional to the number of electrons from a certain area. TEM produces high-resolution images of a sample by detecting transmitted electrons from an electron beam passing through a thin sample. The areas of a sample where the most electrons are absorbed (i.e. by higher atomic number elements or thicker regions of a sample) appear darker in the image produced. As such, this technique can be used to image particles with higher atomic numbers, making it a valuable technique for characterising the noble metal particles, allowing their size and distribution to be determined.

TEM images were collected using a JEOL 2000FXII transmission electron microscope at University College Cork, Ireland. Powder samples were prepared by supporting on lacey carbon or carbon film copper mesh grids.

2.3.7 Inductively Coupled Plasma Optical Emission Spectroscopy (ICP-OES)

ICP-OES is a type of optical emission spectroscopy used in the detection of trace metals. Typically samples are first digested using a strong acid in order to ensure all chemical bonds are broken down, before the sample is introduced to the instrument. ICP-OES uses inductively coupled plasma to produce excited ions that emit characteristic wavelengths of light, which can be related to the quantity of metal using the Beer-Lambert law. As such, ICP-OES can be used to determine the metal loadings for each catalyst, and so was used to accurately determine turnover frequencies for the catalysts tested in this work.

ICP analysis was performed using a Varian Vista MPX ICP-OES analyser at MEDAC Ltd., Surrey. Samples were digested in nitric acid, apart from when samples contained gold, in which case aqua regia (1:3 ratio mixture of concentrated nitric acid and concentrated hydrochloric acid) was used. ICP values were used to accurately determine turnover frequencies for the catalysts tested in this report.

2.3.8 X-Ray Photoelectron Spectroscopy (XPS)

XPS is a surface-sensitive spectroscopic analysis technique that provides information on the chemical nature of elemental components of a sample. The technique probes the top layer of a sample, penetrating to a depth of ~ 10 nm. Spectra are obtained through irradiating a sample with X-rays of a specific wavelength to induce the emission of photoelectrons, while measuring the quantity and kinetic energy of these electrons. The overall kinetic energy of an emitted electron can be used to determine the binding energy using the following equation (see Equation 2.15).

$$E_k = E_P - E_B$$

Equation 2.15: Equation showing the relationship between the kinetic energy of an emitted electron, E_k, the binding energy of an emitted electron, E_B, and the energy of the photon used to irradiate the sample, E_P.

As a result, any factors that affect the binding energy of an electron can be probed, including the chemical environment and the oxidation state.

XPS analysis was performed using a Thermo Scientific K-Alpha instrument equipped with monochromated AI Kα source at NEXUS, University of Newcastle. All XPS spectra were calibrated against the carbon and/or oxygen 1s peak, and high resolution spectra were fitted with Shirley backgrounds before peak analysis using CasaXPS software.

Chapter 3: Results and Discussion

Special Acknowledgments

I would like to acknowledge and thank the following colleagues for their contributions to this chapter:

Arran Gill, University of Southampton, UK: For useful discussions, coordinating collaborations and characterisation data from NEXUS, and fitting the XPS data presented in this chapter.

Gillian Collins, University College Cork, Ireland: For collaboration and collection of the TEM images presented in this chapter.

Scott Rogers, Research Complex at Harwell, UK: For preparing TiO_2-supported nanoparticle catalysts for comparison in this chapter.

Tammy Nimmo, University of Southampton, UK: For contributing to the catalytic testing of materials for the oxidation of valerolactam presented in this chapter.

Julie Herniman, University of Southampton, UK: For helpful discussions regarding analysis using GC-MS.

Georgious Kyriakou, Aston University, UK: For conducting catalytic testing on monometallic CuClP materials for the hydrogenation of furfural presented in this chapter.

Stephanie Newland, University of Southampton, UK: For contributing to the catalytic testing of materials for the Beckmann rearrangement of cyclohexanone oxime presented in this chapter.

3.1 Synthesis and Characterisation of Copper Chloropyrophosphates

3.1.1 Monometallic Copper Chlorophosphates

Initially, the hydrothermal synthesis of the undoped and the monometallic copper chlorophosphates (CuClPs) was reproduced from the literature[72] in order to conduct preliminary catalytic testing. The as-synthesised (AS) CuClP, Au/CuClP, Pt/CuClP and Pd/CuClP materials (each approx. 3.5 wt. %) can be seen in Figure 3.1.

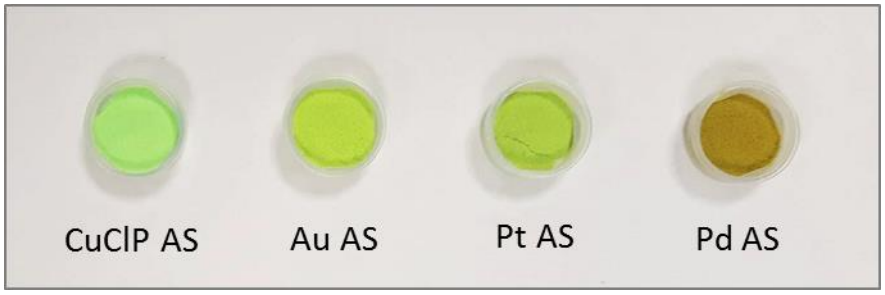

Figure 3.1: Photograph of the as-synthesised CuClP materials.

In Figure 3.2, the measured powder X-ray diffraction (PXRD) pattern for the undoped CuClP material can be compared to a theoretical pattern, and it is possible to see that both patterns are in agreement. PXRD patterns were also collected for the as-synthesised metal-doped frameworks (see Figure 3.3), and they were found to be comparible with the theoretical pattern in Figure 3.2, as well as the PXRD patterns reported by Hinde *et al.*[70] (see Figure A. 4 and Figure A. 5 in the appendix). There are a small number of additional peaks present around 16 ° and 25.5 ° in the Pt/CuClP pattern that are also exclusively present in the Pt/CuClP pattern reported by Hinde *et al*., and as such it is most likely due to the presence of Pt, although this has not been confirmed.

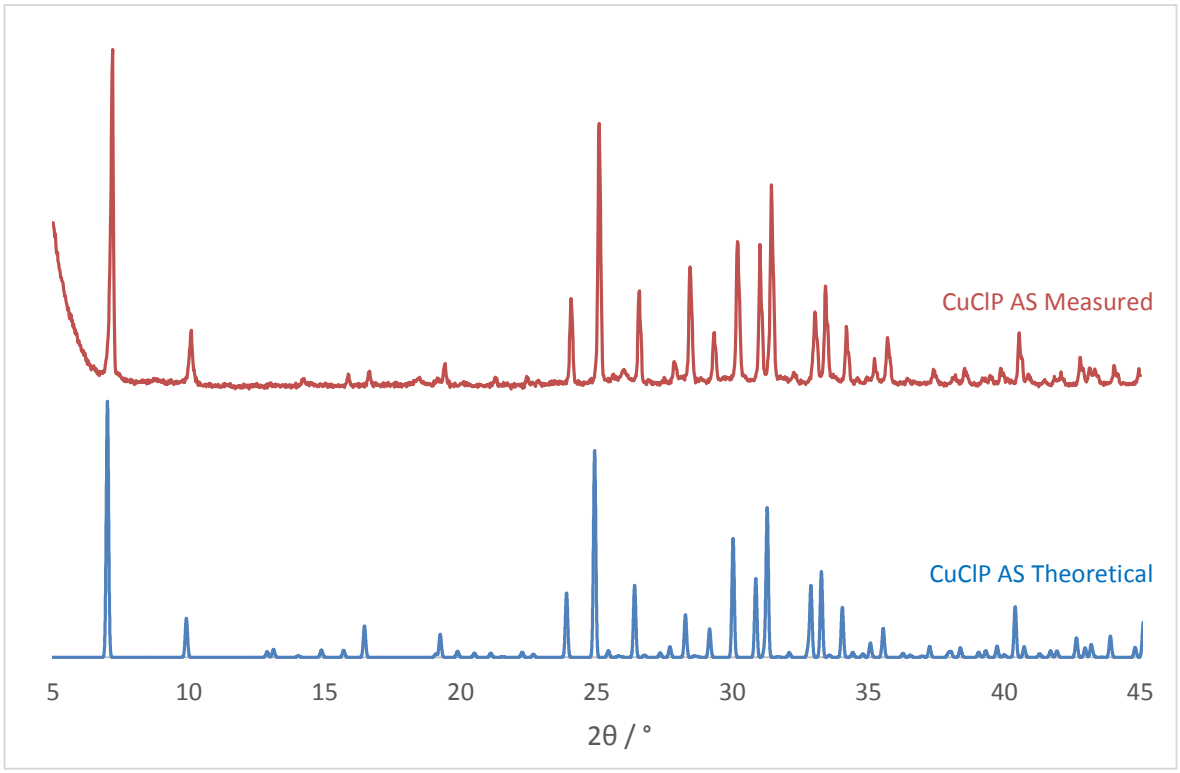

Figure 3.2: Theoretical and measured PXRD patterns for the as-synthesised (AS) CuClP material.

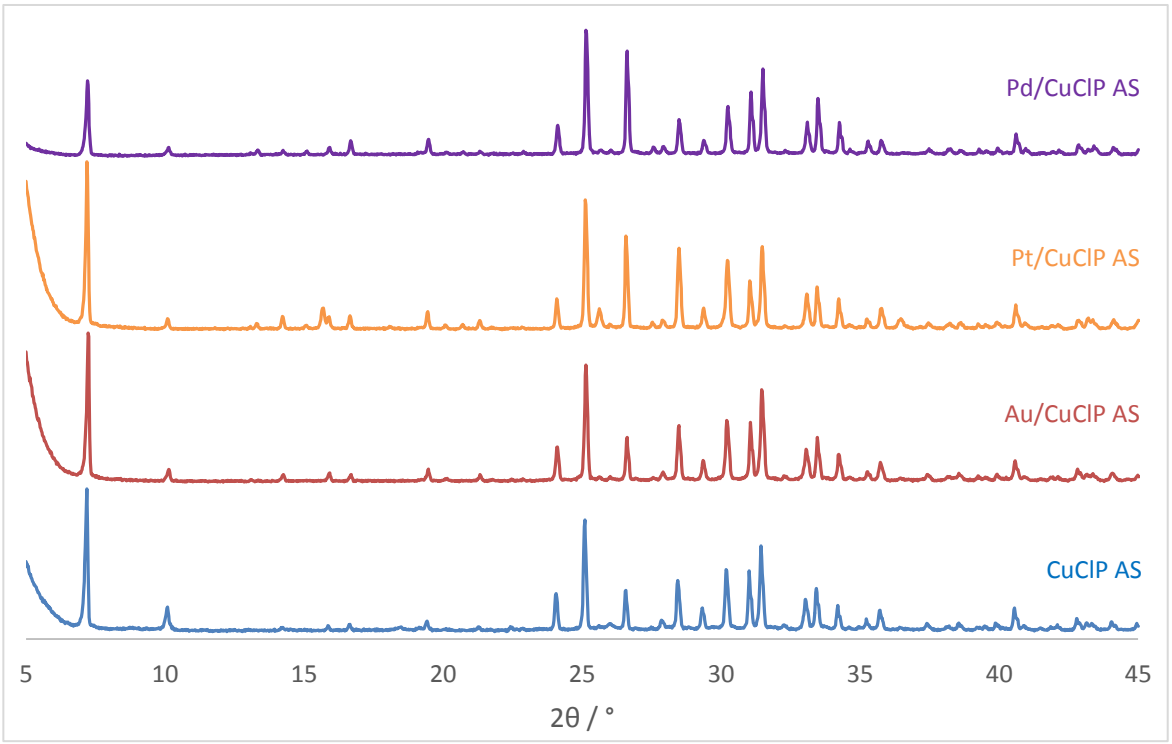

Figure 3.3: PXRD patterns of the as-synthesised (AS) CuClP materials.

Once the synthesis of the monometallic materials was established, the CuClP materials were activated under different reduction temperatures in order to form metallic nanoparticles for catalysis. The reduced CuClP materials are shown below in Figure 3.4, along with the corresponding PXRD patterns in Figure 3.5.

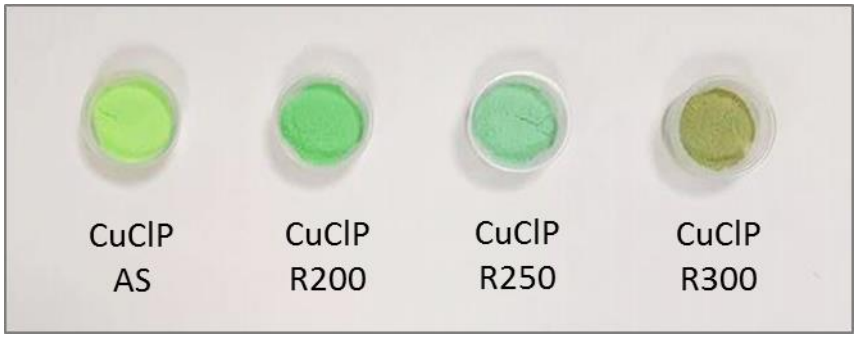

Figure 3.4: Photograph of the as-synthesised and reduced CuClP materials; reduced materials have been activated at 200 °C (R200), 250 °C (R250) and 300 °C (R300).

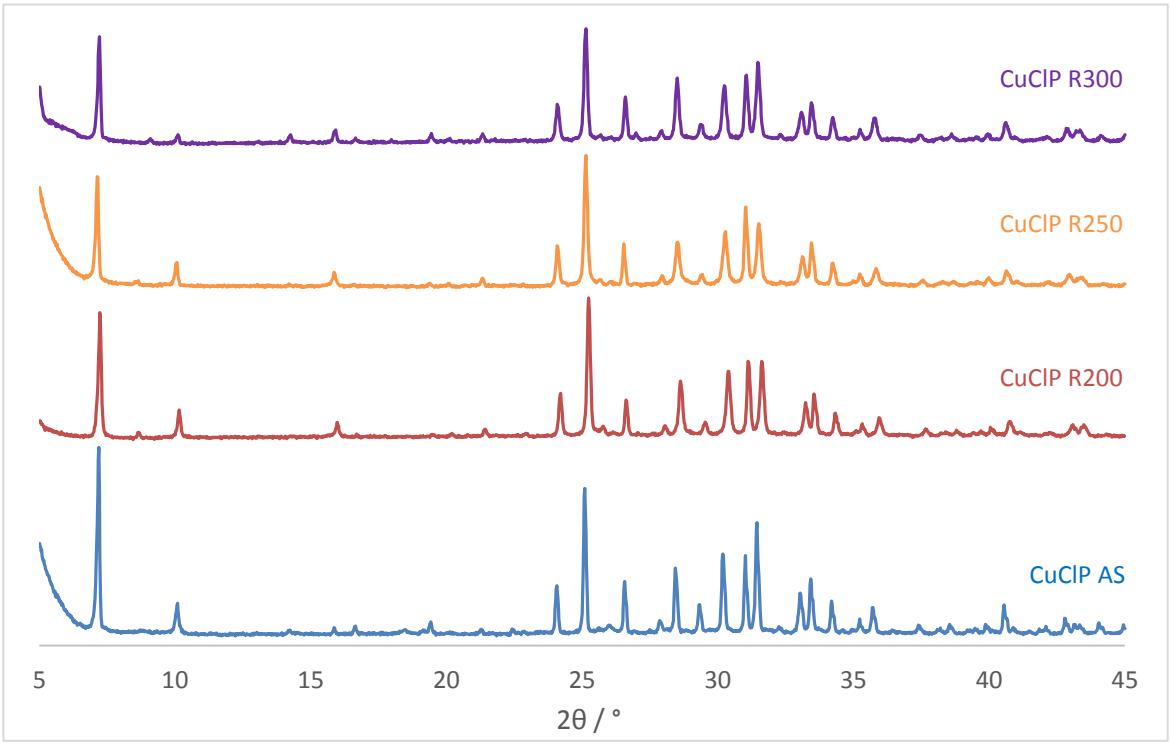

Figure 3.5: PXRD patterns of the as-synthesised and reduced CuClP materials; reduced materials have been activated at 200 °C (R200), 250 °C (R250) and 300 °C (R300).

Figure 3.4 shows a clear change in the CuClP material on reduction, with the material progressing towards khaki green with activation temperature; however, the PXRD patterns remain very similar. As CuClP is the undoped parent framework, no noble metal nanoparticles are expected to form on the surface of the framework, and so no new peaks are expected. However, it is possible that on reduction, the $[CuCl_4]^-$ species that resides in the channels could form Cu nanoparticles on the surface of the support in a manner similar to that reported for the Au/CuClP, Pt/CuClP and Pd/CuClPs. The presence of these Cu nanoparticles could explain the colour change of the CuClP framework on reduction, although their presence has not been confirmed. However, though unpublished, work by A. Gill has found evidence of Au-Cu alloying in the Au/CuClP material reduced at 350 °C using EXAFS and STEM-EDX[74] which could also support the formation of Cu nanoparticles. In the unpublished EXAFS study, data for a Au/CuClP sample reduced at 350 °C shows a large increase in the contribution from Au-Cu, with the change being reflected by a large increase in Au-Cu coordination number from a sample reduced at 250 °C to 350 °C (0.6 to 4.1). Similar evidence of the Au-Cu alloying is seen in STEM-EDX elemental mapping of a Au/CuClP sample reduced at 350 °C, where the Cu species appears to have formed nanoparticles and agglomerated into large particles in the Cu map. Both of these studies allude to the possibility of the extrusion of Cu from the salt template in the channels of the framework to the surface of the material to form nanoparticles.

BET surface areas were measured for the as-synthesised CuClP material and samples reduced at 250 °C and 300 °C, and the results are tabulated in Table 3.1 below (adsorption isotherms can be seen in Figure A. 6 in the appendix).

Table 3.1: Measured BET surface areas for the as-synthesised (AS) and reduced (R) CuClP materials; reduced materials have been activated at 250 °C (R250) and 300 °C (R300).

Material	BET Surface Area / $m^2\ g^{-1}$	BET Pore Volume / $cm^3\ g^{-1}$
CuClP AS	0.8	0.0
CuClP R250	1.7	0.0
CuClP R300	2.3	0.0

From the small measured BET surface areas and pore volumes of 0.0 $cm^3\ g^{-1}$, it is clear that the pores of the CuClP framework were inaccessible, even after reduction. This is most likely due to the salt template remaining inside the channels, and therefore more forcing conditions may be

required in order to fully extrude the salt template, giving rise to larger pore volumes and surface areas. Despite this there is a trend, albeit small, of increasing surface area with activation temperature which could also support the extrusion of $[CuCl_4]^-$ to form Cu nanoparticles on the parent CuClP framework.

The Au/CuClP material was reduced at temperatures between 200 – 300 °C, and samples can be seen in Figure 3.6, along with their corresponding PXRD patterns in Figure 3.7.

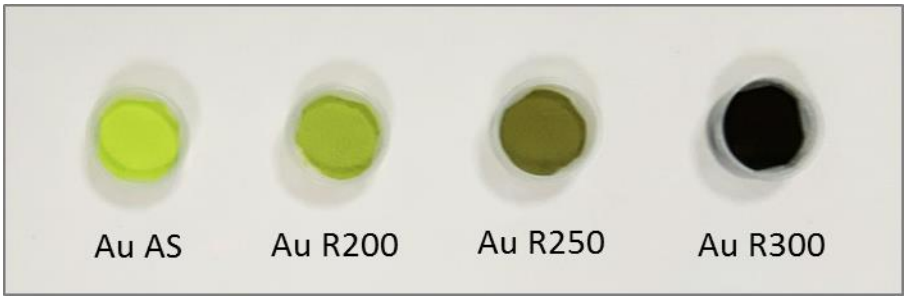

Figure 3.6: Photograph of the as-synthesised and reduced Au/CuClP materials; reduced materials have been activated at 200 °C (R200), 250 °C (R250) and 300 °C (R300).

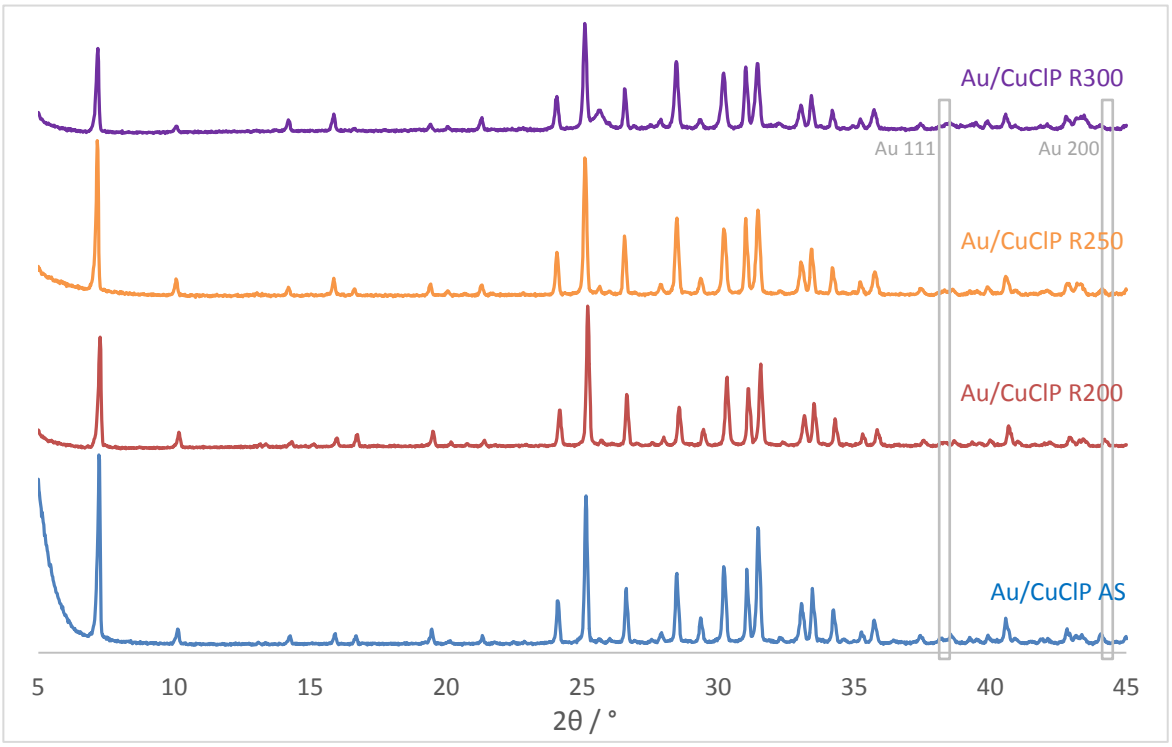

Figure 3.7: PXRD patterns of the as-synthesised and reduced Au/CuClP materials; reduced materials have been activated at 200 °C (R200), 250 °C (R250) and 300 °C (R300).

Similarly to the CuClP material, the Au/CuClP samples get progressively darker, until the dark green/black sample reduced at 300 °C. The PXRD patterns remain similar until the sample reduced at 300 °C, where it is thought that an additional phase is beginning to emerge around 25.4 °. This additional phase is a rubidium phosphate phase and is more pronounced later in Figure 3.9. Due to the dark green/black colour of the sample, along with the additional phase starting to emerge, it is thought that 300 °C is the maximum temperature that the Au/CuClP framework can be activated at before the framework begins to degrade. The presence of metallic Au should be evidenced by additional peaks around 38.2 °(111) and 44.4 ° (200)[124] (regions indicated in Figure 3.7 in grey), however it is unlikely that nanoparticle peaks would be observed due to the low metal loadings of the materials (ca. 3.5 wt. % Au, see Figure A. 9). Due to the low loadings, the expected peaks would be very small in comparison to the parent framework, and as the particles are so small the peaks would also be very broad, so may be indistinguishable from the background, especially if the intensity is very low. The small particle size may also mean that the particles are not crystalline as there is so little bulk material, so peaks may not be present due to their perceived amorphous nature.

The reduced Pt/CuClP materials can be seen in Figure 3.8 below, along with their corresponding PXRD patterns in Figure 3.9.

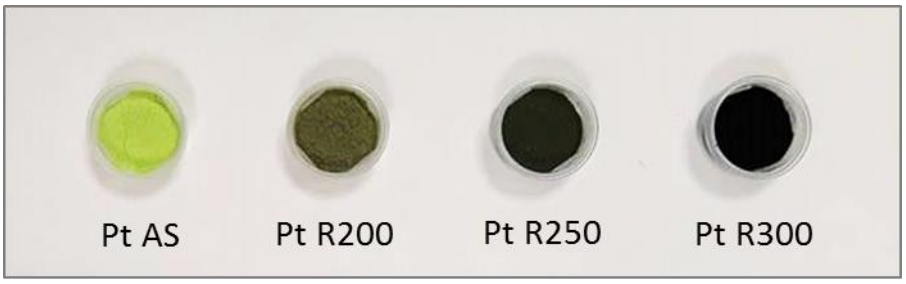

Figure 3.8: Photograph of the as-synthesised and reduced Pt/CuClP materials; reduced materials have been activated at 200 °C (R200), 250 °C (R250) and 300 °C (R300).

The Pt/CuClP materials progress from light green towards a dark green/black with activation temperature, similar to the Au/CuClP material. The PXRD patterns remain largely unchanged until the sample reduced at 300 °C, where the emergence of the rubidium phosphate phase appears as the parent framework degrades. This is not unexpected as, due to the salt-templated nature of the framework, if the rate of extrusion is too high (likely at higher temperatures) it is likely to disrupt

the framework, and hence cause it to break apart. The regions where Pt nanoparticles are expected have been indicated by the grey dashed lines in Figure 3.9, and should be evidenced by additional peaks around 39.9 ° (111) and 46.2 ° (200)[124], however similarly to the Au/CuClP materials, the presence of these tiny peaks are unlikely to be observed due to the small nature of the particles and the low metal loadings of the materials (ca. 3.5 wt. % Pt, see Figure A. 9).

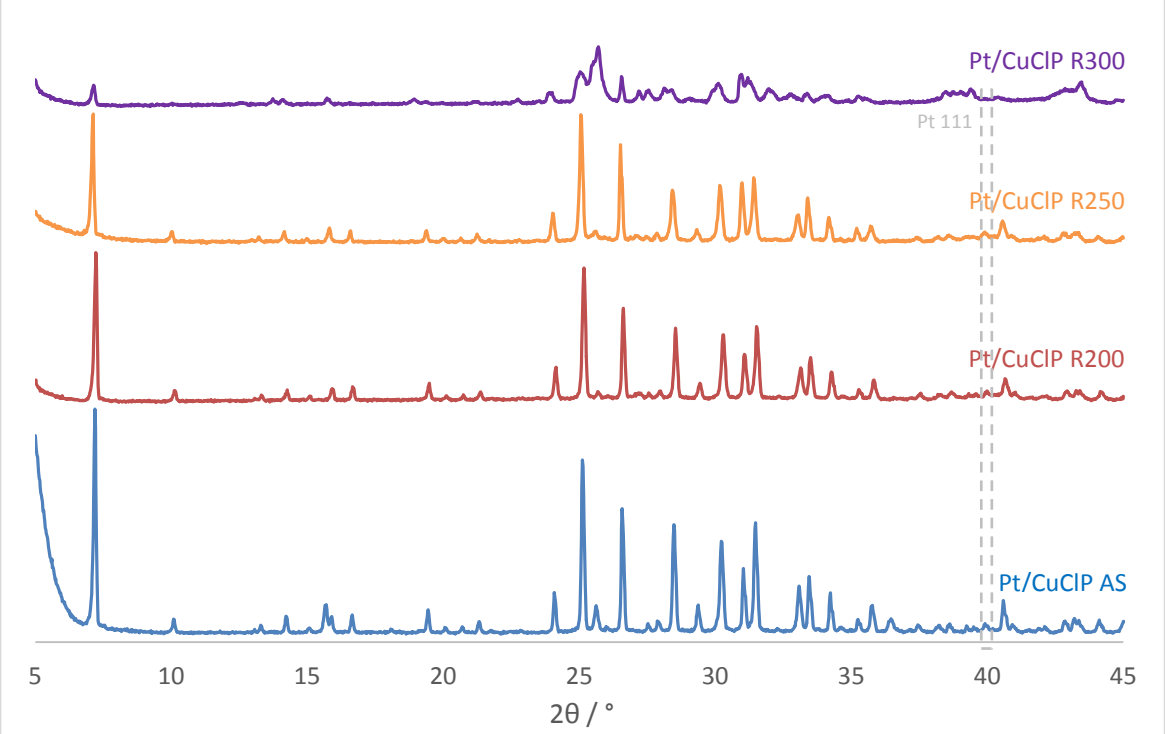

Figure 3.9: PXRD patterns of the as-synthesised and reduced Pt/CuClP materials; reduced materials have been activated at 200 °C (R200), 250 °C (R250) and 300 °C (R300).

The reduced Pd/CuClP materials can be seen in Figure 3.10 below, along with their corresponding PXRD patterns in Figure 3.11.

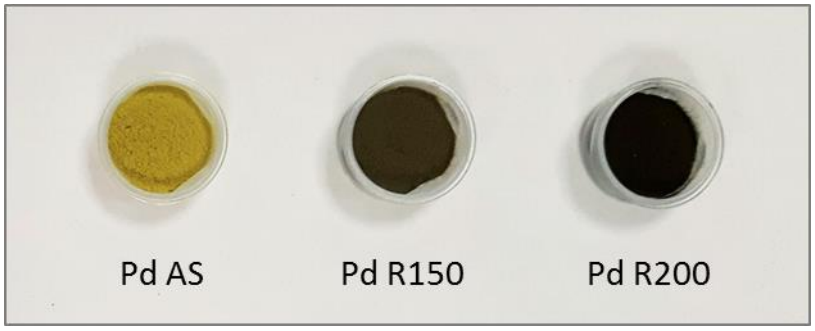

Figure 3.10: Photograph of the as-synthesised and reduced Pd/CuClP materials; reduced materials have been activated at 150 °C (R150) and 200 °C (R200).

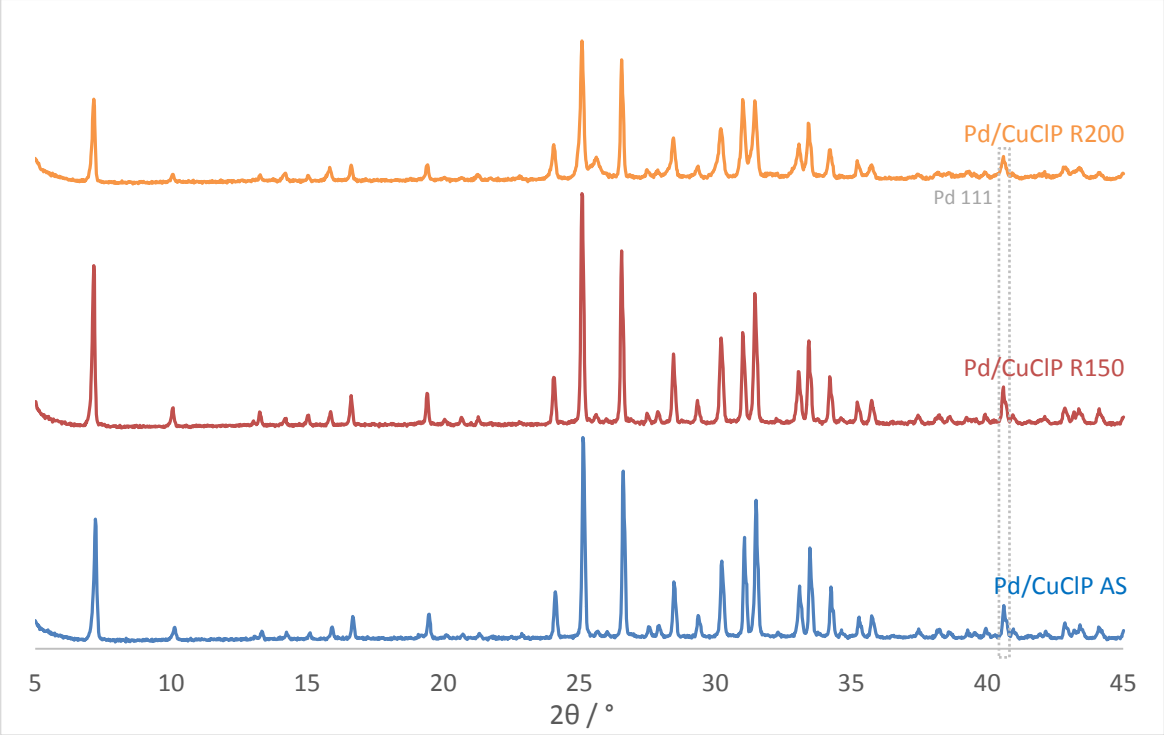

Figure 3.11: PXRD patterns of the as-synthesised and reduced Pd/CuClP materials; reduced materials have been activated at 150 °C (R150) and 200 °C (R200).

Similarly to the Au/CuClP and Pt/CuClP materials, the Pd/CuClP material also gets progressively darker with activation temperature, changing from light brown to dark brown/black. The beginning of the emergence of the rubidium phosphate phase is also clear from the PXRD pattern and the dark brown/black colour of the material reduced at 200 °C, and as such it was hypothesised that the material cannot be activated at temperatures above 200 °C without the framework degrading, which is in agreement with that reported by Gill *et al.*[74]. The lower temperature at which the Pd/CuClP framework degrades could be indicative of stronger interactions between the Pd precursor and the framework in comparison to the Au/CuClP and Pt/CuClP materials. The presence of metallic Pd nanoparticles should be evidenced by additional peaks around 40.6 ° (111) and 46.6 ° (200)[125], and these regions have been highlighted by the grey dotted lines in Figure 3.11. Unfortunately, the metallic Pd region indicated overlaps with a peak from the CuClP framework, and as such it is not possible to tell whether Pd nanopartilces have been formed from PXRD, although, similarly to the Au/CuClP and Pd/CuClP materials, it is unlikely that significant peaks for the Pd nanoparticles would be observed due to the low metal loadings (ca. 3.5 wt. % Pd, see Figure A. 9).

It should be noted that work on the monometallic CuClPs was carried out as a starting point to build upon for the development of bimetallic CuClPs, and as such these materials have not been fully characterised.

3.1.2 Bimetallic Copper Chlorophosphates

Following the work on the monometallic CuClPs, bimetallic variants were synthesised by adapting the synthesis procedure. AuPt/CuClP, PtPd/CuClP and AuPd/CuClP materials (each metal approx. 3.5 wt. %, ICP loadings can be found in Figure A. 9 in the appendix) were synthesised and can be seen in Figure 3.12.

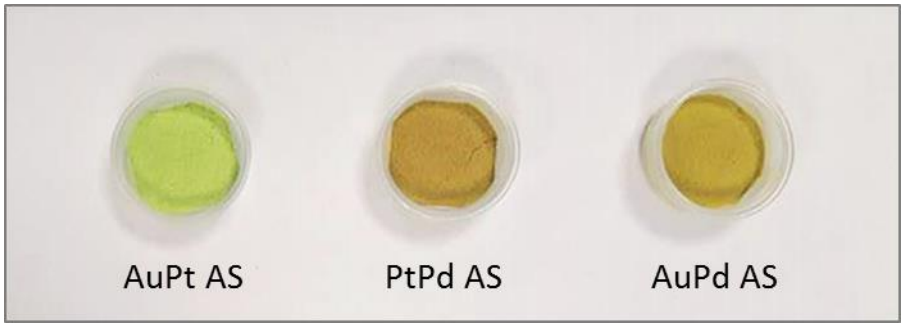

Figure 3.12: Photograph of the as-synthesised bimetallic CuClP materials.

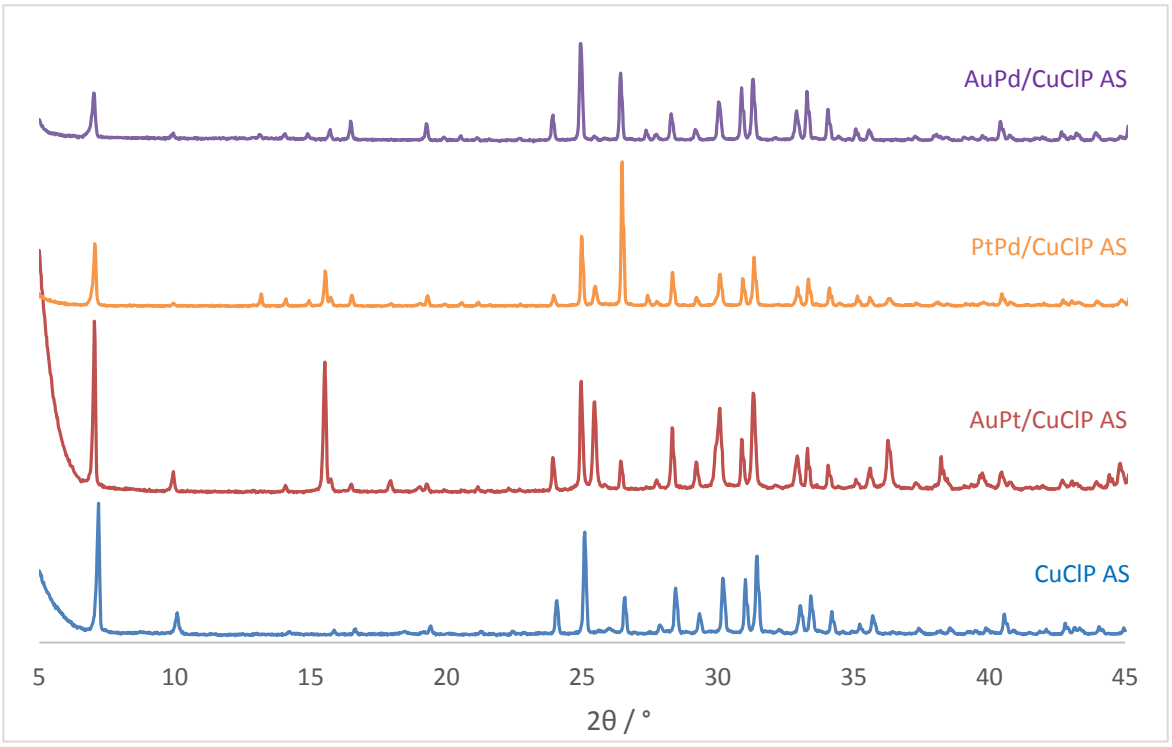

Figure 3.13: PXRD patterns of the as-synthesised (AS) CuClP and bimetallic CuClP materials.

Similarly to the monometallic Pd/CuClP, the Pd-containing bimetallic CuClP materials are brown in colour, with the AuPd/CuClP material being a lighter shade than the PtPd/CuClP. These colour changes from the monometallic CuClP materials potentially hint at the incorporation of both metals into the framework. The PXRD patterns for the bimetallic CuClPs have been compared to the parent framework in Figure 3.13. The bimetallic CuClPs have all retained the CuClP framework and all look similar, with the Pt-containing materials having the same extra peak around 25.5 ° that was present for the monometallic Pt/CuClP. While the patterns clearly show the presence of the CuClP framework, some of the peak intensities have changed on the introduction of the noble metals (most notably the peak around 7 ° in the AuPt/CuClP material, the peak around 15.5 ° for the AuPt/CuClP and PtPd/CuClP materials, and the peak around 26.5 ° for the PtPd/CuClP and AuPd/CuClP materials). Some changes are anticipated due to the substitution of Cu with elements with higher electron densities, which is expected to change the electron density of the unit cell by varying degrees. This change of electron density will be observed in certain lattice planes and will cause certain peak intensities to increase. The substitution of Cu for metals with different charges (Cu^{II} for Au^{III}, Pt^{II} or Pd^{II}) will also change the electron density and may additionally give rise to different coordination geometries, which is also expected to alter peak intensities. The similarity of the AuPd/CuClP and the CuClP patterns suggests that these two materials may adopt a similar geometry, with potentially different geometries adopted by the AuPt/CuClP and PtPd/CuClP materials.

The bimetallic CuClP materials were reduced at a wide range of temperatures, and the AuPt/CuClP materials can be seen in Figure 3.14, along with their corresponding PXRD patterns in Figure 3.15.

Figure 3.14: Photograph of the as-synthesised and reduced AuPt/CuClP materials; reduced materials have been activated at 150 °C (R150), 200 °C (R200), 250 °C (R250), 300 °C (R300), and 350 °C (R350).

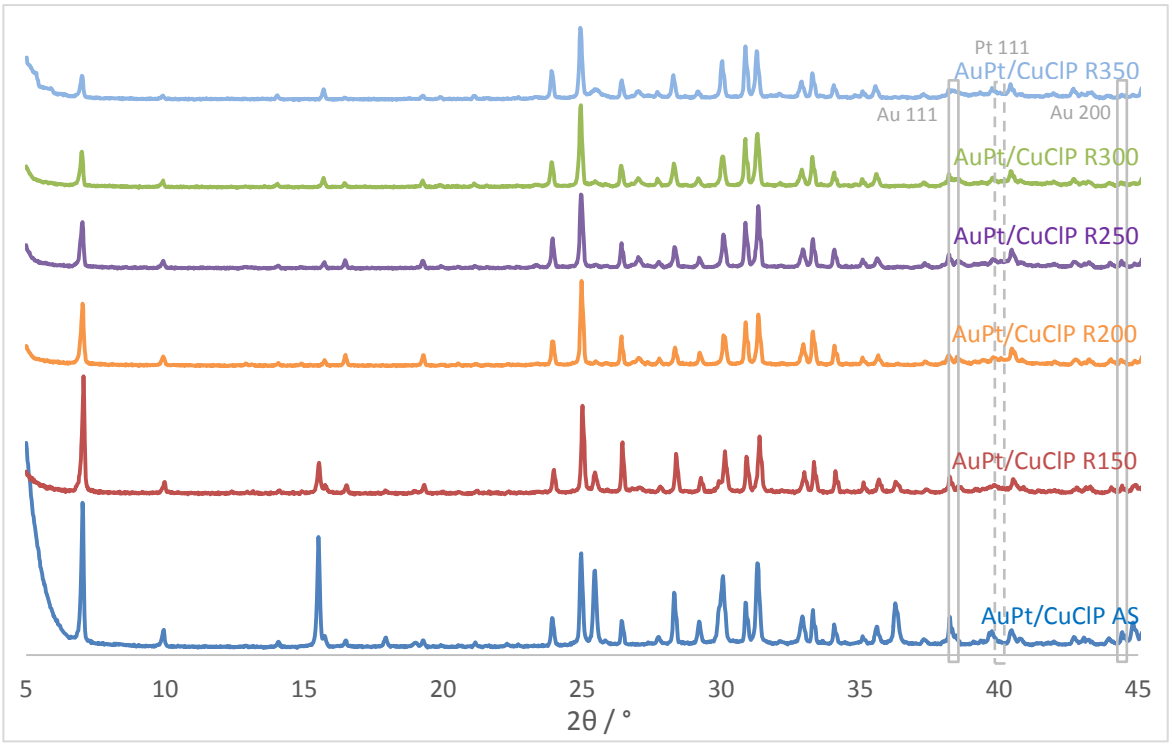

Figure 3.15: PXRD patterns of the as-synthesised and reduced AuPt/CuClP materials; reduced materials have been activated at 150 °C (R150), 200 °C (R200), 250 °C (R250), 300 °C (R300), and 350 °C (R350).

It can be seen that the AuPt/CuClP material gets darker on reduction at higher activation temperatures, progressing from a light green to a dark green. Note how, unlike the monometallic Pt/CuClP, the sample reduced at 300 °C is not dark green/black in colour and does not show any evidence of the rubidium phosphate phase. This suggests that the framework has remained intact, and could be indicative of an interaction between the Au and Pt nanoparticles, as the framework appears to be stable to higher temperatures than the monometallic variants. The intensity of certain framework peaks is likely to decrease with increasing activation temperature as less electron density is expected to be in the channels as the metallic precursor is extruded, and this is indeed observed on reduction for the peaks around 15.5 and 25.5 °. Changes to these peak intensities may also arise from changes in geometry of the Cu in the channels as it changes to accommodate the framework and balance any charges on the extrusion of the metal nanoparticle precursor. The extrusion of the metallic species is also likely to change the symmetry of the unit cell of the framework as it gets less ordered, which may also affect the peaks and their intensities. The presence of metallic Au should be evidenced by additional peaks around 38.2 ° (111), 44.4 ° (200) and 64.6 ° (220)[124] (indicated by the solid grey lines in Figure 3.15, and Figure A. 10 in the appendix), while the presence of metallic Pt should be observed by additional peaks around 39.9 ° (111), 46.2 ° (200) and 67.9 ° (220)[126] (indicated by the dashed grey lines in Figure 3.15, and Figure A. 10 in the

appendix). Due to the low metal loadings (ca. 3.5 wt. % Au and ca. 3.5 wt. % Pt, see Figure A. 9) and small particle sizes, these additional peaks were not observed on the reduction on the material, just as the nanoparticle peaks were not observed for the monometallic CuClP materials. For completeness, PXRD patterns for as-synthesised AuPt/CuClP and a sample reduced at 300 °C, ranging from 5 – 75 °, can be seen in Figure A. 10 in the appendix.

BET surface areas were measured for the as-synthesised AuPt/CuClP material and a sample reduced at 300 °C, and the results are tabulated in Table 3.2 below (adsorption and desorption isotherms can be seen in Figure A. 7 and Figure A. 8 in the appendix). Similarly to the parent CuClP framework, the measured BET surface areas of the AuPt/CuClP materials are very small in comparison to other nanoporous materials such as aluminophosphates (AlPOs) (e.g. AlPO-5 typically has surface areas of ca. 250 $m^2\ g^{-1}$)[127] and mesoporous silicas (e.g. SBA-15 has surface areas between 700 – 800 $m^2\ g^{-1}$)[128]. The tiny measured surface areas of these materials suggest that the channels of the CuClP materials will not become accessible unless more forcing conditions can promote complete extrusion of the species occupying them. As such, it would be more appropriate to think of the CuClP framework as a non-porous support that facilitates the *in situ* generation of metallic nanoparticles.

Table 3.2: Measured BET surface areas for the as-synthesised (AS) and reduced (R) AuPt/CuClP materials; reduced material had been activated at 300 °C (R300).

Material	**BET Surface Area / $m^2\ g^{-1}$**	**BET Pore Volume / $cm^3\ g^{-1}$**
AuPt/CuClP AS	1.4	0.0
AuPt/CuClP R300	1.4	0.0

Transmission electron microscopy (TEM) was used in order to evaluate the extent of nanoparticle formation in the AuPt/CuClP material reduced at a range of different temperatures. TEM images for the AuPt/CuClP material reduced at 200 °C, 250 °C, 300 °C and 350 °C are shown in Figure 3.16. Images were collected by G. Collins, University College Cork, Ireland.

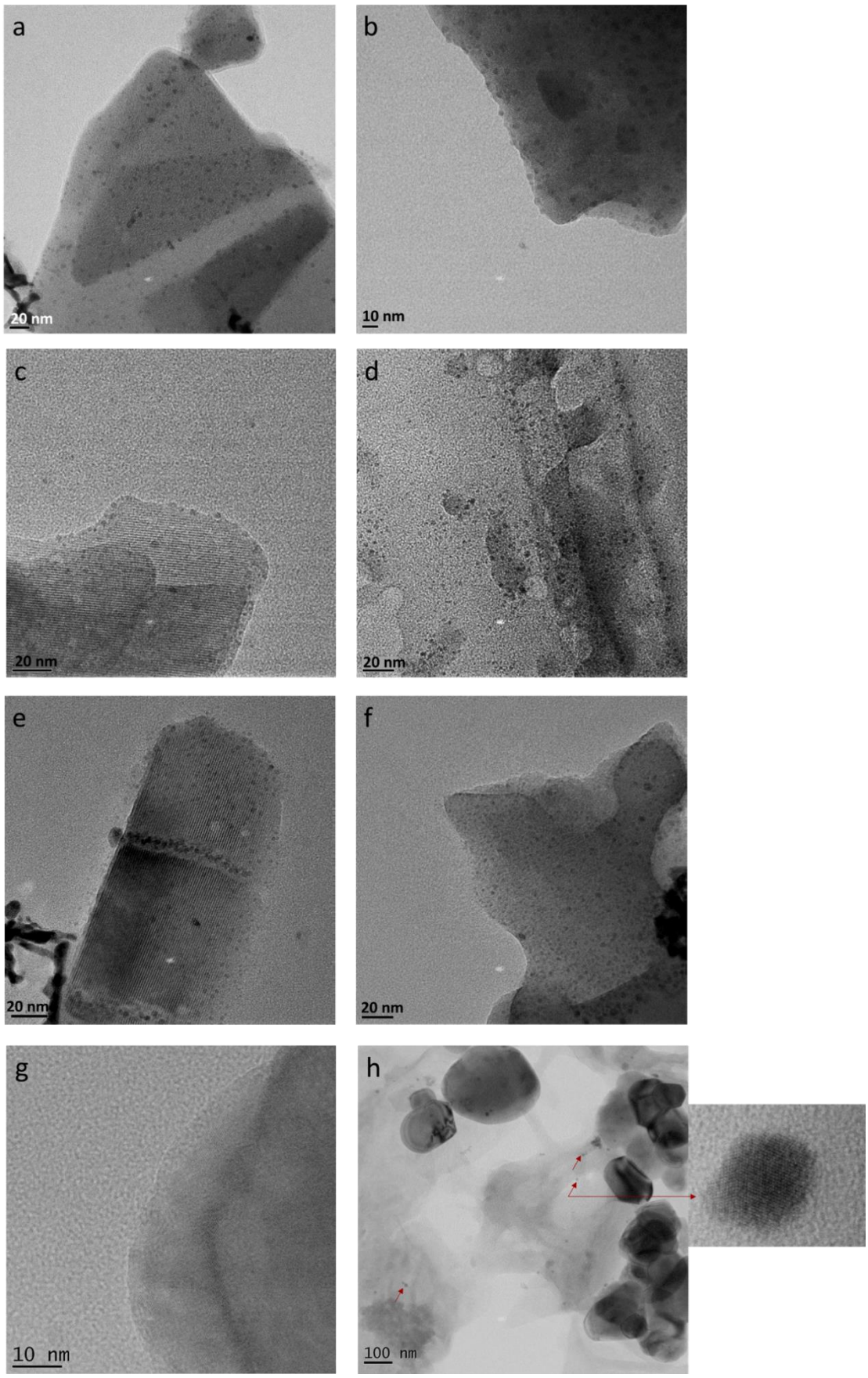

Figure 3.16: TEM images of the AuPt/CuClP material reduced at 200 °C (a – b), 250 °C (c – d), 300 °C (e – f), and 350 °C (g – h); images collected by G. Collins, University College Cork, Ireland.

The crystalline structure of the CuClP framework is present in the TEM images for all of the samples, with the appearance of small and uniform nanoparticles in the materials reduced between 200 – 300 °C (a – f). At 350 °C, the small nanoparticles are no longer clearly visible (g), however large irregular shapes and a small number of larger nanoparticles (ca. 8 nm) were observed (h). The identity of the larger structures is unknown, however it is possible that sintering may be responsible for the formation of the larger nanoparticles as it is well known that the presence of chloride can induce sintering, especially at high temperatures[73]. As such, it is recommended that the reduction process should take place at as low a temperature as possible, with the shortest contact time in order to suppress any precursor mobility that would lead to nanoparticle sintering. It is also possible that these larger nanoparticles could be a result of any potential Au-Cu alloying that has been evidenced by A. Gill in the work on the monometallic Au/CuClP material reduced at 350 °C. Interestingly, there is a region of high nanoparticle density in the sample reduced at 300 °C (e) which appears to be located in a surface defect. Further characterisation is required in order to probe this in more detail and determine whether this is due to the extrusion process or due to the mobility of nanoparticles after formation. Note also that the presence of amorphous regions within the samples (predominantly d) suggest that the synthesis procedure needs to be optimised further.

XPS data was collected for the reduced AuPt/CuClP materials reduced at a range of activation temperatures (see Figure 3.17), and from the data it is possible to see that Au^0 is dominant across all of the samples, with no apparent contribution from Au^{III}. This was unexpected as it disagrees with the monometallic XPS reported by Gill *et al.*[74], where it was reported that higher temperatures (> 250 °C) were required to form metallic Au nanoparticles. It is possible that the presence of Pt in the bimetallic AuPt/CuClP material could influence the formation of Au nanoparticles, allowing them to fully extrude and form at lower temperatures. Unlike the monometallic Pt/CuClP XPS, the bimetallic data suggests that the AuPt/CuClP samples are predominantly Pt^0 across all activation temperatures, showing no contribution from Pt^{II}. As such, it can be hypothesised that there is a synergistic interaction between the Au and the Pt nanoparticles in the AuPt/CuClP material, with the presence of each metal potentially lowering the temperature required to form nanoparticles of the other. However, it is not possible to comment on the nature of these nanoparticles as it is unknown whether they form discrete sites or alloyed particles.

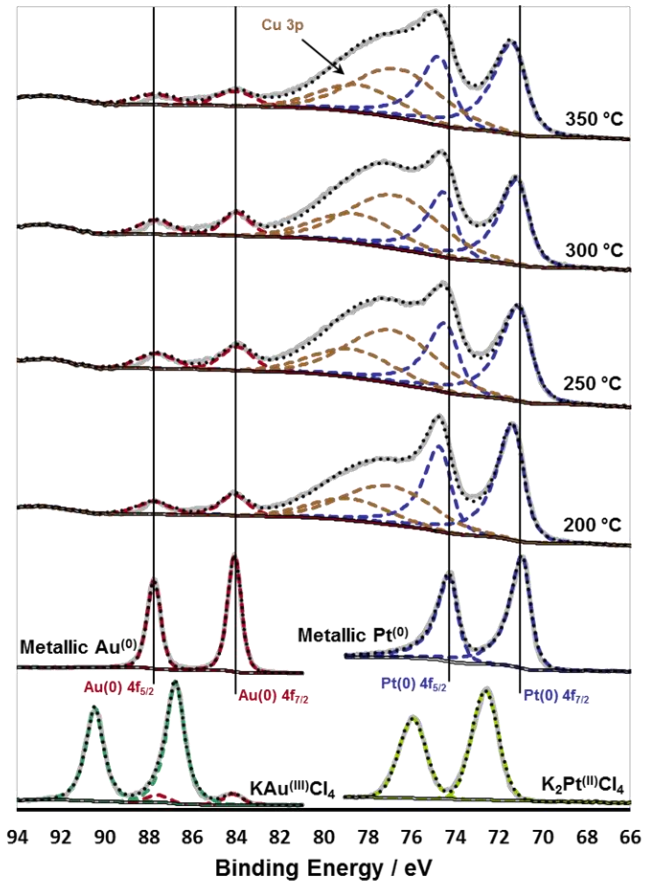

Figure 3.17: Au and Pt XPS spectra for the AuPt/CuClP material reduced at different activation temperatures; data fitted by A. Gill.

The bimetallic PtPd/CuClP materials were reduced at a range of temperatures, and can be seen in Figure 3.18, along with their corresponding PXRD patterns in Figure 3.19.

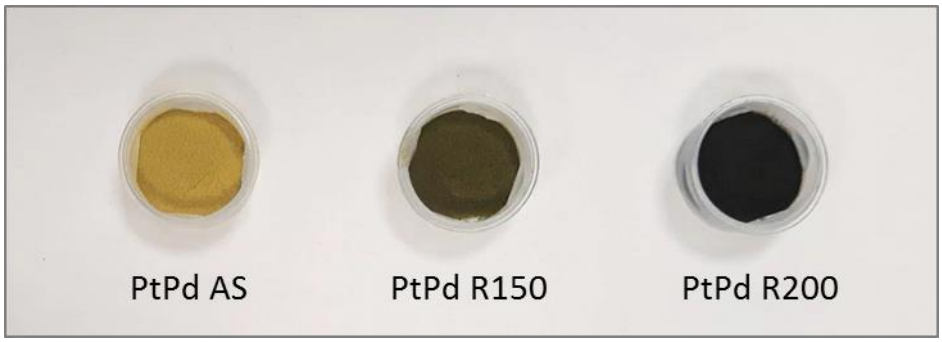

Figure 3.18: Photograph of the as-synthesised and reduced PtPd/CuClP materials; reduced materials have been activated at 150 °C (R150) and 200 °C (R200).

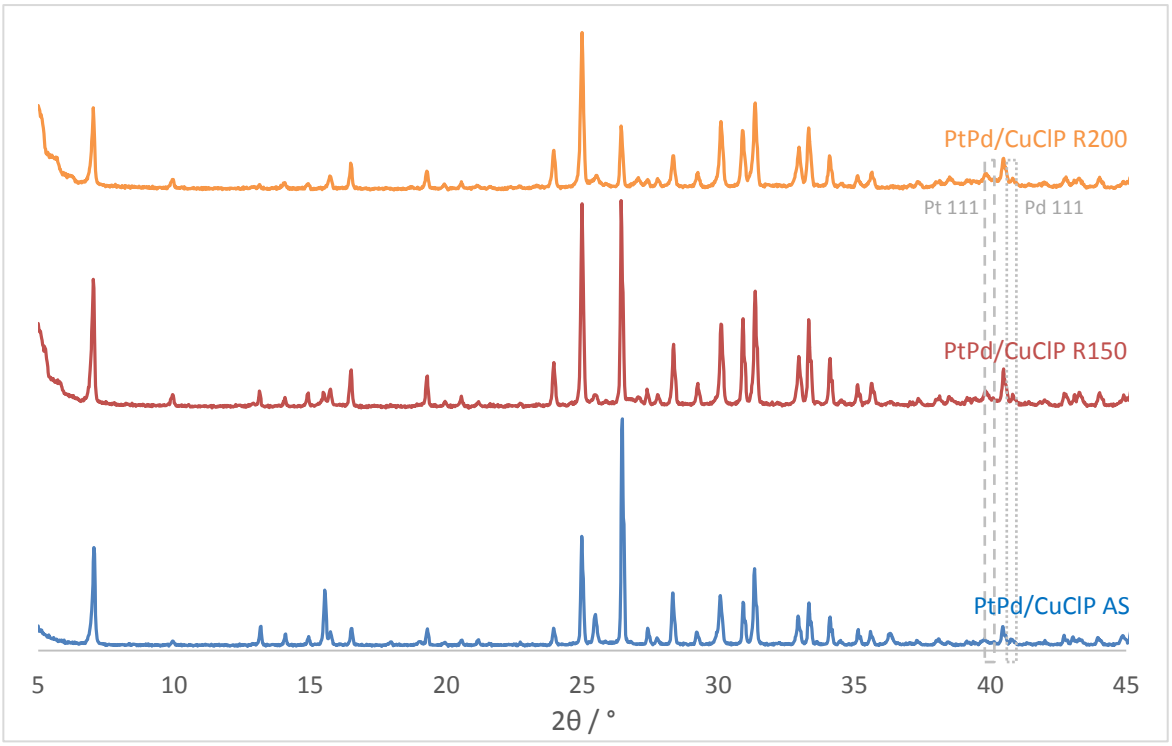

Figure 3.19: PXRD patterns of the as-synthesised and reduced PtPd/CuClP materials; reduced materials have been activated at 150 °C (R150) and 200 °C (R200).

It can be seen that the PtPd/CuClP material gets darker with an increase in activation temperature, retaining the dark brown colour associated with Pd/CuClP samples. Similarly to the AuPt/CuClP material, the presence of another metal, in this case Pt, appears to have marginally increased the thermal stability of the PtPd/CuClP material, which was found to be stable up to 225 °C, 25 °C higher than the monometallic Pd/CuClP. Similarly to the monometallic Pt/CuClP and Pd/CuClP materials, any additional peaks expected due to metallic Pt (nanoparticle regions indicated by the solid grey lines in Figure 3.19, and Figure A. 11 in the appendix) and Pd (metallic Pd expected around 40.6 ° (111), 46.6 ° (200) and 68.4 ° (220)[125], highlighted by the dotted grey lines in Figure 3.19, and Figure A. 11 in the appendix) were not observed due to the low metal loadings (ca. 3 wt. % Pt and ca. 2 wt. % Pd, see Figure A. 9). For completeness, PXRD patterns for as-synthesised PtPd/CuClP and a sample reduced at 200 °C, ranging from 5 – 75 °, can be seen in Figure A. 11 in the appendix.

TEM images collected of the PtPd/CuClP material reduced at 150 °C and 200 °C clearly show the presence of nanoparticles in both samples, although nanoparticles appear to be much more prevalent in the sample reduced at 150 °C. This was unexpected as it was thought that higher temperatures were more likely to produce nanoparticles, however it is possible that the image collected is not representative of the whole sample. It is also worth noting that the nanoparticles

appear larger than those observed for the AuPt/CuClP sample, and this is most likely due to the propensity of Pd to form larger particles, as observed in the monometallic TEM[70].

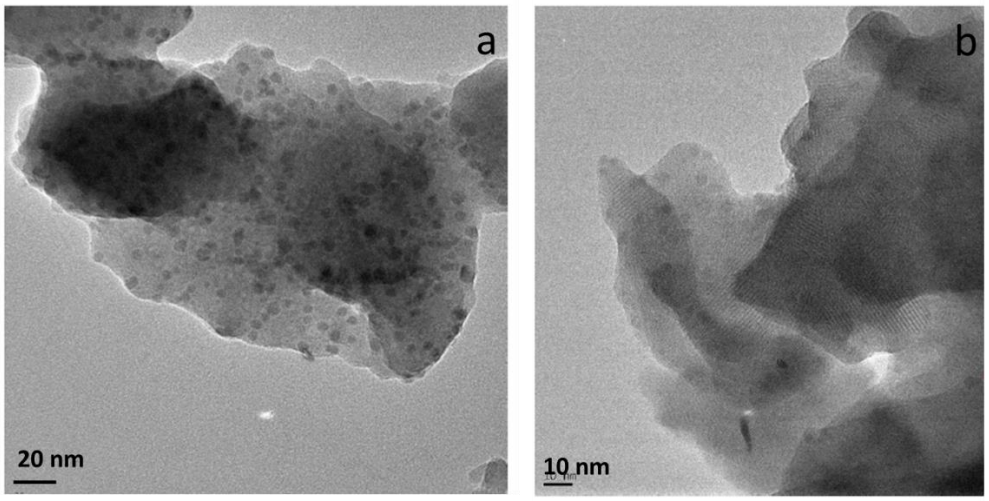

Figure 3.20: TEM images of the PtPd/CuClP material reduced at 150 °C (a) and 200 °C (b); images collected by G. Collins, University College Cork, Ireland.

XPS data was collected for reduced samples of the PtPd/CuClP material, and can be seen in Figure 3.21. The XPS data collected for the PtPd/CuClP shows mild progressive formation of Pd^0 and loss of Pd^{II} with reduction temperature, in agreement with monometallic Pd/CuClP XPS data. However, unlike the AuPt/CuClP, there is also progressive formation of Pt^0 with reduction temperature, in agreement with the monometallic Pt/CuClP XPS data, suggesting that the presence of Pd in the framework might not encourage facile Pt nanoparticle formation, unlike the presence of Au in the AuPt/CuClP material. Although it was perhaps originally overlooked, the presence of Pt^{IV} was noticed in the bimetallic sample, it's position in good agreement with the literature[129]. The presence of Pt^{IV} could suggest that the Pt extrusion process in the monometallic Pt/CuClP and the bimetallic PtPd/CuClP materials is not as efficient or controlled as originally thought, with the process potentially giving rise to a range of Pt oxidation states.

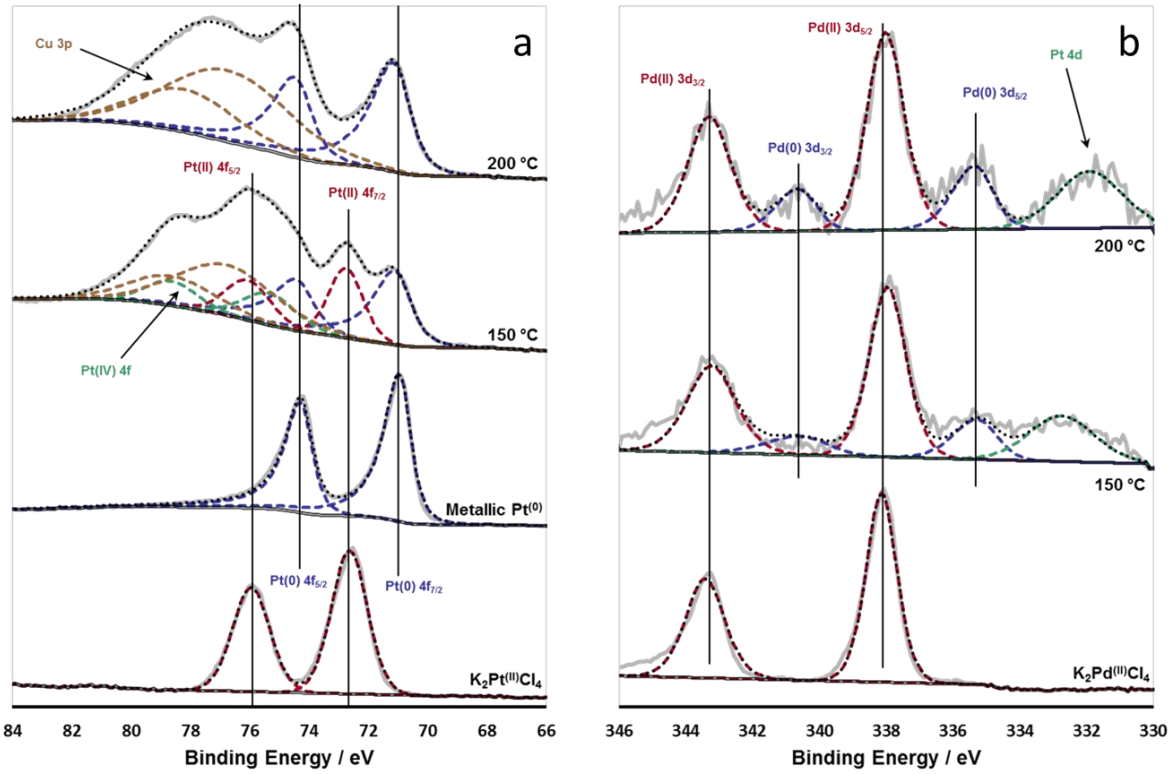

Figure 3.21: (a) Pt and (b) Pd XPS spectra for the PtPd/CuClP material reduced at different activation temperatures; data fitted by A. Gill.

The bimetallic AuPd/CuClP materials were reduced at a range of temperatures, and can be seen in Figure 3.22, along with their corresponding PXRD patterns in Figure 3.23.

Figure 3.22: Photograph of the as-synthesised and reduced AuPd/CuClP materials; reduced materials have been activated at 150 °C (R150) and 200 °C (R200).

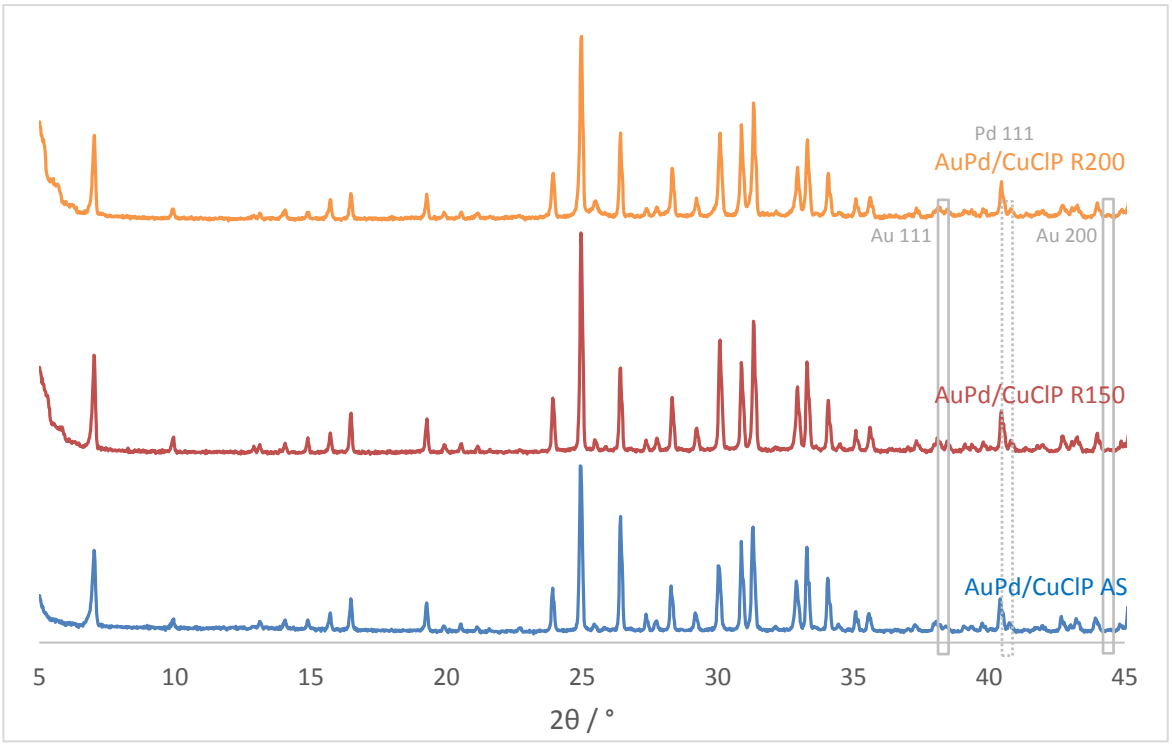

Figure 3.23: PXRD patterns of the as-synthesised and reduced AuPd/CuClP materials; reduced materials have been activated at 150 °C (R150) and 200 °C (R200).

Similarly to the PtPd/CuClP material, the brown AuPd/CuClP material gets darker with increased reduction temperature. As with the PtPd/CuClP, the presence of Au also appears to have increased the thermal stability of the material, which was also found to be stable until 225 °C. This is reflected in the PXRD pattern of the sample reduced at 200 °C, as there is no evidence of the degradation of the framework. Once again, the additional peaks expected for metallic Au (nanoparticle regions highlighted by the solid grey lines in Figure 3.23, and Figure A. 12 in the appendix) and Pd (nanoparticle regions highlighted by the dotted grey lines in Figure 3.23, and Figure A. 12 in the appendix) were not observed due to the low metal loadings (ca. 2 – 3 wt. % Au and ca. 2 wt. % Pd, see Figure A. 9), and a PXRD pattern for as-synthesised AuPd/CuClP and a sample reduced at 200 °C, ranging from 5 – 75 °, can be seen in Figure A. 12 in the appendix.

The crystalline framework and clear nanoparticles can be seen in the TEM images collected for the AuPd/CuClP materials reduced at 150 °C and 200 °C (see Figure 3.24). The samples appear to have a larger size distribution of nanoparticles than the PtPd/CuClP and AuPt/CuClP materials, with the AuPt/CuClP material having the smallest and most uniform particles of the bimetallic materials. The presence of larger particles is likely due to the incorporation of Pd, as larger particles were also found to be more prevalent in the monometallic Pd/CuClP material[72]. It is worth noting that the sample reduced at 150 °C appears to have a similar high nanoparticle density feature as observed

in the AuPt/CuClP sample reduced at 300 °C, which could allude to a propensity to form such surface features.

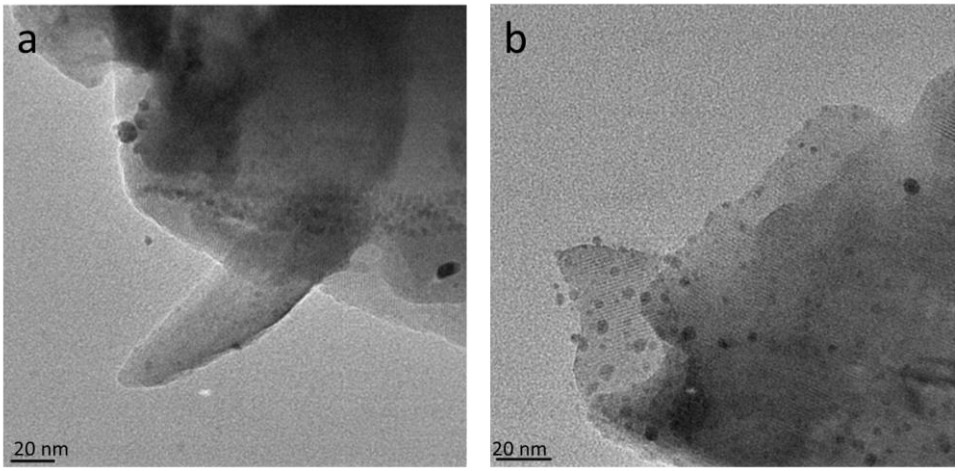

Figure 3.24: TEM images of the AuPd/CuClP material reduced at 150 °C (a) and 200 °C (b); images collected by G. Collins, University College Cork, Ireland.

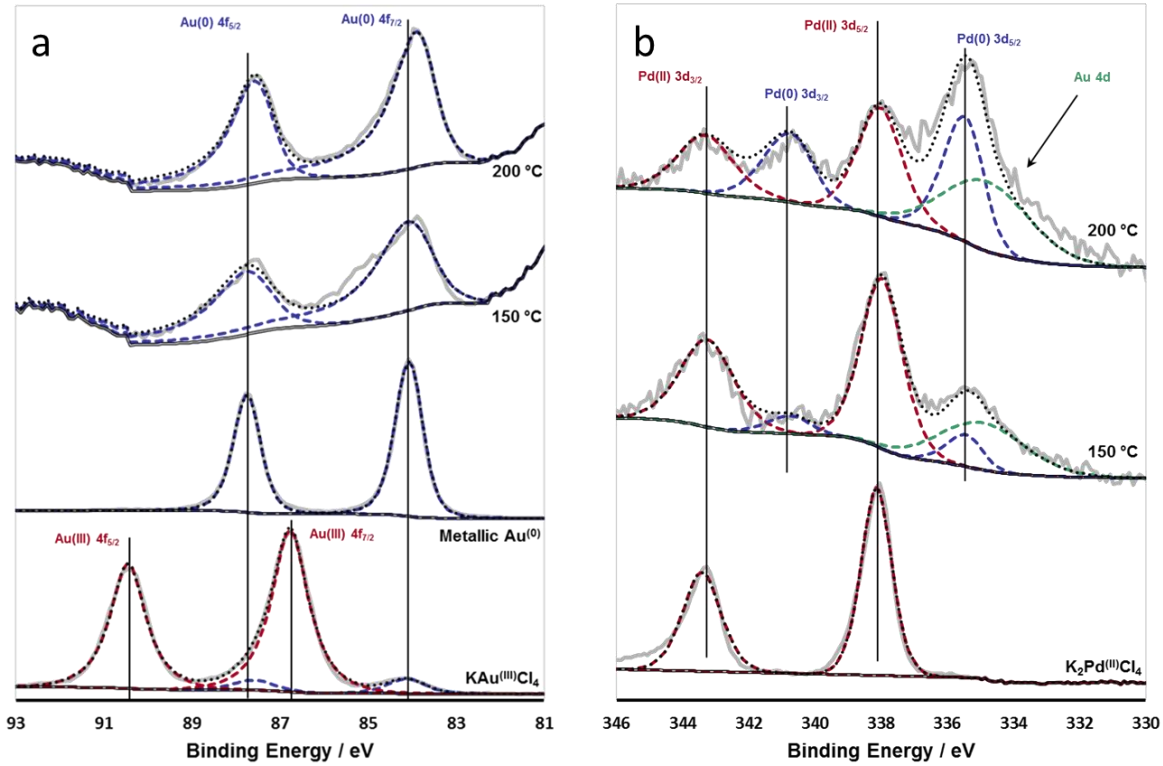

Figure 3.25: (a) Au and (b) Pd XPS spectra for the AuPd/CuClP material reduced at different activation temperatures; data fitted by A. Gill.

Similarly to the AuPt/CuClP material, the XPS data (see Figure 3.25) for the AuPd/CuClP samples reduced at 150 °C and 200 °C shows a predominant contribution from Au^0 across all of the samples, and as such it is possible that the presence of Pd may also promote Au nanoparticle formation. There is also a mild progression from Pd^{II} to Pd^0 with reduction temperature, although a mixture of oxidation states is still present in the sample reduced at 200 °C. It is likely that the Pd/CuClP and Pd-containing bimetallic CuClPs require higher temperatures to extrude to form nanoparticles, even in the presence of Au, although the framework is limited by its thermal stability.

3.2 Catalysis

3.2.1 Oxidation of KA-Oil

Monometallic Copper Chlorophosphates

Preliminary catalytic testing using the monometallic CuClP materials for the aerobic oxidation of KA-oil was initially carried out to provide a foundation to build upon with the bimetallic catalysts. The oxidation of KA-oil (see Figure 3.26) was conducted in the vapour phase at 200 °C using air as the oxidant using 3.5 wt. % monometallic catalysts, and the results can be seen in Table 3.3. All reaction parameters have been tabulated in Figure A. 16 in the appendix.

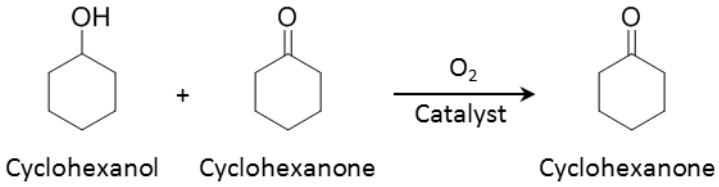

Figure 3.26: Oxidation of KA-oil (1:1 ratio cyclohexanol to cyclohexanone) to cyclohexanone.

A range of reduction temperatures were screened in order to probe the activity of the monometallic CuClPs, while keeping the CuClP framework intact. A series of blank reactions, using no catalyst and using the as-synthesised CuClP catalyst (first two entries in Table 3.3), were also carried out to test for uncatalysed reactions. As hoped, the blank reactions, using no catalyst and as-synthesised CuClP, showed no activity in the oxidation of KA-oil, meaning that any conversion observed in the reaction can be accredited to the catalyst used.

Table 3.3: Screening for KA-oil oxidation activity; 1:1 ratio KA-oil feedstock, 0.20 g catalyst (3.5 wt. %), 15 µL min^{-1} substrate flow rate, 25 mL min^{-1} air flow rate, 200 ° C, 1 hr on stream.

Catalyst	Reduction Temperature / °C	Conversion / mol %	Cyclohexanone Selectivity / %	TOF / hr^{-1}
None	N/A	0	0	N/A
CuClP	-	0	0	0
	300	0	0	0
Au/CuClP	250	0	0	0
	300	0	0	0
Pt/CuClP	200	59	> 99	63
	250	69	> 99	82
Pd/CuClP	150	0	0	0
	200	0	0	0

Interestingly, no activity was observed for the CuClP material reduced at 300 °C, either disproving the notion of forming Cu nanoparticles from the parent framework or suggesting that Cu nanoparticles are not active in the reaction. However, as Cu has been reported to be active in the oxidation of cyclohexanol[95,113], the latter is unlikely. This absence of activity in the CuClP framework reduced at high temperatures is useful however, as any activity of catalysts reduced at these temperatures can be accredited to the nanoparticles on the material, as opposed to the framework itself. Of the three nanoparticle catalysts, the Pt/CuClP material appeared to be the only active material, with the Au/CuClP and Pd/CuClP catalysts being inactive regardless of the activation temperature. This disagrees with the results reported by Gill *et al*.[74], whereby all of the monometallic CuClP materials were active. However, the catalysts used by Gill *et al*. had higher metal loadings (7 wt. % c.f. 3.5 wt. %), and the conversions observed were very low for the Au/CuClP and Pd/CuClP materials (ca. 1 – 5 mol %). As such, this difference is most likely due to sample differences, and it is likely that using a higher metal loading would afford the same trend. Despite the lower metal loading, a similar trend was observed for the Pt/CuClP materials whereby the conversion increased with activation temperature. Lower metal loadings were adopted in this work in order to improve the design of the materials, through encouraging more controlled nanoparticle formation and discouraging nanoparticle sintering, and in order to increase the catalytic efficiency.

Note that the selectivity for the reaction has been quoted as > 99 % as only one product, cyclohexanone, was detected by GC. The absence of the by-product cyclohexene, commonly formed from the dehydration of cyclohexanol, suggests the absence of strong acid sites in the materials, as it has been found that the dehydration reaction requires strong acids in order to commence[130].

After the initial testing, studies were carried out to see the effects of varying the temperature, the substrate flow rate, and the air flow rate on the conversion and selectivity of the reaction, with an aim to optimise the oxidation. Studies were carried out using 7 wt. % Pt/CuClP material reduced at 200 °C. All reaction parameters can be found in Figure A. 17 in the appendix.

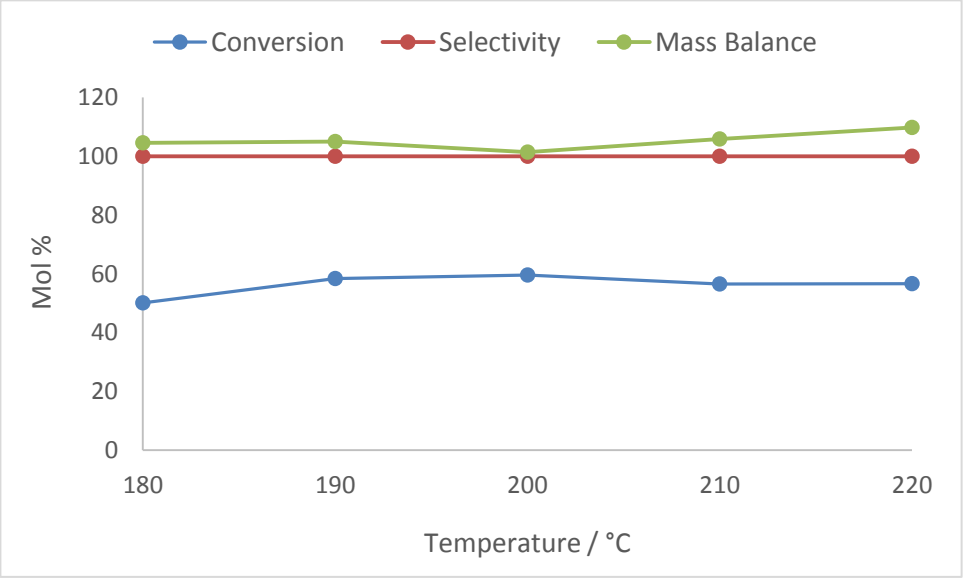

Figure 3.27: Plot showing the change in conversion, selectivity and mass balance as the temperature is varied in the oxidation of KA-oil using 7 wt. % Pt/CuClP reduced at 200 °C; 1:1 ratio KA-oil feedstock, 0.20 g catalyst, 15 µL min^{-1} substrate flow rate, 25 mL min^{-1} air flow rate, 180 – 220 ° C, 1 hr on stream.

The reaction temperature was varied from 180 – 220 °C, and the results are shown in Figure 3.27. Over the temperature range investigated it can be seen that the conversion, selectivity and the mass balance remains fairly constant, with the best conversion and mass balance being achieved at 200 °C. The lack of change in conversion indicates that the reaction is not temperature dependent in this temperature range, suggesting that the temperatures tested were above the activation temperature for the reaction. This observation can be explained using the Arrhenius equation in Equation 3.1, indicating the temperature dependence of reaction rates.

$$k = Ae^{-\frac{E_a}{RT}}$$

Equation 3.1: Arrhenius equation highlighting the temperature dependence of reaction rates, where k is the rate constant (units dependent on the order of reaction), A is the pre-exponential factor (units same as k), E_a is the activation energy (J mol^{-1}), R is the ideal gas constant (8.314 J K^{-1} mol^{-1}) and T is the temperature (K).

Below the activation temperature for a reaction (at small values of T), the value of exp(-E_a/RT) is small, and as a result the rate constant, k, is also small resulting in a very slow rate of reaction. When the activation temperature is reached, the value of exp(-E_a/RT) becomes much larger, giving rise to a larger value of k, and a faster rate of reaction. However, once the activation energy has been reached, the effect of temperature on the rate of the reaction becomes much smaller. This is because as the value of T becomes very large, the value of exp(-E_a/RT) tends towards 1, and it's effect in the Arrhenius equation becomes negligible, resulting in little change in the rate. It is worth noting that a lower temperature range was not explored due to the high boiling points of cyclohexanol and cyclohexanone being 161 °C and 156 °C respectively. As the reaction was to take place in the vapour phase it was important that the temperature was high enough to vaporise the substrate flow before the catalyst bed was reached.

The air flow rate was varied between 10 – 40 mL min^{-1} in order to determine the effect of increasing the quantity of oxygen in the system (see Figure 3.28). From the graph it is clear that the rate of the reaction is clearly dependent on the quantity of oxygen in the system, as observed by the increase in conversion with increased quantities of oxygen. This was expected as the greater the amount of oxygen available in the system for reaction, the more substrate will react with the oxygen, increasing the conversion. This increase in conversion was also met with a decrease in mass balance which could be attributed to the conversion of cyclohexanol to products that could not be detected by GC. It is worth noting that the observed mass balance for this study was over-inflated (see Figure A. 17 in the appendix) and as such the mass balances were normalised relative to a zero point sample, a point where there is no conversion. The over-inflated mass balance could have been due to many factors, including poor calibration or instrument set-up, however despite this, the results are still comparable as all of the factors would have been the same for each data point, and as such trends can still be identified and discussed.

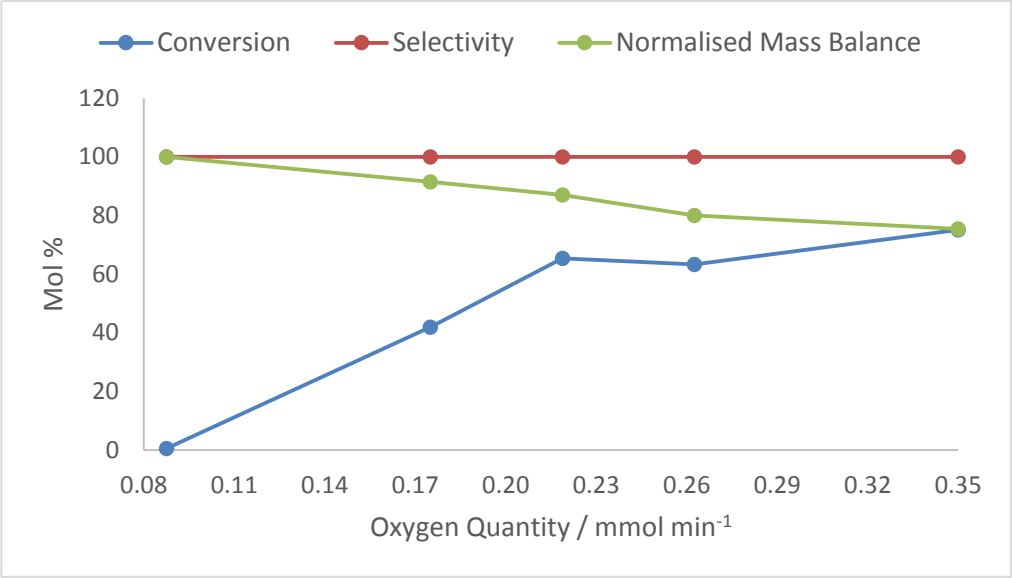

Figure 3.28: Plot showing the change in conversion, selectivity and normalised mass balance as the oxygen quantity is varied in the oxidation of KA-oil using 7 wt. % Pt/CuClP reduced at 200 °C; 1:1 ratio KA-oil feedstock, 0.20 g catalyst, 15 µL min^{-1} substrate flow rate, 10 – 40 mL min^{-1} air flow rate, 200 ° C, 1 hr on stream.

The weight hourly space velocity (WHSV) is a term used to relate the flow of a substrate to the residence time over a fixed catalyst bed, and can be calculated using Equation 3.2. Altering the substrate flow rate of a system allows the WHSV to be varied, and as such, the effect of increased residence time on the oxidation of KA-oil could be investigated. The substrate flow was varied between 5 – 25 µL min^{-1}, and the results are shown in Figure 3.29.

$$WHSV\ (hr^{-1}) = \frac{Substrate\ flow\ (g\ hr^{-1})}{Mass\ catalyst\ (g)}$$

Equation 3.2: Equation for calculating the weight hourly space velocity (hr^{-1}).

Naturally, the conversion was expected to increase with a decrease in WHSV due to the longer residence time with the catalyst, and this was indeed observed. From the linear relationship of conversion to WHSV it is clear that the rate determining step is dependent on the amount of cyclohexanol and oxygen there is in the system, as you would expect. It is also worth noting that the mass balance decreased with decreasing WHSV, and this is most likely due to the increased residence times increasing the likelihood of over-oxidising cyclohexanol to products that could not be detected by GC. Increasing the WHSV limits the time products spend in contact with the catalyst

and they are therefore less likely to over-oxidise past the formation of cyclohexanone. As a result of the above, a compromise must be made between obtaining maximum conversion whilst having an acceptable mass balance. As such, A WHSV of 1.83 hr^{-1}, with a corresponding substrate flow rate of 15 µL min^{-1}, was determined to be optimum.

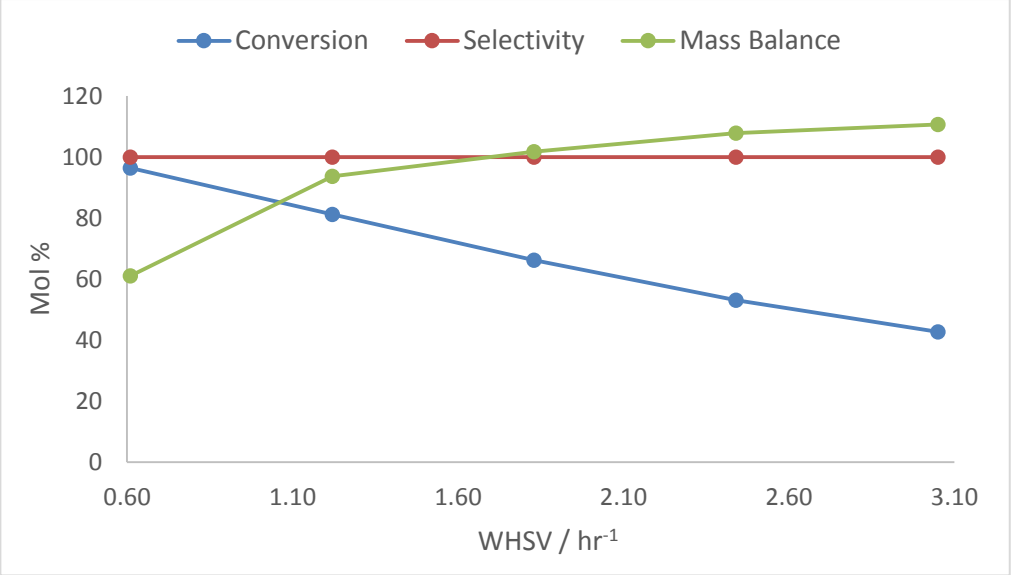

Figure 3.29: Plot showing the change in conversion, selectivity and mass balance as the weight hourly space velocity is varied in the oxidation of KA-oil using 7 wt. % Pt/CuClP reduced at 200 °C, 1:1 ratio KA-oil feedstock, 0.20 g catalyst, 5 – 25 µL min^{-1} substrate flow rate, 25 mL min^{-1} air flow rate, 200 ° C, 1 hr on stream.

The outcome of the above studies allowed the optimum operating conditions for the 7 wt. % Pt/CuClP catalyst reduced at 200 °C to be determined, with a temperature of 200 °C, a substrate flow rate of 15 µL min^{-1} and an air flow rate of 25 mL min^{-1}. These conditions were used as a basis for screening the bimetallic CuClP catalysts and have been used for the remainder of the catalytic testing in this work.

Bimetallic Copper Chlorophosphates

An activation temperature study was conducted on the bimetallic CuClP materials to investigate the effect of reduction temperature on the catalytic activity of the materials. The catalytic results are tabulated and displayed in Table 3.4 and Figure 3.30 below. All reaction parameters are tabulated in Figure A. 18 in the appendix.

Table 3.4: Screening of the bimetallic CuClP materials reduced at different temperatures for the oxidation of KA-oil; 1:1 ratio KA-oil feedstock, 0.20 g catalyst (7 wt. %), 15 µL min^{-1} substrate flow rate, 25 mL min^{-1} air flow rate, 200 ° C, 1 hr on stream.

Catalyst	Activation Temperature / °C	Conversion / mol %	Cyclohexanone Selectivity / %	TOF / hr^{-1}
AuPt/CuClP	150	0	0	0
	200	48	> 99	30
	250	58	> 99	34
	300	89	> 99	53
	350	61	> 99	32
PtPd/CuClP	150	11	> 99	6
	200	63	> 99	31
AuPd/CuClP	150	0	0	0
	200	0	0	0

Similarly to the monometallic CuClP materials, it appears that only the Pt-containing bimetallic CuClP materials are active in the oxidation of KA-oil. This trend was expected as the individual metal loadings are similar to the monometallic CuClP materials (see Figure A. 9). As such, it is possible that the loadings of Au and Pd may be too low to give rise to conversion without the assistance of Pt, and as such, the AuPd/CuClP material is the least active of the bimetallic catalysts. Of the Pt-containing materials, the AuPt/CuClP materials are the most promising catalysts, achieving the highest conversions and being stable over the largest range of reduction temperatures. This increased activity could be a result of the AuPt/CuClP material having the smallest, most uniform nanoparticles, and containing predominantly Au^0 and Pt^0, as seen in the XPS data. In contrast, the AuPd/CuClP and PtPd/CuClP materials both contained a mixture of oxidation states in all of the samples which may have impacted their activities.

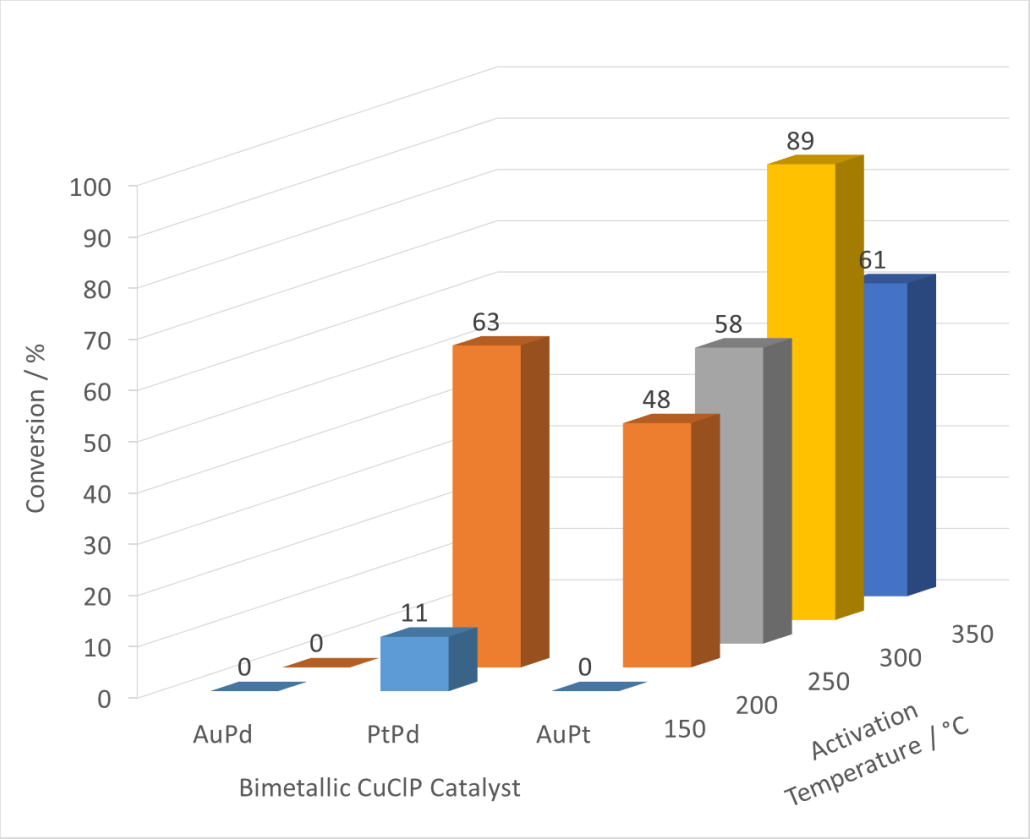

Figure 3.30: Screening the bimetallic CuClP materials for the oxidation of KA-oil; catalysts reduced at a variety of activation temperatures; 1:1 ratio KA-oil feedstock, 0.20 g catalyst (7 wt. %), 15 µL min^{-1} substrate flow rate, 25 mL min^{-1} air flow rate, 200 ° C, 1 hr on stream.

Despite the high activity of the AuPt/CuClP material, no conversion was observed for the sample reduced at 150 °C. This is possibly due to Pt and Au requiring temperatures higher than 200 °C and 250 °C respectively to fully extrude. As such, it is possible that there were no active metallic nanoparticles present in the material for the reaction. As there is no XPS data available for the AuPt/CuClP sample reduced at 150 °C predictions can be made based on the monometallic Au/CuClP and Pt/CuClP data, where the samples reduced at 150 °C consisted mainly of Au^0 and Pt^{II} respectively. From the inactivity of the Au/CuClP material in the oxidation of KA-oil, it is most likely that the Pt will be contributing more to the activity of the catalyst, and so despite the likely presence of Au^0 in the sample (from the monometallic Au XPS data), the sample is likely to consist of predominantly Pt^{II}. As such, it is unlikely that there will be any Pt^0 to act in the reaction. For the AuPt/CuClP samples reduced above 200 °C, there is a clear trend of increasing activity with reduction temperature, until the sample reduced at 350 °C, where the conversion drops off. This drop in conversion is possibly due to sintering of nanoparticles as suggested by TEM, or even the emergence of the Au-Cu alloys seen in the monometallic STEM-EDX and EXAFS. There is a large

increase in activity between the AuPt/CuClP samples reduced at 150 °C and 200 °C, with the XPS data showing predominantly Au^0 and Pt^0 in the sample reduced at 200 °C. This large increase in activity is likely due to the ability of Pt and Au to extrude at 200 °C. The conversion continues to increase until the sample reduced at 300 °C, and this is thought to be due to increased extrusion. Despite the XPS data showing predominantly Au^0 and Pt^0 across all samples, the technique is mostly surface sensitive (penetration depth of ca. 10 nm[131]) and so cannot observe the chloride precursor within the channels of the materials. As such, if a considerable amount of precursor remains in the channels of the material, on activating at higher temperatures there may be an increase in the extent of extrusion allowing more nanoparticles to be deposited on the surface of the catalyst. This would cause an increase in conversion while the XPS data would remain unchanged. The highest activity for the AuPt/CuClP material was achieved for the sample reduced at 300 °C, and it is most likely that this temperature reached a comprise between a high temperature required for maximum extrusion whilst keeping the temperature low enough to prevent nanoparticle sintering. It is also possible that this sample was the most active due to the high nanoparticle density feature present in the TEM images. The drop in catalytic activity for the AuPt/CuClP material reduced at 350 °C could be due to possible nanoparticle sintering causing the larger particles seen in the TEM data (see Figure 3.16h). It is expected that these larger particles would be less catalytically active than smaller particles due to their smaller surface area, so may explain the decrease in conversion despite the higher degree of nanoparticle extrusion expected at the higher activation temperature. It is worth noting that the reaction was also carried out using an as-synthesised sample of the AuPt/CuClP material which showed no catalytic activity (see Figure A. 18 in the appendix). As such, all catalytic activity of the AuPt/CuClP material can be attributed to the Au and Pt nanoparticles.

The activities of the PtPd/CuClP materials also increase with activation temperature, with the maximum conversion being achieved for the sample reduced at 200 °C. The large increase in conversion between the samples reduced at 150 °C and 200 °C is most likely due to the transition from a mixture of Pt oxidation states (Pt^{II}, Pt^{IV} and Pt^0) to predominantly Pt^0 from the XPS data. A mixture of Pd oxidation states (Pd^{II} and Pd^0) remains in both samples, however it is unlikely that Pd plays a large role in the activity of the catalysts, as Pd/CuClP was inactive in the reaction. The conversions achieved by the PtPd/CuClP and Pt/CuClP samples reduced at 200 °C are comparable, with the PtPd/CuClP material being slightly more active (63 mol % c.f. 59 mol % conversion). Comparing the turnover frequencies of each catalyst is a useful way of normalising the catalytic data for the metal active site, however the turnover frequency reported for the PtPd/CuClP material is likely to be inaccurate as it was calculated assuming 50 % contribution from each metal to the catalytic activity. Assuming that Pd plays no role in the catalysis, a perhaps more representative turnover frequency of 71 hr^{-1} could be reported (as opposed to 31 hr^{-1}), which is much closer to the

turnover frequency of 63 hr^{-1} reported for the monometallic Pt/CuClP sample. This slight increase in turnover frequency for the bimetallic sample could be indicative of a small contribution to the activity from Pd, however this is difficult to quantify. It is worth noting that the PtPd/CuClP material is the most active of all of the catalysts activated at 200 °C. However, as this material is limited by thermal stability, the AuPt/CuClP is still the best system as a higher activation temperature can be used, achieving a higher conversion (89 mol % (AuPt/CuClP reduced at 300 °C) c.f. 63 mol % (PtPd/CuClP reduced at 200 °C)).

Unlike the conversions obtained for the Pt/CuClP and PtPd/CuClP materials, the conversions achieved by the AuPt/CuClP and Pt/CuClPs are not comparable. The conversion achieved by the monometallic Pt/CuClP material was approximately 10 mol % higher than the AuPt/CuClP material when reduced at both 200 °C and 250 °C (59 mol % (Pt/CuClP reduced at 200 °C) c.f. 48 mol % (AuPt/CuClP reduced at 200 °C), and 69 mol % (Pt/CuClP reduced at 250 °C) c.f. 58 mol % (AuPt/CuClP reduced at 250 °C) respectively). As the metal loadings were similar, this difference was likely caused by the presence of Au. As the nature of the nanoparticles is unknown, it is possible that this decrease in activity could be due to Au blocking Pt sites (if the particles are discrete sites), or due to the alloying of Au and Pt to produce nanoparticles that are less effective in the oxidation reaction. However, despite reducing the activity of the Pt nanoparticles, the presence of Au seems to allow the material to be activated at much higher temperatures, and this access to higher activation temperatures ultimately allows the AuPt/CuClP catalyst to achieve more impressive conversions compared to the monometallic Pt/CuClP catalyst (89 mol % (AuPt/CuClP reduced at 300 °C) c.f. 69 mol % (Pt/CuClP reduced at 250 °C)).

As the nature of the interaction between Au and Pt in the AuPt/CuClP material is unknown, a physical mixture study was conducted in order to probe the nature of the Au and Pt nanoparticles. It would have been most beneficial to probe the AuPt/CuClP catalyst reduced at 300 °C, however unfortunately as the monometallic Pt/CuClP catalyst was found to break down at 300 °C, the system reduced at 250 °C was explored instead. In the study, the AuPt/CuClP sample reduced at 250 °C was compared to two mixed samples: one where an as-synthesised Au/CuClP sample and an as-synthesised Pt/CuClP sample were mixed together and then reduced, and one where a reduced Au/CuClP sample and a reduced Pt/CuClP sample were mixed together. The results can be seen in Table 3.5 and Figure 3.31. All reaction parameters are tabulated in Figure A. 19 in the appendix, and can be compared directly with analogous Au/CuClP and Pt/CuClP data.

Table 3.5: Physical mixture test for the Au/CuClP, Pt/CuClP and AuPt/CuClP catalysts in the aerobic oxidation of KA-oil. †Mix then R250 refers to mixing the as-synthesised Au/CuClP and Pt/CuClP materials before reducing them at 250 °C together; ‡R250 then mix refers to mixing the Au/CuClP material reduced at 250 °C with the Pt/CuClP material reduced at 250 °C; 1:1 ratio KA-oil feedstock, 0.20 g catalyst (3.5 wt. % each metal), 15 µL min^{-1} substrate flow rate, 25 mL min^{-1} air flow rate, 200 ° C, 1 hr on stream.

Catalyst	Activation Temperature / °C	Conversion / mol %	Cyclohexanone Selectivity / %	TOF / hr^{-1}
AuPt/CuClP	250	58	> 99	34
Au/CuClP + Pt/CuClP	Mix then R250†	65	> 99	41
Au/CuClP + Pt/CuClP	R250 then mix‡	61	> 99	38

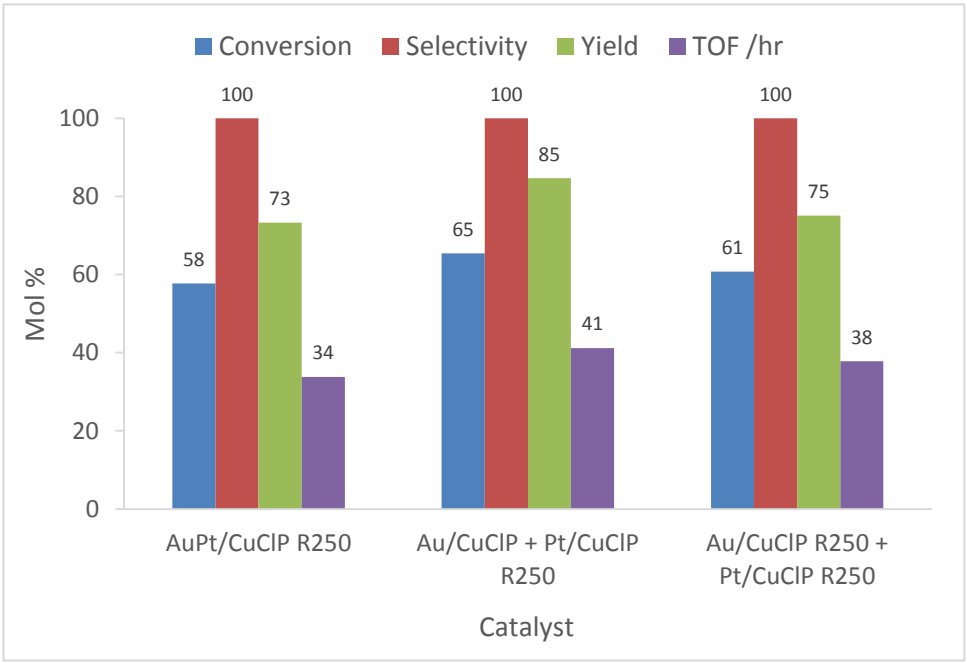

Figure 3.31: Physical mixture test for the Au/CuClP, Pt/CuClP and AuPt/CuClP catalysts in the aerobic oxidation of KA-oil; 1:1 ratio KA-oil feedstock, 0.20 g catalyst (3.5 wt. % each metal), 15 µL min^{-1} substrate flow rate, 25 mL min^{-1} air flow rate, 200 ° C, 1 hr on stream.

During the extrusion and reduction process, it is possible that the Au and Pt could form alloyed nanoparticles, form discrete sites, or form individual nanoparticles in close proximity, which could act synergistically. It was thought that by comparing mixed samples with the bimetallic AuPt/CuClP catalyst it would be possible to determine whether the sample comprised of a physical mixture of Au and Pt nanoparticles (if the results are similar to the mixed samples), or whether bimetallic species are likely to be present (if the results are very different). Given the similarity of the AuPt/CuClP data to the physical mixture result, it is more likely that the Au and Pt nanoparticles formed as discrete sites in the sample. However, as the presence of each metal appears to affect the extrusion of the other (through XPS data), it is possible that these discrete sites are in close proximity to one another, and therefore a synergy could exist between them. However, it is worth noting that the uncontrolled nature of this nanoparticle formation is likely to give rise to a mixture of different sites, and as such, it is possible that all three nanoparticle possibilities are present. It is interesting that the AuPt/CuClP material is stable when reduced at 300 °C when the monometallic Pt/CuClP material begins to break down. This increase in stability could indicate that the Au and Pt nanoparticles begin to alloy when activated at this temperature, and this change could be reflected in the marked increase in catalytic activity for the AuPt/CuClP catalyst reduced between 250 °C and 300 °C (see Figure 3.30). It would be interesting to repeat this study using catalysts reduced at 300 °C to see if dramatically different results are achieved, despite the degradation of the monometallic Pt/CuClP catalyst.

Comparing Catalytic Systems

Work was done to compare the activity of metal nanoparticles supported on different materials in the oxidation of KA-oil, looking specifically at TiO_2 and the CuClP framework. The TiO_2-supported catalysts were provided by S. Rogers from the UK Catalysis Hub at the Research Complex at Harwell, and were tested in the same way as the CuClP materials. The results are tabulated in Table 3.6 below, and all reaction parameters can be found in Figure A. 20 in the appendix.

For the TiO_2-supported catalysts, it was found that the monometallic Pd material was the most active but unselective catalyst, producing substantial quantities of cyclohexene and benzene by-products in the reaction, most likely formed in the dehydration of cyclohexanol[130] and dehydrogenation of cyclohexene[132] respectively. The monometallic Au catalyst was found to be the most selective of the TiO_2-supported catalysts, only producing small amounts of cyclohexene; however, the Au catalysts generally suffered very low conversions. The Pt-containing TiO_2-supported catalysts typically performed moderately in comparison to the Au and Pd-containing catalysts, being significantly more selective than Pd/TiO_2, and approximately twice as active as Au/TiO_2. The TiO_2-supported catalysts used in this study were prepared by colloidal

deposition at 1 ° C and 75 °C as it had been found that forming nanoparticles in this manner at low temperatures could inhibit their growth, allowing a smaller size distribution to be achieved. It was generally found that the catalysts prepared at 1 °C were more active than those prepared at 75 °C; however the effect on the selectivity was less straightforward. In the case of Pd/TiO_2, on an increase in synthesis temperature the selectivities for the by-products were altered slightly, with an increase in the selectivity for cyclohexene met with a corresponding decrease in selectivity for benzene. However, in the case of Au/TiO_2, the effect of increased synthesis temperature actually encourages the reaction to be less selective for the desired product cyclohexanone in favour of cyclohexene.

Table 3.6: Screening of the TiO_2-supported nanoparticle catalysts in the aerobic oxidation of KA-oil; catalysts contain 1 wt. % metal, with bimetallic catalysts containing 0.05 wt. % of each metal; catalysts provided by S. Rogers from the UK Catalysis Hub at the Research Complex at Harwell, Oxford; 1:1 ratio KA-oil feedstock, 0.20 g catalyst, 15 µL min^{-1} substrate flow rate, 25 mL min^{-1} air flow rate, 200 ° C, 1 hr on stream.

Catalyst	**Conversion / mol %**	**Selectivity / %**			**TOF / hr^{-1}**
		Cyclohexanone	**Cyclohexene**	**Benzene**	
Pd/TiO_2 (1 °C)	57	80	5	15	109
Pd/TiO_2 (75 °C)	36	80	7	13	69
Pt/TiO_2 (1 °C)	19	95	5	0	66
$AuPt/TiO_2$ (1 °C)	8	94	6	0	30
$AuPd/TiO_2$ (1 °C)	6	95	5	0	17
Au/TiO_2 (1 °C)	4	97	3	0	14
Au/TiO_2 (75 °C)	4	96	4	0	16

Unlike the TiO_2-supported catalysts, no by-products were observed in the GC trace for the CuClP catalysts, alluding to improved selectivity. These selectivity trends prove a useful tool for highlighting the differences in the active sites for both catalytic systems, with the absence of cyclohexene alluding to a lack of strong acid sites in the CuClP materials. In contrast, the increased selectivity of the TiO_2 catalysts for cyclohexene suggests that acid sites may play an important part in the activity of these catalysts. For ease of comparison, the best CuClP catalyst results have been tabulated in Table 3.7. For clarity, all of the reaction parameters for the CuClP catalysts can be found in Figure A. 21 in the appendix.

Table 3.7: Compilation of the best performing CuClP catalysts in the aerobic oxidation of KA-oil; 1:1 ratio KA-oil feedstock, 0.20 g catalyst (3.5 wt. % each metal), 15 µL min^{-1} substrate flow rate, 25 mL min^{-1} air flow rate, 200 ° C, 1 hr on stream.

Catalyst	**Conversion / mol %**	**Cyclohexanone Selectivity / %**	**TOF / hr^{-1}**
AuPt/CuClP R300	89	> 99	53
Pt/CuClP R250	69	> 99	82
PtPd/CuClP R200	63	> 99	31
Au/CuClP R300	0	0	0
Pd/CuClP R200	0	0	0
AuPd/CuClP R200	0	0	0

In comparison to the TiO_2-supported catalysts, only the Pt-containing CuClP materials were catalytically active, with the Pd-containing CuClP catalysts performing the worst (only active in the presence of Pt). This reversal of catalytic activity of the metal centres could suggest a potential influence from the support, perhaps especially on the activity of the Pd nanoparticles; however,

without detailed structural characterisation it would be impossible to determine the exact influence of the support. It is worth noting that conversions between the catalytic systems cannot be directly compared due to the different metal loadings, and should rather be used to display trends in catalytic activity. Instead, it is better to compare the turnover frequencies for the catalysts as they have been normalised to the metal loading. However, note that the turnover frequency reported for the AuPt/CuClP material reduced at 300 °C is unlikely to be accurate as the nature of the active site in unknown. As evidence suggests that the Au/CuClP material reduced at 300 °C is inactive, it can be assumed that the Au does not contribute to the catalytic activity, and as such the turnover frequency can be calculated only considering Pt, and can now be reported as 108 hr^{-1} (c.f. 53 hr^{-1}). The nature of the active sites for the PtPd/CuClP and bimetallic TiO_2-supported catalysts is also unknown, however unlike the AuPt/CuClP material there is no specific evidence for the inactivity of either metal, and so both metals were considered when calculating the turnover frequencies. A comparison of the turnover frequencies for the active catalysts can be seen in Figure 3.32 below, where only active catalysts and TiO_2-supported catalysts synthesised at 1 °C have been included. Generally, the turnover frequencies were very comparable between the two catalyst systems, with Pd/TiO_2 (1 °C) and AuPt/CuClP (R300) achieving very similar values. The similarity in turnover frequencies suggest that both catalysts are perform equally well in the conversion of KA-oil, however the improved selectivity of the AuPt/CuClP catalyst allows it to be the better catalyst.

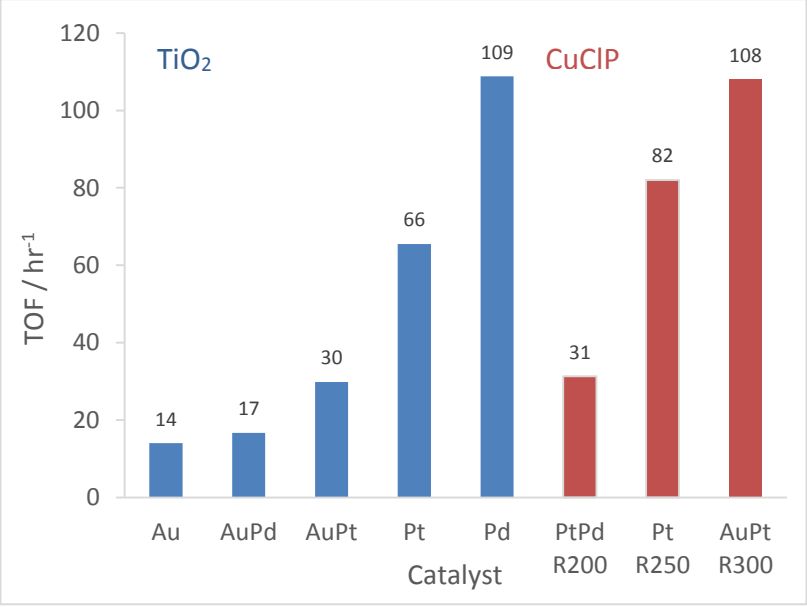

Figure 3.32: Comparison of the turnover frequencies (TOFs) for the TiO_2-supported catalysts (blue) and the CuClP catalysts (red) for the aerobic oxidation of KA-oil; 1:1 ratio KA-oil feedstock, 0.20 g catalyst, 15 µL min^{-1} substrate flow rate, 25 mL min^{-1} air flow rate, 200 ° C, 1 hr on stream.

3.2.2 Oxidation of Valerolactam

In order to probe the activity of the CuClP materials further, the oxidation of valerolactam (see Figure 3.33) was explored with the intention of using the results as a basis for the oxidation of caprolactam, a relevant feedstock in the Nylon industry. There is very limited research on the oxidation of caprolactam or valerolactam to adipimide and glutarimide respectively; however, examples of general lactam oxidation to cyclic imides demonstrate the harsh reagents and conditions required to achieve the transformation. These include the use of ozone in tetrachloromethane[133], molecular oxygen under high temperature and pressure in subcritical water[134], peracetic acid under microwave irradiation[135], and hydroperoxides and peracids with metal ion catalysts[136–139].

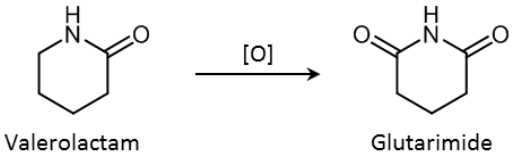

Figure 3.33: Oxidation of valerolactam to glutarimide.

The oxidation of valerolactam was attempted using the oxidant *tert*-butyl hydroperoxide, with batch processes conducted on a small scale. A selection of monometallic and bimetallic CuClP catalysts were screened in preliminary testing, and the results along with the blank reaction are tabulated in Table 3.8 below, with key results shown in Figure 3.34. Note that these results were produced from rough preliminary testing, and as such only conversions were calculated. All reaction parameters can be found in Figure A. 22 in the appendix.

Table 3.8: Screening the CuClP catalysts in the oxidation of valerolactam; experiments conducted by T. Nimmo; 0.06 g valerolactam, 0.02 g catalyst (7 wt. %), 0.02 g chlorobenzene, 5 mL *tert*-butanol, 0.24 mL *tert*-butyl hydroperoxide (6.0 M in decane), 80 °C reflux, 24 hr.

Catalyst	Activation Temperature / °C	Conversion / mol %
-	N/A	2
Au/CuClP	150	17
	250	22
	350	60

Catalyst (continued)	**Activation Temperature / °C** (continued)	**Conversion / mol %** (continued)
Pt/CuClP	150	31
	175	31
	250	33
Pd/CuClP	150	23
	175	39
AuPt/CuClP	200	45
AuPd/CuClP	200	44
PtPd/CuClP	200	41

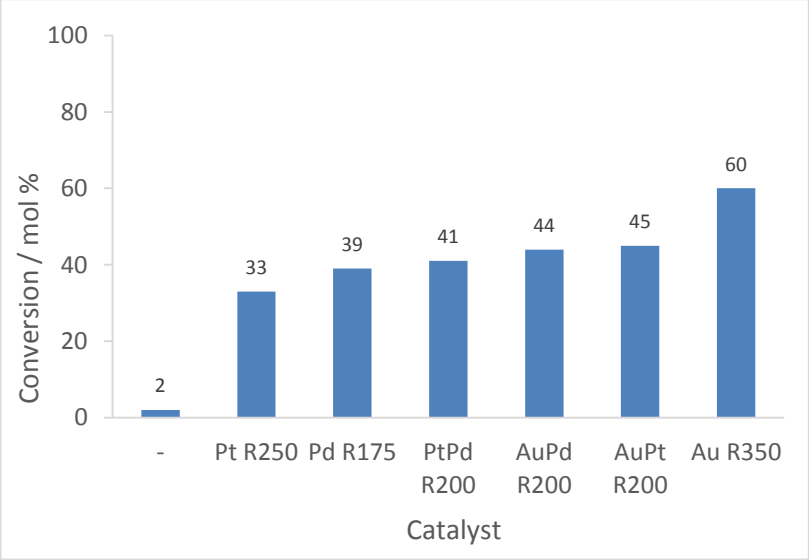

Figure 3.34: Key findings for the screening of the CuClP catalysts in the oxidation of valerolactam; experiments conducted by T. Nimmo; 0.06 g valerolactam, 0.02 g catalyst, 0.02 g chlorobenzene, 5 mL *tert*-butanol, 0.24 mL *tert*-butyl hydroperoxide (6.0 M in decane), 80 °C reflux, 24 hr.

From the graph, it is clear that the Au/CuClP material reduced at 350 °C was the most active catalyst in the oxidation of valerolactam, with all Au-containing catalysts outperforming the other metals. When comparing the Au/CuClP catalyst reduced at different temperatures there is a marked increase in activity between the catalysts reduced at 250 °C to 350 °C (see Figure 3.35). It has been

hypothesised that this increase in activity is caused by the increase in the extent of Au-Cu alloying evidenced in the monometallic Au/CuClP catalyst when reduced from 250 °C to 350 °C (increase in Au-Cu coordination number from 0.6 to 4.1).

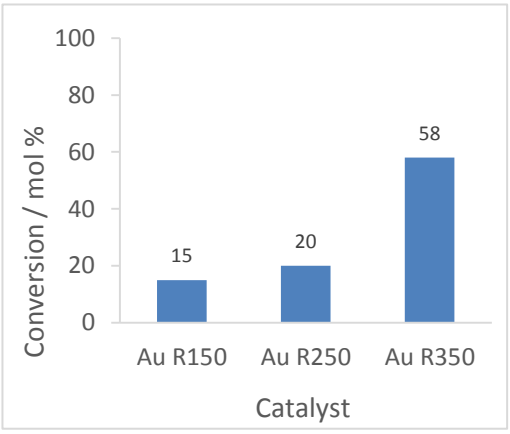

Figure 3.35: Screening the Au/CuClP catalysts reduced at different reduction temperature in the oxidation of valerolactam; experiments conducted by T. Nimmo; 0.06 g valerolactam, 0.02 g catalyst (7 wt. %), 0.02 g chlorobenzene, 5 mL *tert*-butanol, 0.24 mL *tert*-butyl hydroperoxide (6.0 M in decane), 80 °C reflux, 24 hr.

3.2.3 Probing the Acidity of the Copper Chlorophosphates

As part of a collaboration with Aston University, the monometallic Pt/CuClP material was screened in the hydrogenation of furfural to furfuryl alcohol (see Figure 3.36). The simplified hydrogenation mechanism can be seen in Figure 3.37.

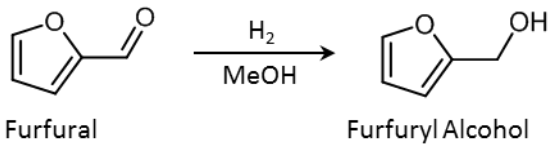

Figure 3.36: Hydrogenation of furfural to furfuryl alcohol.

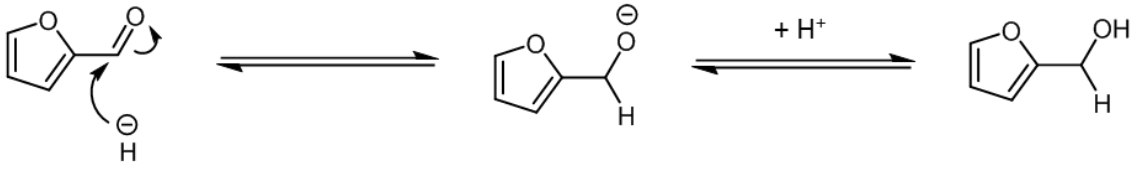

Figure 3.37: Simplified mechanism for the hydrogenation of furfural to furfuryl alcohol.

It was noticed that a small amount of furfuryl alcohol was formed in the reaction, however the main product was 2-(dimethoxymethyl)furan (see Figure 3.38), a typically acid-catalysed product (see Figure 3.38 for the proposed mechanism for the formation of the acetal product from furfural). This unexpected outcome suggested that the Pt/CuClP material was acidic in nature, conflicting with the idea that the CuClP materials did not contain strong acid sites, as proven by the lack of cyclohexene in the oxidation of KA-oil. As such, the acidity of the Pt/CuClP material was to be probed in more detail by screening in the Brønsted acid-catalysed Beckmann rearrangement of cyclohexanone oxime.

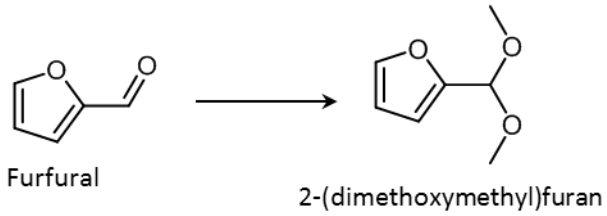

Figure 3.38: Reaction of furfural to 2-(dimethoxymethyl)furan.

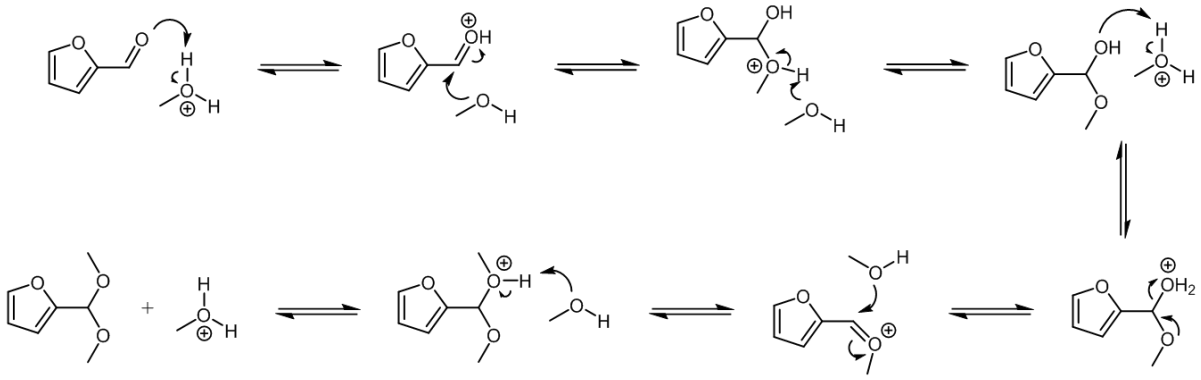

Figure 3.39: Proposed mechanism for the acid-catalysed formation of 2-(dimethoxymethyl)furan from furfural.

The Pt/CuClP catalyst reduced at 200 °C was screened in the Beckmann rearrangement, with preliminary experiments being conducted by S. Newland. The Beckmann rearrangement of cyclohexanone oxime requires a Brønsted acid in order to form caprolactam (see Figure 3.40), and the mechanism is shown in Figure 3.41 below.

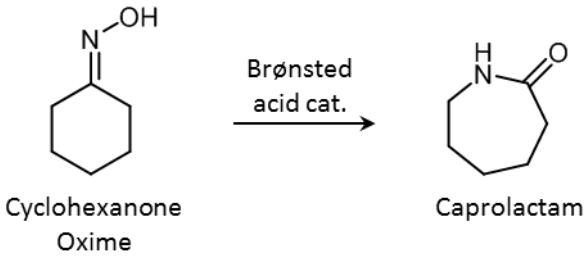

Figure 3.40: Brønsted acid-catalysed Beckmann rearrangement of cyclohexanone oxime to caprolactam.

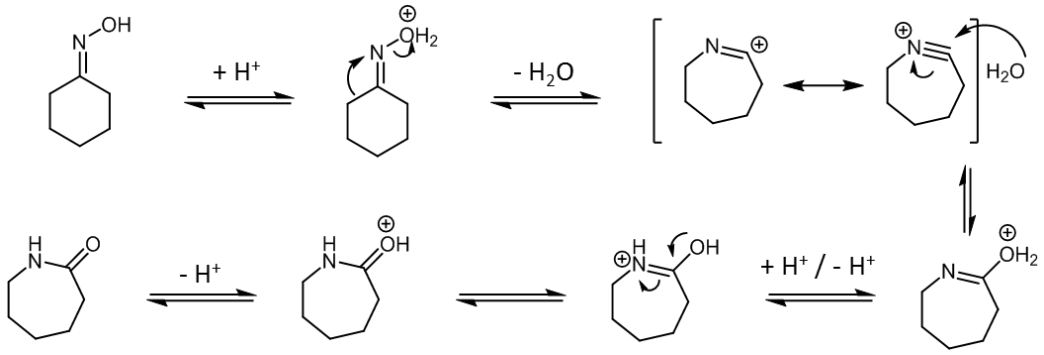

Figure 3.41: Brønsted acid-catalysed mechanism for the Beckmann rearrangement of cyclohexanone oxime to caprolactam.

From this preliminary test, it was found that the Pt/CuClP catalyst did not form any caprolactam in the reaction, observing cyclohexanone instead in > 99 % selectivity. This lack of lactam formation indicated that the Pt/CuClP catalyst did not contain the necessary Brønsted acid sites required for the reaction, but instead contained primarily weak Lewis acid sites, which have been found to be responsible for cyclohexanone formation[140]. These results contrast those seen by Newland *et al.*[141] where hierarchically porous silicon AlPO-5 (HP SAPO-5), a catalyst containing Brønsted acid sites, directly converted cyclohexanone oxime to caprolactam in 76 % selectivity, with no evidence of any cyclohexanone formation (catalyst achieved 100 mol % conversion). The proposed mechanism for the conversion of cyclohexanone oxime to cyclohexanone can be seen in Figure 3.42 below.

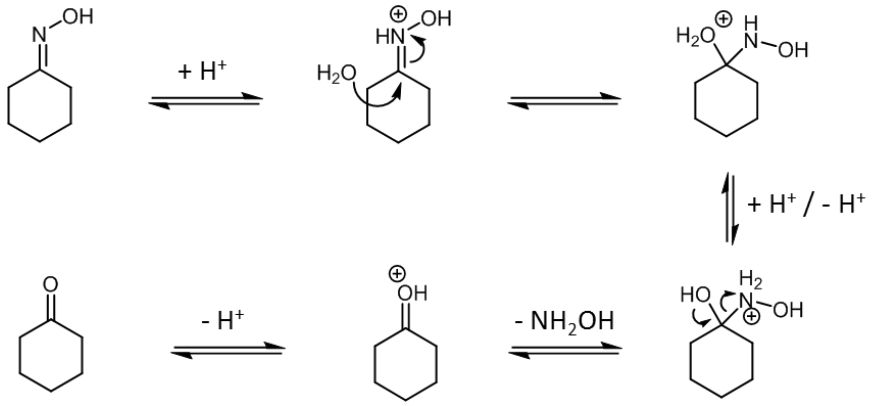

Figure 3.42: Proposed mechanism for the Lewis acid-catalysed conversion of cyclohexanone oxime to cyclohexanone.

In order to understand whether the Lewis acid sites originated from the Pt nanoparticles or the CuClP framework the as-synthesised and reduced parent framework was also tested in the liquid phase Beckmann rearrangement of cyclohexanone oxime. The results are tabulated in Table 3.9 alongside the prior data for Pt/CuClP reduced at 200 °C collected by S. Newland. All reaction parameters and conditions can be found in Figure A. 23 in the appendix. Conversion and selectivity plots can be found in Figure A. 13, Figure A. 14 and Figure A. 15 in the appendix.

Table 3.9: Screening the CuClP catalysts for the liquid phase Beckmann rearrangement of cyclohexanone oxime; values taken after 6 hour reaction; † reaction conducted by S. Newland; 0.1 g cyclohexanone oxime, 0.1 g catalyst (7 wt. % Pt), 0.1 g chlorobenzene, 20 mL acetonitrile, N_2 atmosphere reflux, 130 °C.

Catalyst	Activation Temperature / °C	Conversion / mol %	Caprolactam Selectivity / %	Cyclohexanone Selectivity / %
CuClP	-	94	0	> 99
	200	95	0	> 99
Pt/CuClP†	200	92	0	> 99

As the conversions achieved by the parent framework and the Pt/CuClP catalysts are comparable it is unlikely that the Pt nanoparticles are contributing to the formation of cyclohexanone. As such, this indicates that the parent framework itself possesses Lewis acid sites.

The Lewis acidic nature of the CuClP material was probed in some preliminary reactions that specifically require Lewis acid sites to commence. One such reaction is the Baeyer-Villiger oxidation of cyclohexanone to produce cyclohexyl lactone (see Figure 3.43). The simplified proposed mechanism can be seen in Figure 3.44 below.

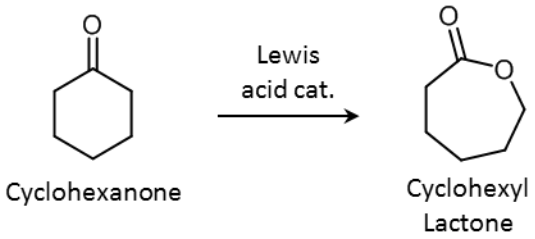

Figure 3.43: Lewis acid-catalysed Baeyer-Villiger oxidation of cyclohexanone to cyclohexyl lactone.

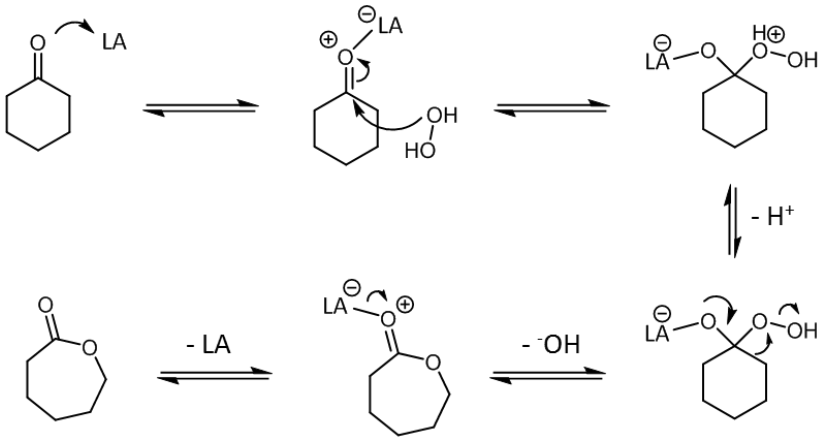

Figure 3.44: Simplified proposed mechanism for the Lewis acid (LA) catalysed Baeyer-Villiger oxidation of cyclohexanone to cyclohexyl lactone.

Corma *et al*.[142] focused on using a Lewis acidic catalyst to selectively activate the carbonyl group in a range of ketone starting materials, allowing reaction with non-activated hydrogen peroxide to selectively produce the lactone product. As such, the conditions were adopted and the CuClP material reduced at 200 °C was tested in the reaction. The reaction parameters and conditions can be found in Figure A. 24 in the appendix. Unfortunately no reaction occurred, however as the catalyst used by Corma *et al*. was a strong Lewis acid, it is likely that the reaction would not occur for the CuClP material as the Beckmann rearrangement results implied the presence of weak Lewis acid sites. More forcing conditions could be employed in order to observe any reaction, or another suitable Lewis acid probe reaction could be investigated.

Chapter 4: Conclusions and Future Work

4.1 Conclusions

The synthesis of the bimetallic CuClP materials was largely successful, producing AuPt/CuClP, PtPd/CuClP and AuPd/CuClP variants. The AuPt/CuClP material was found to be stable until 350 °C, a vast improvement on the monometallic Au/CuClP (< 300 °C) and Pt/CuClP (< 250 °C) materials. This increase in stability is theorised to be a result of a stabilising interaction between the two metals, although this has not been proven. Similarly to the monometallic Pd/CuClP material, the PtPd/CuClP and the AuPd/CuClP materials were both only stable until 225 °C, and as such are thought to be somewhat limited by their low temperature stability. TEM images showed the presence of small and uniform nanoparticles across the majority of the bimetallic samples, with the exception of the AuPt/CuClP sample reduced at 350 °C, where it is likely that sintering may have occurred to form larger species. The AuPt/CuClP samples appeared to exhibit the smallest nanoparticles, followed by PtPd/CuClP and AuPd/CuClP where the presence of larger particles was thought to be due to the propensity of Pd to form larger nanoparticles, as evidenced in the monometallic materials (see Figure 1.5). XPS data revealed that Au^0 was present in samples of the AuPt/CuClP material reduced between 200 – 350 °C, which was largely unexpected based on the XPS data for the monometallic Au/CuClP where temperatures higher than 250 °C were required to form Au nanoparticles (see Figure 1.11a). Similarly, all of the samples contained Pt^0, despite the monometallic Pt/CuClP showing a mixture of Pt oxidation states (see Figure 1.10a). These discrepancies once again allude to a synergistic interaction between the Au and the Pt, whereby the presence of each metal encourages the other to form nanoparticles at lower temperatures than observed in the monometallic materials. In the PtPd/CuClP and AuPd/CuClP materials, there was a progression from Pd^{II} towards Pd^0 with reduction temperature; however, a mixture of Pd oxidation states remained in all of the samples reduced between 150 – 200 °C, in agreement with monometallic Pd/CuClP XPS data (see Figure 1.12a). As such, it is likely that Pd-containing CuClP materials required higher temperatures to form Pd nanoparticles, although activating at temperatures higher than 200 °C is not possible due to the limited thermal stability of the Pd-containing materials.

The catalytic potential of the bimetallic CuClP catalysts was explored, with the best catalyst (AuPt/CuClP reduced at 300 °C) achieving 89 mol % conversion with > 99 % selectivity to cyclohexanone in the aerobic oxidation of KA-oil. The process employed utilised molecular oxygen from air in a solvent-free, vapour phase, oxidation reaction conducted at 200 °C. Unlike the traditional industrial process, the oxidation of cyclohexanol in KA-oil did not require the use of

harmful Cr(III) salts or nitric acid, but instead only used the solid catalyst and air in order to progress, and as such the process can be deemed more environmentally benign. In comparison to vapour phase cyclohexanol oxidations found in the literature (see Table 1.4), the AuPt/CuClP catalyst reduced at 300 °C achieved a more impressive result, with the best vapour phase result in the literature achieving a conversion of 90 mol % with only a 50 % selectivity to cyclohexanone when using Mn-MCM-41[96]. The most comparable result in the literature for cyclohexanone selectivity achieved in the vapour phase was using a $Cu/MgO/Cr_2O_3$ catalyst in a dehydrogenation reaction, however despite achieving > 99 % selectivity to cyclohexanone, a low conversion of 38 mol % was achieved[112]. The only system to achieve both comparable conversion and selectivity to the AuPt/CuClP catalyst reduced at 300 °C was using a FeO/MIL-101 catalyst in a microwave reaction, achieving 77 mol % conversion and > 99 % selectivity[105]. Of the bimetallic catalysts found in the literature (see grey highlighted section in Table 1.4), the most comparable results were obtained using the AuPd-SiO_2 catalyst, achieving a conversion of 62 mol % and a selectivity to cyclohexanone of > 99 %[122]. Both reactions included the use of noble metal nanoparticles; however, the AuPt/CuClP catalyst was conducted in the vapour phase making the process much more conducive to being applied to industry, converting off-stream KA-oil to cyclohexanone. As such, the results provided by the AuPt/CuClP catalyst provide an exciting prospect, with the potential for improvement through optimisation of the synthesis procedure and the activation of the material, as well as the catalytic process.

Of the bimetallic CuClP materials, only the Pt-containing materials were found to be active in the oxidation of KA-oil, in agreement with the monometallic CuClP catalytic data. The AuPt/CuClP catalyst performed the best of all three systems, followed by PtPd/CuClP, while the AuPd/CuClP was inactive. The AuPt/CuClP was found to be the most stable catalyst over the largest range of temperatures (150 – 350 °C), whereas the potential of the PtPd/CuClP catalyst was limited by the thermal stability of the material. The catalytic activity of the AuPt/CuClP catalyst was found to increase with reduction temperature until 300 °C, after which point the activity drops, possibly as a result of nanoparticle sintering at 350 °C, as evidenced by the larger particles present in the TEM images collected for this catalyst (see Figure 3.16h). The bimetallic AuPt/CuClP catalyst was also found to have increased activity in the oxidation of KA-oil in comparison to the monometallic Pt/CuClP material, achieving a conversion of 89 mol % in comparison to 69 mol %, highlighting its potential as an oxidation catalyst.

Unfortunately, the nature of the nanoparticle species in the AuPt/CuClP catalyst reduced at 300 °C could not be probed due to the instability of Pt/CuClP above 250 °C; however, the AuPt/CuClP catalyst reduced at 250 °C was determined to contain a mixture of discrete Au and Pt nanoparticles. This was determined by the similarity of catalytic data for AuPt/CuClP to the physical mixture of

Au/CuClP and Pt/CuClP. It is interesting, however, that the presence of Au appears to prevent the AuPt/CuClP material from breaking down above 250 °C, with the AuPt/CuClP material being stable up to 350 °C. This suggests that a synergy exists between the two metals, and as such alludes to the alloying of the two metals to form bimetallic nanoparticles, as opposed to discrete sites as in the catalyst reduced at 250 °C.

The influence of the support on the activity of the nanoparticle catalysts could not be directly determined due to many factors playing a role in nanoparticle activity (size, shape and composition of nanoparticles, etc.), however when comparing the TiO_2-supported catalysts and the CuClP catalysts, the CuClP materials were found to be the most promising. Despite both systems having comparable turnover frequencies, the CuClP materials were more selective to the cyclohexanone product. It was interesting, however, that the order of metal activity changed between the two catalyst systems, with Pd-catalysts performing the best for the TiO_2-supported materials, and the Pt-catalysts performing the best for the CuClP materials.

The catalytic potential of the CuClP materials was explored for the oxidation of valerolactam, with the Au/CuClP giving the best result (60 mol % conversion). A large increase in catalytic activity was seen when this material was activated between 250 – 350 °C, the cause of which is thought to be due to an increase in Au-Cu alloying seen in EXAFS and STEM-EDX.

The acidity of the CuClP materials was explored after the acid-catalysed production of 2-(dimethoxymethyl)furan from furfural was observed. The formation of cyclohexanone from cyclohexanone oxime alluded to the presence of weak Lewis acid sites in the CuClP framework, while the lack of caprolactam formation suggested that no Brønsted acid sites were present. The Lewis acidity was probed in the Baeyer-Villiger oxidation of cyclohexanone, however no caprolactone product was observed, suggesting the lack of strong Lewis acid sites. As such, it was theorised that the CuClP framework contains only weak Lewis acid sites, although more studies and acid characterisation are required in order to confirm this.

4.2 Future Work

From a synthesis standpoint, in order to develop this work, more detailed characterisation is required to understand the nature of the bimetallic nanoparticles and the extrusion process that generates them. Many characterisation techniques can be explored, with the most useful techniques shown in Table 4.1 below.

Table 4.1: Useful information gained from a range of characterisation techniques.

Technique	**Information Gained**
HR-SEM	Morphology of particles across sample and confirm presence of surface features
EDX	Elemental mapping
FTIR	Nature of the surface through the use of probes (e.g. CO, CD_3CN, C_5H_5N)
TPD	Surface coverage of binding sites alluding to site isolation, strength of site through enthalpy of adsorption, and the number of different binding sites on the surface
TPR	Reactivity and redox behaviour, and obtain evidence for interaction between two metallic components
UV-Vis	Oxidation state and coordination geometry of metal particles
XAS	Local structural environment (oxidation state and coordination environment)

HR-SEM = high-resolution scanning electron microscopy, EDX = energy-dispersive X-ray spectroscopy, FTIR = Fourier transform infrared spectroscopy, TPD = temperature programmed desorption spectroscopy, TPR = temperature programmed reduction spectroscopy, UV-Vis = ultraviolet-visible spectroscopy, XAS – X-ray absorption spectroscopy.

The extrusion process is currently being investigated through multiple *in situ* EXAFS studies, which will be supplemented by additional contrast tomography measurements. This will allow a time-resolved 3D distribution to be built up of the extrusion process and resulting nanoparticles, giving valuable insight into the progression of the process. From these EXAFS studies, it is hoped that the Au-Cu alloying alluded to in the Au/CuClP material reduced at 350 °C, through EXAFS, STEM-EDX and catalysis (see Figure 3.35), can be investigated.

Additionally, from the presence of amorphous regions in the TEM images collected for the AuPt/CuClP material (see Figure 3.16d), the synthesis and activation procedures should be further

optimised to ensure maximum efficiency in the formation of the support, and in the generation of the nanoparticles.

From the interesting acid catalysis results (see Section 3.2.3), it is clear that the proposed Lewis acidic nature of the CuClP material needs to be investigated through acid characterisation techniques. A technique that could be used to probe the acidic nature of the surface is diffuse reflectance infrared Fourier transform spectroscopy (DRIFTS) using a variety of different probes (e.g. CO, CD_3CN, C_5H_5N), which would provide information on the nature of the surface through the interaction of the probe with the acid sites. To supplement this, additional acid-catalysed reactions could be explored, specifically focusing on reactions catalysed by Lewis acid sites, such as Friedel-Crafts reactions.

Further development key to understanding the active site of the material would be to undertake post-catalysis characterisation in order to determine whether the active site is altered in any way. This would serve to understand the active site further, whilst also investigating the potential for these catalysis to be reused. In terms of the catalysis, further work could be undertaken in order to optimise the oxidation of KA-oil in order to obtain the maximum results for the AuPt/CuClP catalyst reduced at 300 °C. Time-on-stream studies and recyclability tests are also important steps in determining the viability of the CuClP materials for catalytic oxidations, and should be investigated going forward.

Finally, further developments for this work include a more extensive support influence study, where a larger range of nanoparticle supports are investigated, including SiO_2, CeO_2 and C. This study should be supported with structural characterisation of all of the nanoparticle catalysts in order for meaningful comparisons to be drawn between the different systems, whilst also comparing the catalytic activities of the materials for the aerobic oxidation of KA-oil.

References

[1] P. T. Anastas, T. C. Williamson, Eds. , *Green Chemistry: Frontiers in Benign Chemical Syntheses and Processes*, Oxford University Press, Inc., Oxford, **1998**.

[2] J. M. Thomas, W. J. Thomas, *Principles and Practice of Heterogeneous Catalysis*, Wiley-VCH Verlag GmbH, Weinheim, **2015**.

[3] P. Atkins, T. Overton, J. Rourke, M. Weller, F. Armstrong, *Shriver & Atkins' Inorganic Chemistry*, Oxford University Press, Inc., Oxford, **2010**.

[4] K. M. K. Yu, I. Curcic, J. Gabriel, S. C. E. Tsang, *ChemSusChem* **2008**, *1*, 893–899.

[5] R. I. Masel, *Chemical Kinetics and Catalysis*, John Wiley & Sons Inc., New York, **2001**.

[6] M. Bowker, *The Basis and Applications of Heterogeneous Catalysis*, Oxford University Press, Inc., Oxford, **1998**.

[7] R. J. White, R. Luque, V. L. Budarin, J. H. Clark, D. J. Macquarrie, *Chem. Soc. Rev.* **2009**, *38*, 481–494.

[8] D. Cai, J. M. Mataraza, Z. H. Qin, Z. P. Huang, J. Y. Huang, T. C. Chiles, D. Carnahan, K. Kempa, Z. F. Ren, *Nat. Methods* **2005**, *2*, 449–454.

[9] E. R. Kenawy, S. D. Worley, R. Broughton, *Biomacromolecules* **2007**, *8*, 1359–1384.

[10] X. Hu, S. Dong, *J. Mater. Chem.* **2008**, *18*, 1279.

[11] G. G. Wildgoose, C. E. Banks, R. G. Compton, *Small* **2006**, *2*, 182–193.

[12] D. Astruc, F. Lu, J. R. Aranzaes, *Angew. Chemie - Int. Ed.* **2005**, *44*, 7852–7872.

[13] S. H. Joo, J. Y. Park, C.-K. Tsung, Y. Yamada, P. Yang, G. a Somorjai, *Nat. Mater.* **2009**, *8*, 126–131.

[14] J. Zhu, T. Wang, X. Xu, P. Xiao, J. Li, *Appl. Catal. B Environ.* **2013**, *130-131*, 197–217.

[15] S. Proch, J. Herrmannsdörfer, R. Kempe, C. Kern, A. Jess, L. Seyfarth, J. Senker, *Chem. - A Eur. J.* **2008**, *14*, 8204–8212.

[16] H. Song, R. Rioux, J. D. Hoefelmeyer, R. Komor, K. Niesz, M. Grass, P. Yang, G. A. Somorjai, *J. Am. Chem. Soc.* **2006**, *128*, 3027–3037.

[17] M. Anpo, N. Aikawa, Y. Kubokawa, *J. Phys. Chem.* **1984**, *88*, 3998–4000.

[18] C. Lian, H. Q. Liu, C. Xiao, W. Yang, K. Zhang, Y. Liu, Y. Wang, *Chem. Commun.* **2012**, *48*, 3124–3126.

[19] K. M. Bratlie, H. Lee, K. Komvopoulos, P. Yang, G. A. Somorjai, *Nano Lett.* **2007**, *7*, 3097–3101.

[20] G. Aguilar-Ríos, P. Salas, M. A. Valenzuela, H. Armendáriz, J. A. Wang, J. Salmones, *Catal. Letters* **1999**, *60*, 21–25.

[21] M.-L. Yang, Y.-A. Zhu, C. Fan, Z.-J. Sui, D. Chen, X.-G. Zhou, *Phys. Chem. Chem. Phys.* **2011**, *13*, 3257–3267.

[22] P. Sun, G. Siddiqi, W. C. Vining, M. Chi, A. T. Bell, *J. Catal.* **2011**, *282*, 165–174.

[23] M. A. Aramendía, J. A. Benítez, V. Boráu, C. Jiménez, J. M. Marinas, A. Moreno, *React. Kinet. Catal. Lett.* **1997**, *62*, 23–21.

[24] J. M. Campelo, D. Conesa, J. Gracia, J. Jurado, R. Luque, J. Maria, A. Angel, T. D. Conesa, M. J. Gracia, M. J. Jurado, et al., *Green Chem.* **2008**, *10*, 853–858.

[25] G. J. Hutchings, *Catal. Today* **2008**, *138*, 9–14.

[26] N. Perkas, Z. Zhong, J. Grinblat, A. Gedanken, *Catal. Letters* **2008**, *120*, 19–24.

[27] G. Glaspell, L. Fuoco, M. S. El-shall, V. Commonwealth, V. Uni, *J. Phys. Chem. B Lett.* **2005**, *109*, 17350–17355.

[28] G. Glaspell, H. M. a Hassan, A. Elzatahry, V. Abdalsayed, M. Samy El-Shall, *Top. Catal.* **2008**, *47*, 22–31.

[29] T. Hayashi, K. Tanaka, M. Haruta, *J. Catal.* **1998**, *178*, 566–575.

[30] M. Okumura, T. Akita, M. Haruta, *Catal. Today* **2002**, *74*, 265–269.

[31] G. Zhou, P. Wang, Z. Jiang, P. Ying, C. Li, *Chinese J. Catal.* **2011**, *32*, 27–30.

[32] K. Mori, T. Hara, T. Mizugaki, K. Ebitani, K. Kaneda, *J. Am. Chem. Soc.* **2004**, *126*, 10657–10666.

[33] A. Biffis, L. Minati, *J. Catal.* **2005**, *236*, 405–409.

[34] M. R. Knecht, D. B. Pacardo, *Anal. Bioanal. Chem.* **2010**, *397*, 1137–1155.

[35] G. Collins, M. Blömker, M. Osiak, J. D. Holmes, M. Bredol, C. O'Dwyer, *Chem. Mater.* **2013**, *25*, 4312–4320.

[36] Y. Huang, Z. Lin, R. Cao, *Chem. - A Eur. J.* **2011**, *17*, 12706–12712.

[37] S. Senkan, M. Kahn, S. Duan, A. Ly, C. Leidholm, *Catal. Today* **2006**, *117*, 291–296.

[38] M. J. Jacinto, P. K. Kiyohara, S. H. Masunaga, R. F. Jardim, L. M. Rossi, *Appl. Catal. A Gen.* **2008**, *338*, 52–57.

[39] S. Wang, X. He, L. Song, Z. Wang, *Synlett* **2009**, 447–450.

[40] H. Zhao, H. Song, L. Chou, *Inorg. Chem. Commun.* **2012**, *15*, 261–265.

[41] T. Mitsui, K. Tsutsui, T. Matsui, R. Kikuchi, K. Eguchi, *Appl. Catal. B Environ.* **2008**, *81*, 56–63.

[42] A. M. Silva, A. P. M. G. Barandas, L. O. O. Costa, L. E. P. Borges, L. V. Mattos, F. B. Noronha, *Catal. Today* **2007**, *129*, 297–304.

[43] G. Vitulli, M. Bernini, S. Bertozzi, E. Pitzalis, P. Salvadori, S. Coluccia, G. Martra, *Chem. Mater.* **2002**, *14*, 1183–1186.

[44] S. Hermes, M. K. Schröter, R. Schmid, L. Khodeir, M. Muhler, A. Tissler, R. W. Fischer, R. a. Fischer, *Angew. Chemie - Int. Ed.* **2005**, *44*, 6237–6241.

[45] D. C. Skelton, H. Wang, R. G. Tobin, D. K. Lambert, C. L. DiMaggio, G. B. Fisher, *J. Phys. Chem. B* **2001**, *105*, 204–209.

[46] Y. Lou, M. M. Maye, L. Han, J. Luo, C.-J. Zhong, *Chem. Commun.* **2001**, 473–474.

[47] A. Habrioux, E. Sibert, K. Servat, W. Vogel, K. B. Kokoh, N. Alonso-Vante, *J. Phys. Chem. B* **2007**, *111*, 10329–10333.

[48] P. Herna, J. L. Go, J. Sanza, M. a Pen, F. J. Garcı, *J. Phys. Chem. C* **2007**, *111*, 2913–2923.

[49] Q. Yu, W. Chen, Y. Li, M. Jin, Z. Suo, *Catal. Today* **2010**, *158*, 324–328.

[50] A. Parinyaswan, S. Pongstabodee, A. Luengnaruemitchai, *Int. J. Hydrogen Energy* **2006**, *31*, 1942–1949.

[51] J. L. Rousset, L. Stievano, F. J. Cadete Santos Aires, C. Geantet, a J. Renouprez, M. Pellarin, F. J. C. S. Aires, *J. Catal.* **2001**, *197*, 335–343.

[52] S. Albertazzi, G. Busca, E. Finocchio, R. Glöckler, A. Vaccari, *J. Catal.* **2004**, *223*, 372–381.

[53] W. Hou, N. A. Dehm, R. W. J. Scott, *J. Catal.* **2008**, *253*, 22–27.

[54] N. Dimitratos, A. Villa, D. Wang, F. Porta, D. Su, L. Prati, *J. Catal.* **2006**, *244*, 113–121.

[55] G. Li, J. Edwards, A. F. Carley, G. J. Hutchings, *Catal. Today* **2007**, *122*, 361–364.

[56] G. C. Bond, *Gold Nanoparticles for Physics, Chemistry and Biology*, Imperial College Press, London, **2012**.

[57] N. Zheng, G. D. Stucky, *J. Am. Chem. Soc.* **2006**, *128*, 14278–14280.

[58] S. Ertan, F. Şen, S. Şen, G. Gökağaç, *J. Nanoparticle Res.* **2012**, *14*, 922–934.

[59] J. Zhu, K. Kailasam, X. Xie, R. Schomaecker, A. Thomas, *Chem. Mater.* **2011**, *23*, 2062–2067.

[60] S. Opelt, S. Türk, E. Dietzsch, A. Henschel, S. Kaskel, E. Klemm, *Catal. Commun.* **2008**, *9*, 1286–1290.

References

[61] A. Barau, V. Budarin, A. Caragheorgheopol, R. Luque, D. J. Macquarrie, A. Prelle, V. S. Teodorescu, M. Zaharescu, *Catal. Letters* **2008**, *124*, 204–214.

[62] A. Sandoval, A. Gómez-Cortés, R. Zanella, G. Díaz, J. M. Saniger, *J. Mol. Catal. A Chem.* **2007**, *278*, 200–208.

[63] H. Choi, S. R. Al-Abed, S. Agarwal, D. D. Dionysiou, *Chem. Mater.* **2008**, *20*, 3649–3655.

[64] R. Zanella, S. Giorgio, C. H. Shin, C. R. Henry, C. Louis, *J. Catal.* **2004**, *222*, 357–367.

[65] H. Yin, C. Wang, H. Zhu, S. H. Overbury, S. Sun, S. Dai, *Chem. Commun.* **2008**, 4357–4359.

[66] R. Zanella, S. Giorgio, C. R. Henry, C. Louis, *J. Phys. Chem. B* **2002**, *106*, 7634–7642.

[67] B. L. Cushing, V. L. Kolesnichenko, C. J. O. Connor, **2004**, *104*, 3893–3946.

[68] D. Nagao, Y. Shimazaki, S. Saeki, Y. Kobayashi, M. Konno, *Colloids Surfaces A Physicochem. Eng. Asp.* **2007**, *302*, 623–627.

[69] E. R. Williams, R. M. Leithall, R. Raja, M. T. Weller, *Chem. Commun.* **2013**, 249–251.

[70] C. S. Hinde, S. Van Aswegen, G. Collins, J. D. Holmes, T. S. A. Hor, R. Raja, *Dalt. Trans.* **2013**, *42*, 12600–12605.

[71] Q. Huang, M. Ulutagay, P. a. Michener, S. J. Hwu, *J. Am. Chem. Soc.* **1999**, *121*, 10323–10326.

[72] C. S. Hinde, D. Ansovini, P. P. Wells, G. Collins, S. Van Aswegen, J. D. Holmes, T. S. A. Hor, R. Raja, *ACS Catal.* **2015**, *5*, 3807–3816.

[73] G. C. Bond, C. Louis, D. T. Thompson, *Catalysis by Gold*, Imperial College Press, London, **2006**.

[74] A. M. Gill, C. S. Hinde, R. K. Leary, M. E. Potter, A. Jouve, P. P. Wells, P. A. Midgley, J. M. Thomas, R. Raja, *ChemSusChem* **2016**, *9*, 423–427.

[75] D. I. Enache, J. K. Edwards, P. Landon, B. Solsona-Espriu, A. F. Carley, A. A. Herzing, M. Watanabe, C. J. Kiely, D. W. Knight, G. J. Hutchings, *Science (80-.).* **2006**, *311*, 362–365.

[76] G. J. Hutchings, *Catal. Today* **2007**, *122*, 196–200.

[77] A. L. Tarasov, L. M. Kustov, V. I. Isaeva, A. N. Kalenchuk, I. V. Mishin, G. I. Kapustin, V. I. Bogdan, *Kinet. Catal.* **2011**, *52*, 273–276.

[78] Y. Y. Fong, B. R. Visser, J. R. Gascooke, B. C. C. Cowie, L. Thomsen, G. F. Metha, M. A. Buntine, H. H. Harris, *Langmuir* **2011**, *27*, 8099–8104.

[79] C. S. Hinde, A. M. Gill, P. P. Wells, T. S. A. Hor, R. Raja, *Chempluschem* **2015**, *80*, 1226–1230.

[80] J. Scharschmidt, C. Mendoza-Frohn, H. Buysch, R. Klotzbücher, *Process for the Preparation of a Mixture of Cyclohexanone and Cyclohexanol*, **1995**, US5395976.

[81] A. Matsuura, T. Watanabe, *Method for Producing Cyclohexanone Compound*, **2013**, WO2014163080 A1.

[82] C. Gardner, J. F. Prescott, *Oxidation of Cyclohexane*, **1968**, US3365491.

[83] K. Takagi, T. Ishida, *Oxidation of Cyclohexane*, **1972**, US3644526.

[84] M. T. Musser, *Ullman's Encyclopedia of Industrial Chemistry, Volume 11*, Wiley-VCH Verlag GmbH, Weinheim, **2012**.

[85] O. Drossbach, *Oxidation of Cyclohexanol*, **1942**, US2285914.

[86] P. Ruiz, B. Delmon, Eds. , in *Vol. 72 Stud. Surf. Sci. Catal.*, Elsevier, Amsterdam, **1992**.

[87] A. Dhakshinamoorthy, H. Garcia, *Chem. Soc. Rev.* **2012**, *41*, 5262–5284.

[88] H. Liu, Y. Liu, Y. Li, Z. Tang, H. Jiang, *J. Phys. Chem. C* **2010**, *114*, 13362–13369.

[89] G. Franz, R. A. Sheldon, *Ullman's Encyclopedia of Industrial Chemistry, Volume 25*, Wiley-VCH Verlag GmbH, Weinheim, **2000**.

[90] A. Abad, A. Corma, H. García, *Chem. - A Eur. J.* **2008**, *14*, 212–222.

[91] Y. Zhu, J. Xu, M. Lu, *Catal. Commun.* **2014**, *48*, 78–84.

[92] L. Balbinot, U. Schuchardt, C. Vera, J. Sepúlveda, *Catal. Commun.* **2008**, *9*, 1878–1881.

[93] L. Chen, T. Zhou, L. Chen, Y. Ye, Z. Qi, H. Freund, K. Sundmacher, *Chem. Commun. (Camb).* **2011**, *47*, 9354–9356.

[94] K. Li, D. Zhou, J. Deng, X. Lu, Q. Xia, *J. Mol. Catal. A Chem.* **2014**, *387*, 31–37.

[95] F. Wang, R. Shi, Z. Liu, P. Shang, X. Pang, S. Shen, Z. Feng, C. Li, W. Shen, *ACS Catal.* **2013**, *3*, 890–894.

[96] D. Santhanaraj, C. Suresh, P. Vijayan, N. Venkatathri, K. Shanthi, *React. Kinet. Mech. Catal.* **2010**, *99*, 439–446.

[97] T. Wang, H. Shou, Y. Kou, H. Liu, *Green Chem.* **2009**, *11*, 562–568.

[98] J. Ni, W.-J. Yu, L. He, H. Sun, Y. Cao, H.-Y. He, K.-N. Fan, *Green Chem.* **2009**, *11*, 756–759.

[99] R. Raja, J. M. Thomas, M. Greenhill-Hooper, V. Doukova, *Chem. Commun.* **2007**, 1924–1926.

[100] H. Ji, T. Mizugaki, K. Ebitani, K. Kaneda, *Tetrahedron Lett.* **2002**, *43*, 7179–7183.

[101] K. Yamaguchi, N. Mizuno, *New J. Chem.* **2002**, *26*, 972–974.

References

[102] G. Chatel, C. Monnier, N. Kardos, C. Voiron, B. Andrioletti, M. Draye, *Appl. Catal. A Gen.* **2014**, *478*, 157–164.

[103] A. Romero, A. Santos, D. Escrig, E. Simón, *Appl. Catal. A Gen.* **2011**, *392*, 19–27.

[104] J. Taghavimoghaddam, G. P. Knowles, A. L. Chaffee, *J. Mol. Catal. A Chem.* **2013**, *379*, 277–286.

[105] A. M. Balu, C. S. K. Lin, H. Liu, Y. Li, C. Vargas, R. Luque, *Appl. Catal. A Gen.* **2013**, *455*, 261–266.

[106] H. Figueiredo, B. Silva, I. Kuźniarska-Biernacka, A. M. Fonseca, R. Medina, S. Rasmussen, M. A. Bañares, I. C. Neves, T. Tavares, *Chem. Eng. J.* **2014**, *247*, 134–141.

[107] H. Wang, W. Kong, W. Zhu, L. Wang, S. Yang, F. Liu, *Catal. Commun.* **2014**, *50*, 87–91.

[108] V. Mahdavi, S. Soleimani, *Mater. Res. Bull.* **2014**, *51*, 153–160.

[109] N. Jappar, Q. Xia, T. Tatsumi, *J. Catal.* **1998**, *180*, 132–141.

[110] B. Zhan, M. A. White, T. Sham, J. a Pincock, J. Doucet, K. V. R. Rao, K. N. Robertson, T. S. Cameron, M. Ii, C. Phen, **2003**, 2195–2199.

[111] R. L. Oliveira, K. Kiyohara, L. M. Rossi, *Green Chem.* **2010**, *12*, 144–149.

[112] B. M. Nagaraja, A. H. Padmasri, P. Seetharamulu, K. Hari Prasad Reddy, B. David Raju, K. S. Rama Rao, *J. Mol. Catal. A Chem.* **2007**, *278*, 29–37.

[113] W. Li, A. Wang, X. Liu, T. Zhang, *Appl. Catal. A Gen.* **2012**, *433-434*, 146–151.

[114] Y. Chang, T. Jiang, B. Han, L. Gao, R. Zhang, Z. Liu, W. Wu, *Ind. Eng. Chem. Res.* **2003**, *42*, 6384–6388.

[115] G. Ranga Rao, S. K. Meher, B. G. Mishra, P. H. K. Charan, *Catal. Today* **2012**, *198*, 140–147.

[116] Y. Hong, X. Yan, X. Liao, R. Li, S. Xu, L. Xiao, J. Fan, *Chem. Commun.* **2014**, *50*, 9679–9682.

[117] A. Buonerba, C. Cuomo, S. Ortega Sánchez, P. Canton, A. Grassi, *Chem. - A Eur. J.* **2012**, *18*, 709–715.

[118] A. Corma, P. Esteve, A. Martínez, *J. Catal.* **1996**, *161*, 11–19.

[119] Z. Yang, J. Li, X. Yang, X. Xie, Y. Wu, *J. Mol. Catal. A Chem.* **2005**, *241*, 15–22.

[120] M. Popova, Á. Szegedi, K. Lázár, A. Dimitrova, *Catal. Letters* **2011**, *141*, 1288–1296.

[121] G. K. Reddy, P. K. Rao, *Catal. Letters* **1997**, *45*, 93–96.

[122] H. Zou, R. Wang, J. Dai, Y. Wang, X. Wang, Z. Zhang, S. Qiu, *Chem. Commun.* **2015**, *51*, 14601–14604.

[123] Y. Du, Q. Wang, X. Liang, Y. He, J. Feng, D. Li, *J. Catal.* **2015**, *331*, 154–161.

[124] Y. Zhu, Y. Cao, X. Sun, X. Wang, *Sensors (Basel).* **2013**, *13*, 5286–5301.

[125] S. Tang, S. Vongehr, Z. Zheng, H. Ren, X. Meng, *Nanotechnology* **2012**, *23*, 255606–255616.

[126] J. E. Readman, A. Olafsen, Y. Larring, R. Blom, *J. Mater. Chem.* **2005**, *15*, 1931–1937.

[127] C. M. Chen, J. M. Jehng, *Catal. Letters* **2003**, *85*, 73–80.

[128] R. M. Rioux, H. Song, J. D. Hoefelmeyer, P. Yang, G. a Somorjai, *J. Phys. Chem. B* **2005**, *109*, 2192–2202.

[129] M. F. Lengke, M. E. Fleet, G. Southam, *Langmuir* **2006**, *22*, 7318–7323.

[130] A. Clearfield, D. S. Thakur, *J. Catal.* **1980**, *65*, 185–194.

[131] R. Srinivasan, *Science (80-.).* **1986**, *234*, 559–565.

[132] M. C. Tsai, C. M. Friend, E. L. Muetterties, *J. Am. Chem. Soc.* **1982**, *104*, 2539–2543.

[133] O. Alekseeva, M. Konstantinova, S. Rasumovskii, *Heteroat. Chem.* **2008**, *19*, 661–666.

[134] N. S. Kus, C. Kazaz, *Asian J. Chem.* **2008**, *20*, 1226–1230.

[135] A. A. Taherpour, H. R. Mansuri, *Turkish J. Chem.* **2005**, *29*, 317–320.

[136] P. S. Starcher, D. Trecker, J. E. McKeon, *Oxidation of Lactams to Cyclic Imides*, **1971**, US3621012.

[137] A. R. Doumaux, *Oxidation of Lactams to Cyclic Imides*, **1972**, US3634406.

[138] A. R. Doumaux, J. E. McKeon, D. J. Trecker, *J. Am. Chem. Soc.* **1969**, *91*, 3992–3993.

[139] A. R. Doumaux, D. J. Trecker, *J. Org. Chem.* **1970**, *35*, 2121–2125.

[140] C. Ngamcharussrivichai, P. Wu, T. Tatsumi, *J. Catal.* **2005**, *235*, 139–149.

[141] S. H. Newland, W. Sinkler, T. Mezza, S. R. Bare, M. Carravetta, I. M. Haies, A. Levy, S. Keenan, R. Raja, *ACS Catal.* **2015**, *5*, 6587–6593.

[142] A. Corma, L. T. Nemeth, M. Renz, S. Valencia, *Nature* **2001**, *412*, 423–425.

Appendix

Sample	Abs Sc	N	R / Å	$2\sigma^2$ / Å^2	E_f / eV	R_{factor}
Pt/CuClP 150 °C	Pt – Cl	3.7 (2)	2.320 (5)	0.0027 (3)	9.5 (8)	0.012
	Pt – Pt	3.4 (5)	2.768 (7)	0.0056 (5)		
Pt/CuClP 175 °C	Pt – Cl	0.8 (1)	2.31 (9)	0.0026 (8)	7.9 (7)	0.006
	Pt – Pt	8.9 (3)	2.76 (2)	0.0059 (1)		
Pt/CuClP 200 °C	Pt – Cl	0.4 (1)	2.32 (2)	0.003 (2)	7.6 (6)	0.006
	Pt – Pt	9.6 (4)	2.760 (3)	0.0059 (2)		

Figure A. 1: EXAFS fitting parameters for the Pt/CuClP fits displayed in Figure 1.10b, reproduced from Gill *et al*.[74].

Sample	Abs Sc	N	R / Å	$2\sigma^2$ / Å^2	E_f / eV	R_{factor}
Au/CuClP 150 °C	Au – Cl	3.7 (1)	2.287 (4)	0.0027 (2)	9.9 (6)	0.004
Au/CuClP 200 °C	Au – Cl	2.24 (7)	2.269 (4)	0.0028 (3)	7.3 (7)	0.009
Au/CuClP 250 °C	Au – Cl	3.1 (1)	2.282 (5)	0.0029 (3)	9.4 (9)	0.010

Figure A. 2: EXAFS fitting parameters for the Au/CuClP fits displayed in Figure 1.11b, reproduced from Gill *et al*.[74].

Sample	Abs Sc	N	R / Å	$2\sigma^2$ / Å^2	E_f / eV	R_{factor}
Pd/CuClP 150 °C	Pd – Cl	4.2 (1)	2.322 (5)	0.0028 (4)	5.2 (7)	0.007
	Pd – Pd	0.3 (2)	2.76 (3)	0.003 (3)		
Pd/CuClP 175 °C	Pd – Cl	3.2 (3)	2.35 (1)	0.003 (1)	4 (2)	0.041
	Pd – Pd	0.9 (4)	2.77 (3)	0.003 (2)		
Pd/CuClP 200 °C	Pd – Cl	3.4 (3)	2.35 (1)	0.0027 (7)	13 (1)	0.025
	Pd – Pd	0.9 (4)	2.77 (2)	0.002 (2)		

Figure A. 3: EXAFS fitting parameters for the Pd/CuClP fits displayed in Figure 1.12b, reproduced from Gill *et al*.[74].

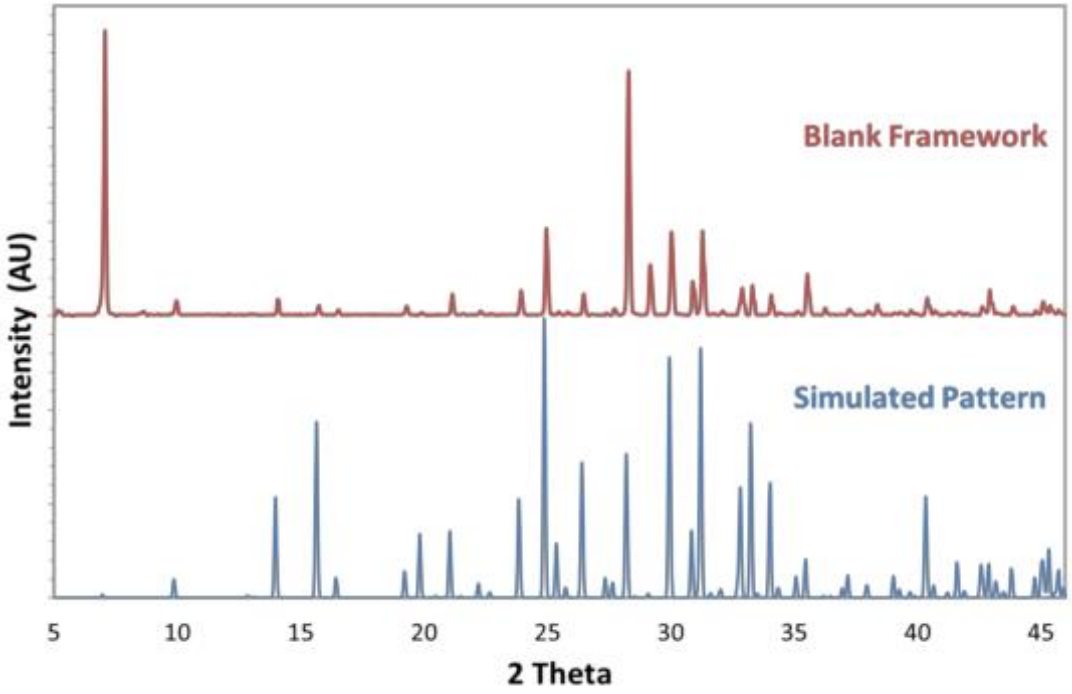

Figure A. 4: Simulated PXRD pattern (blue line) and experimental PXRD of the blank framework (red line); reproduced from Hinde *et al*.[70].

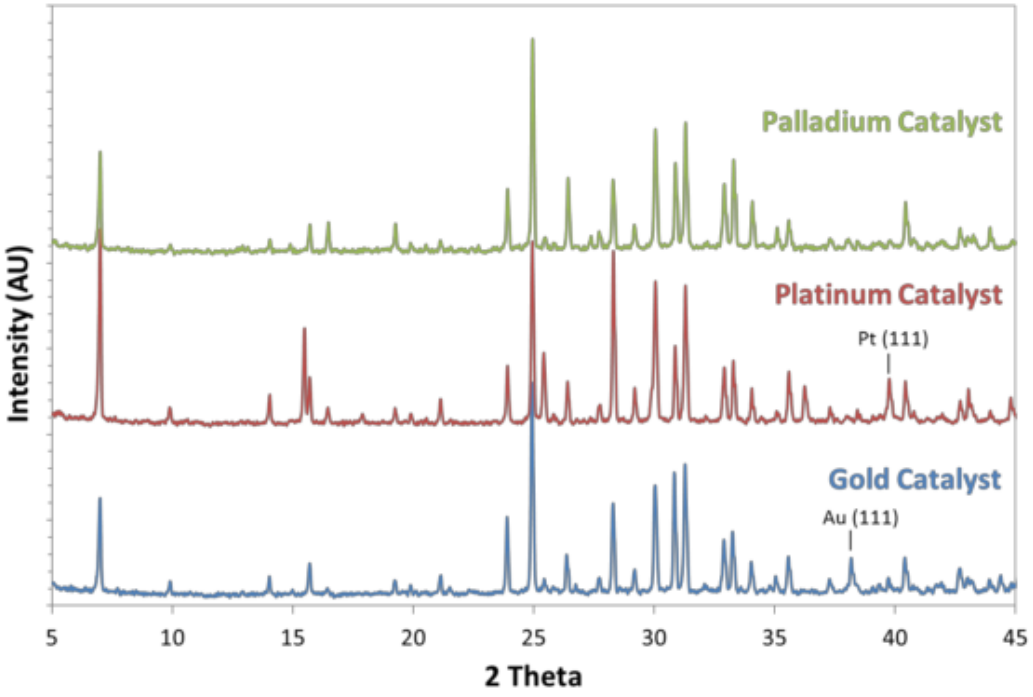

Figure A. 5: PXRD patterns of Au/CuClP (blue line), Pt/CuClP (red line) and Pd/CuClP (green line) materials calcined at 500 °C; reproduced from Hinde *et al*.[70].

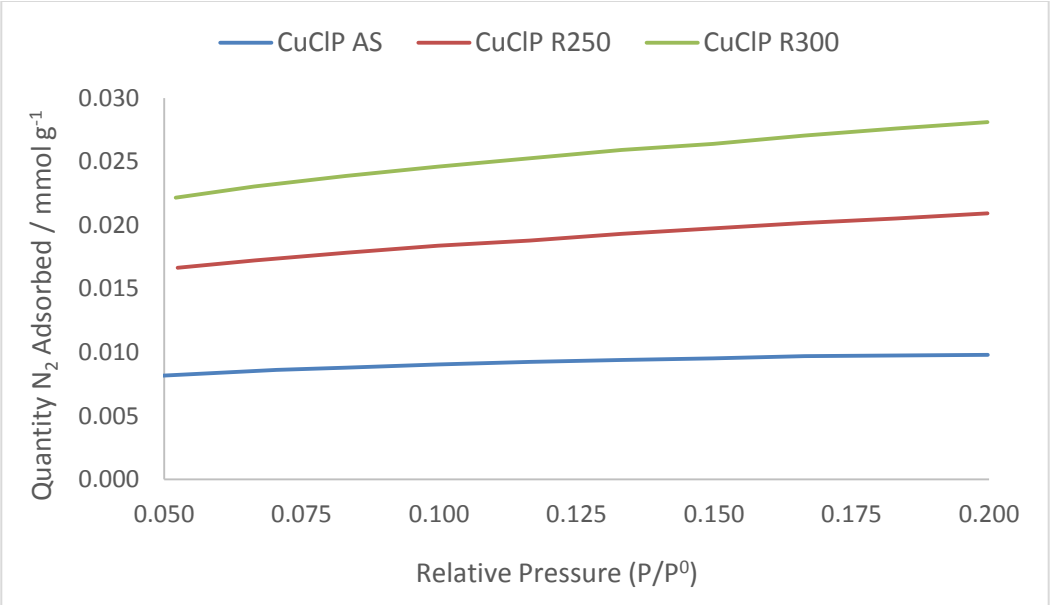

Figure A. 6: BET N_2 adsorption isotherms for as-synthesised and reduced CuClP materials; reduced materials activated at 250 °C (R250) and 300 °C (R300).

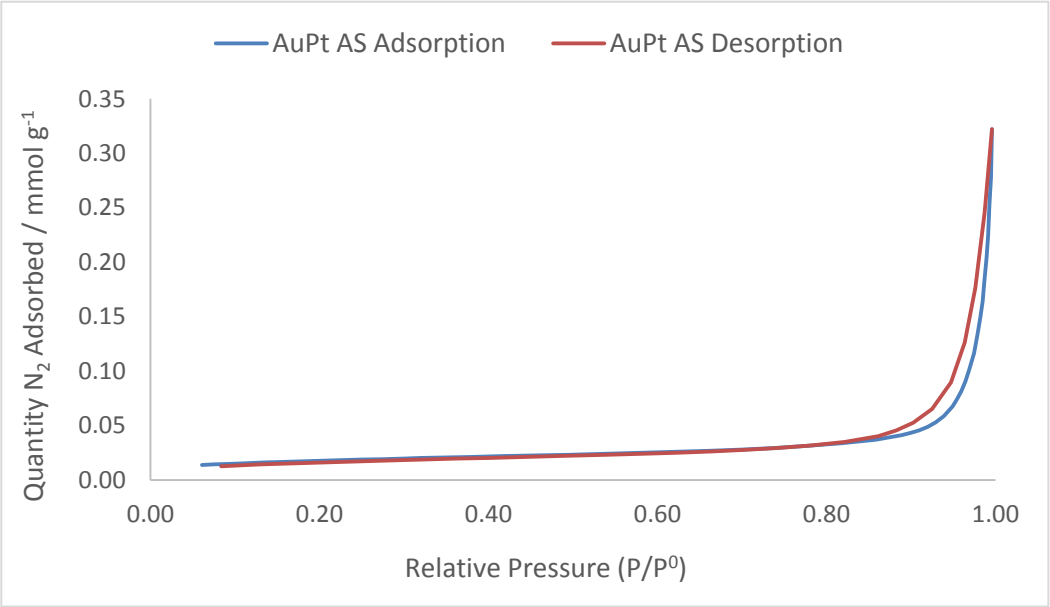

Figure A. 7: BET N_2 adsorption (blue) and desorption (orange) isotherms for the as-synthesised (AS) AuPt/CuClP material.

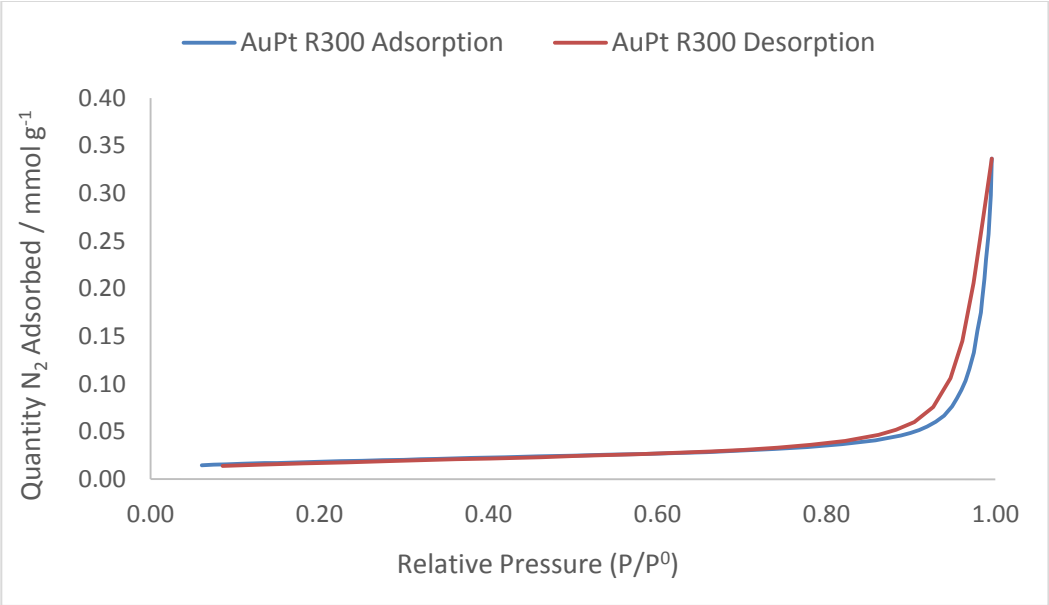

Figure A. 8: BET N_2 adsorption (blue) and desorption (orange) isotherms for the AuPt/CuClP material reduced at 300 °C (R300).

Sample	Activation Temperature / °C	ICP Loading		
		Au	Pt	Pd
Au/CuClP	200	3.5*	-	-
	250	3.5*		
Pt/CuClP	250	-	3.79	-
	300		3.5*	
Pd/CuClP	150	-	-	3.5*
	200			3.5*
AuPt/CuClP	150	3.5*	3.5*	-
	200	3.44	3.26	
	250	3.59	3.49	
	300	3.59	3.41	
	350	4.65	4.18	
PtPd/CuClP	150	-	3.01	2.15
	200		3.19	2.18
AuPd/CuClP	150	2.01	-	2.33
	200	3.03		2.35

Figure A. 9: ICP loadings for the monometallic and bimetallic CuClP materials; * no ICP data, estimated loading based on synthesis amounts.

Appendix

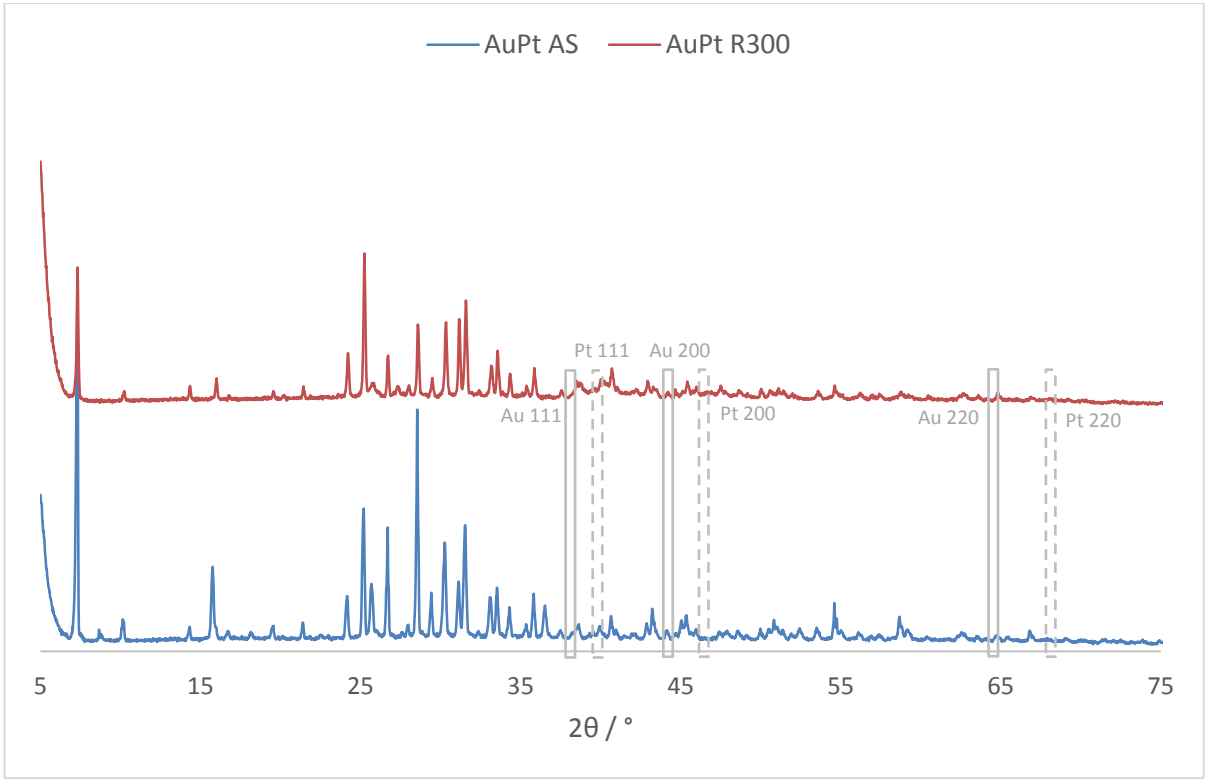

Figure A. 10:PXRD patterns of as-synthesised (AS) AuPt/CuClP and a sample reduced at 300 °C (R300); Au and Pt nanoparticle regions indicated by solid and dashed grey lines.

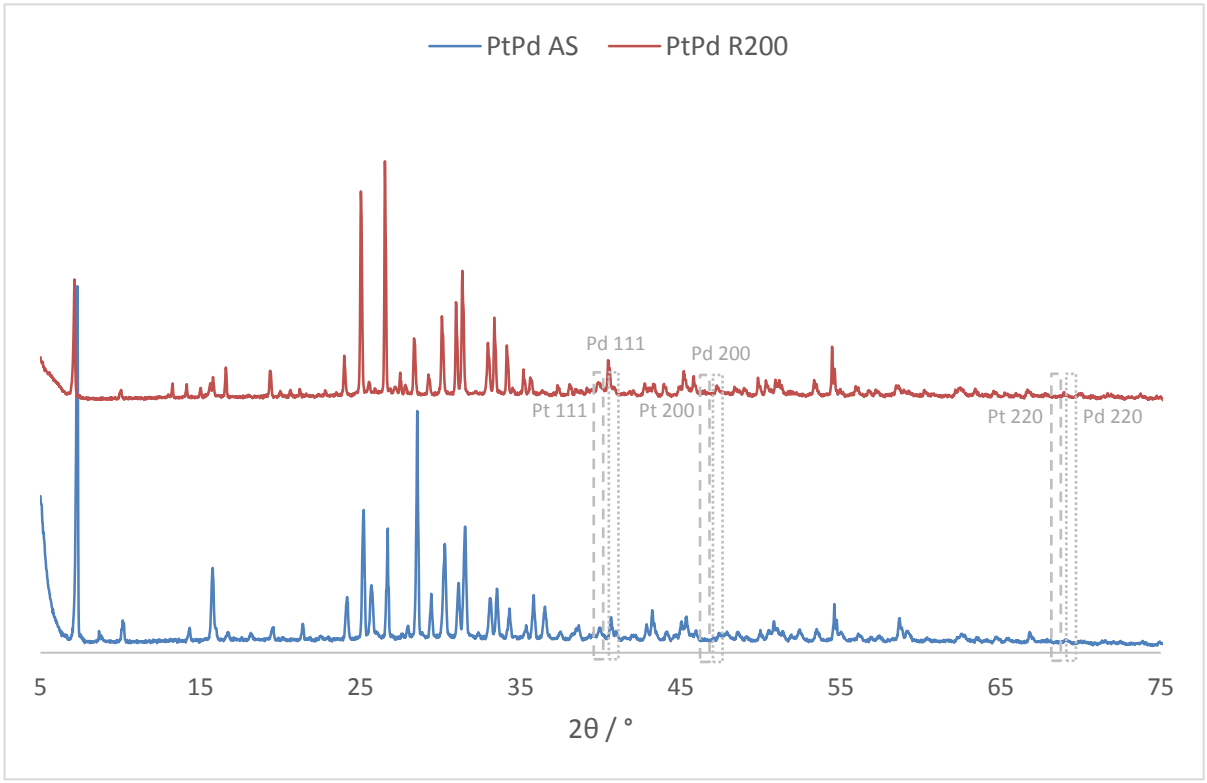

Figure A. 11:PXRD patterns of as-synthesised (AS) PtPd/CuClP and a sample reduced at 200 °C (R200); Pt and Pd nanoparticle regions indicated by dashed and dotted grey lines.

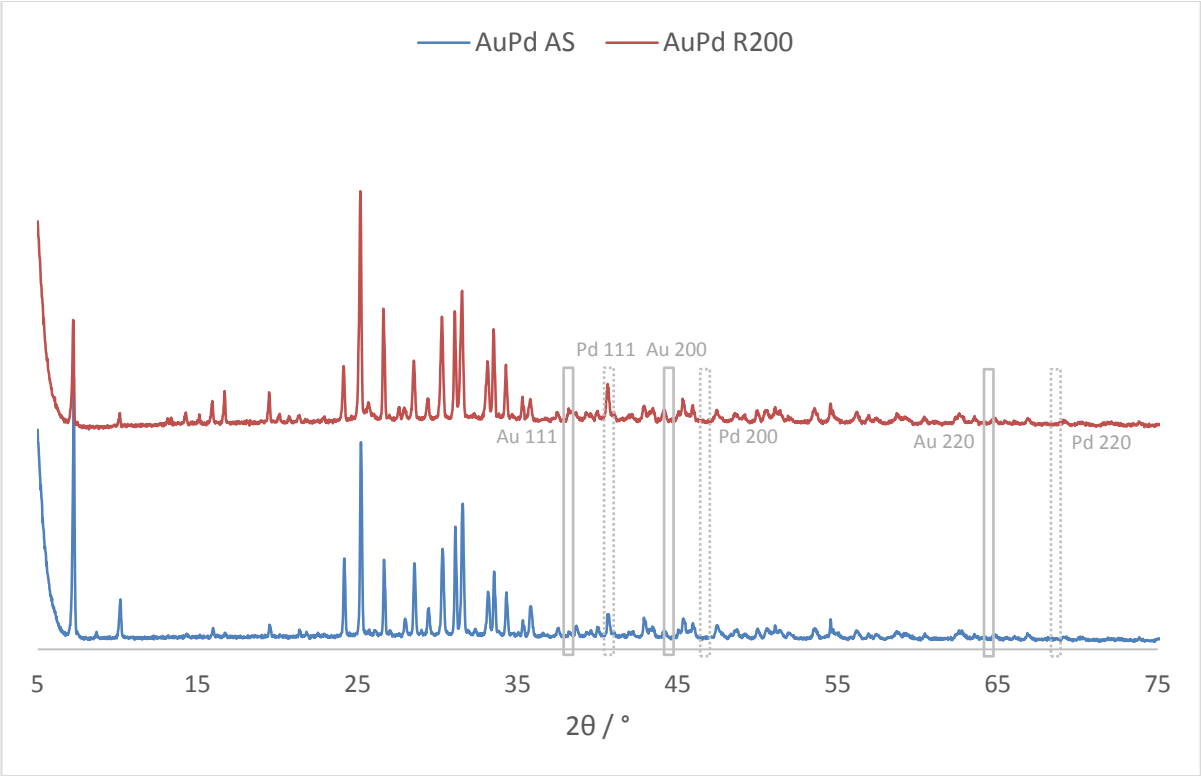

Figure A. 12:PXRD patterns of as-synthesised (AS) AuPd/CuClP and a sample reduced at 200 °C (R200); Au and Pd nanoparticle regions indicated by solid and dotted grey lines.

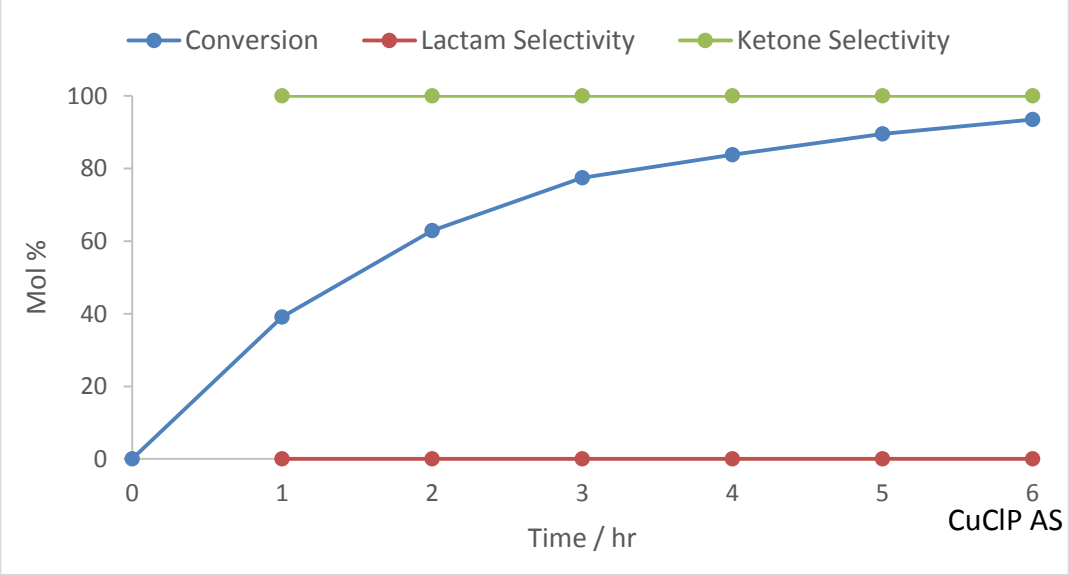

Figure A. 13:Conversion and selectivity plot for the Beckmann rearrangement of cyclohexanone oxime using as-synthesised CuClP; lactam is caprolactam; ketone is cyclohexanone; 0.1 g cyclohexanone oxime, 0.1 g catalyst, 0.1 g chlorobenzene, 20 mL acetonitrile, N_2 atmosphere reflux, 130 °C.

Appendix

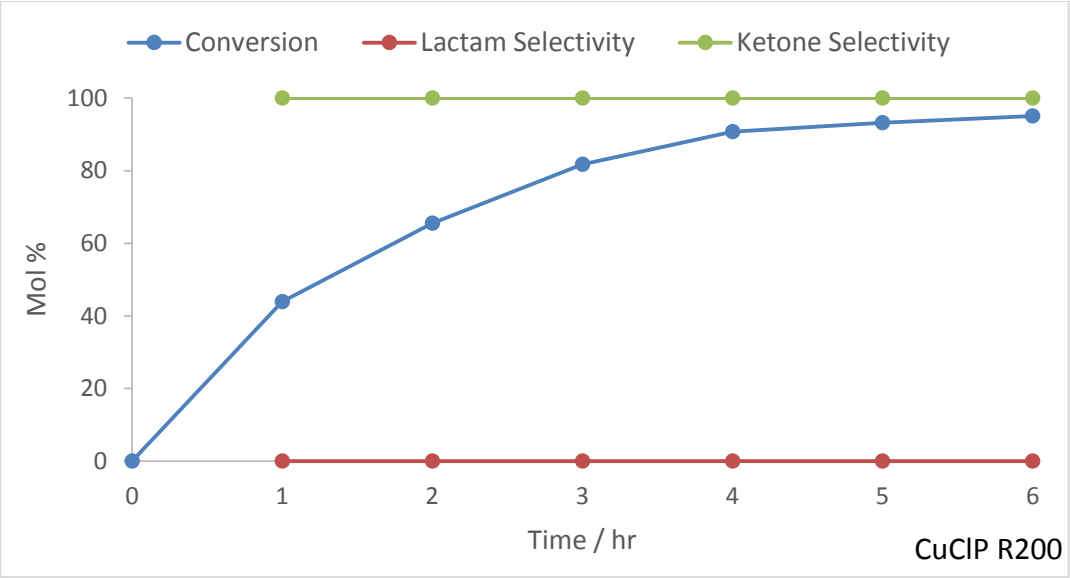

Figure A. 14: Conversion and selectivity plot for the Beckmann rearrangement of cyclohexanone oxime using CuClP reduced at 200 °C; lactam is caprolactam; ketone is cyclohexanone; 0.1 g cyclohexanone oxime, 0.1 g catalyst, 0.1 g chlorobenzene, 20 mL acetonitrile, N_2 atmosphere reflux, 130 °C.

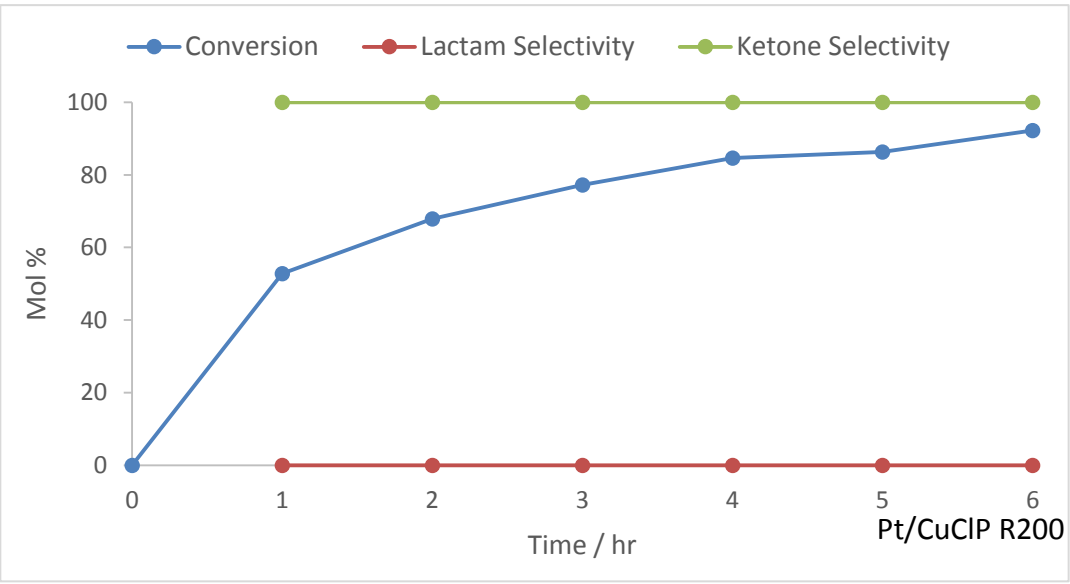

Figure A. 15: Conversion and selectivity plot for the Beckmann rearrangement of cyclohexanone oxime using Pt/CuClP reduced at 200 °C; lactam is caprolactam; ketone is cyclohexanone; experiment conducted by S. Newland; 0.1 g cyclohexanone oxime, 0.1 g catalyst, 0.1 g chlorobenzene, 20 mL acetonitrile, N_2 atmosphere reflux, 130 °C.

Exp. #	Catalyst	Activation Temperature / °C	Reaction Temperature / °C	WHSV / hr^{-1}	Air Flow Rate / mL min^{-1}	Reaction Time / hr	Conversion / mol %	Cyclohexanone Selectivity / %	Cyclohexanone Yield / %	Mass Balance / %	TOF / hr^{-1}
114	None	N/A	200	N/A	25	3	0	0	0	162	0
137	CuClP	-	200	2.15	25	3	0	0	0	121	0
138		300	200	2.14	25	3	0	0	0	130	0
135	3.5 wt. % Au/CuClP	250	200	1.90	25	3	0	0	0	132	0
142		300	200	2.15	25	3	0	0	0	116	0
125	3.5 wt. % Pt/CuClP	200	200	2.10	25	3	59	> 99	68	116	63
136		250	200	2.13	25	3	69	> 99	82	118	82
141	3.5 wt. % Pd/CuClP	150	200	2.06	25	3	0	0	0	141	0
143		200	200	2.11	25	3	0	0	0	94	0

Figure A. 16: Catalytic parameters and conditions for the screening of the monometallic CuClP catalysts and blanks reactions in the aerobic oxidation of KA-oil.

Appendix

Exp. #	Catalyst	Activation Temperature / °C	Reaction Temperature / °C	WHSV / hr^{-1}	Air Flow Rate / mL min^{-1}	Reaction Time / hr	Conversion / mol %	Cyclohexanone Selectivity / %	Cyclohexanone Yield / %	Mass Balance† / %	TOF / hr^{-1}
27	7 wt. % Pt/CuClP	200	180	1.83	25	5	50	> 99	52	105	25
			190				58	> 99	61	105	29
			200				60	> 99	60	101	30
			210				57	> 99	60	106	28
			220				57	> 99	62	110	28
28	7 wt. % Pt/CuClP	200	200	1.80	10	5	0.5	> 99	0.5	126 (100)	0
					20		42	> 99	48	115 (91)	21
					25		65	> 99	71	109 (87)	32
					30		63	> 99	64	101 (80)	31
					40		75	> 99	71	95 (75)	37
29	7 wt. % Pt/CuClP	200	200	0.61	25	5	96	> 99	59	61	48
				1.22			81	> 99	76	94	41
				1.83			66	> 99	67	102	33
				2.44			53	> 99	57	108	27
				3.05			43	> 99	47	111	21

Figure A. 17:Catalytic parameters and conditions for the optimisation of the aerobic oxidation of KA-oil; † normalised mass balance in brackets, calculated using a zero point sample.

Exp. #	Catalyst	Activation Temperature / °C	Reaction Temperature / °C	WHSV / hr^{-1}	Air Flow Rate / mL min^{-1}	Reaction Time / hr	Conversion / mol %	Cyclohexanone Selectivity / %	Cyclohexanone Yield / %	Mass Balance / %	TOF / hr^{-1}
131		-	200	1.90	25	3	0	> 99	0	122	0
76		150	200	2.15	25	3	0	> 99	0	130	0
78	7 wt. %	200	200	2.13	25	3	48	> 99	56	118	30
79	AuPt/CuClP	250	200	2.12	25	3	58	> 99	73	127	34
35		300	200	2.12	25	3	89	> 99	63	71	53
68		350	200	2.37	25	3	61	> 99	67	109	32
41	7 wt. %	150	200	1.87	25	3	11	> 99	13	121	6
42	PtPd/CuClP	200	200	1.84	25	3	63	> 99	72	115	31
84	7 wt. %	150	200	2.01	25	3	0	0	0	125	0
85	AuPd/CuClP	200	200	2.16	25	3	0	0	0	127	0

Figure A. 18:Catalytic parameters and conditions for the screening of the bimetallic CuClP catalysts in the aerobic oxidation of KA-oil.

Appendix

Exp. #	Catalyst	Activation Temperature / °C	Reaction Temperature / °C	WHSV / hr^{-1}	Air Flow Rate / mL min^{-1}	Reaction Time / hr	Conversion / mol %	Cyclohexanone Selectivity / %	Cyclohexanone Yield / %	Mass Balance / %	TOF / hr^{-1}
135	3.5 wt. % Au/CuClP	250	200	1.90	25	3	0	0	0	132	0
136	3.5 wt. % Pt/CuClP	250	200	2.13	25	3	69	> 99	82	118	82
79	7 wt. % AuPt/CuClP	250	200	2.12	25	3	58	> 99	73	127	34
133	3.5 wt. % Au/CuClP + 3.5 wt. % Pt/CuClP	Mix then R250	200	2.25	25	3	65	> 99	85	129	41
134	3.5 wt. % Au/CuClP + 3.5 wt. % Pt/CuClP	R250 then mix	200	2.23	25	3	61	> 99	75	124	38

Figure A. 19: Catalytic parameters and conditions for the physical mixture test of the Au/CuClP, Pt/CuClP and AuPt/CuClP materials in the aerobic oxidation of KA-oil.

Exp. #	Catalyst	Reaction Temperature / °C	WHSV / hr^{-1}	Air Flow Rate / mL min^{-1}	Reaction Time / hr	Conversion / mol %	Selectivity / %			Cyclohexanone Yield / %	Mass Balance / %	TOF / hr^{-1}
							Cyclohexanone	Cyclohexene	Benzene			
102	Pd/TiO_2 (1 wt. %, 1 °C)	200	1.80	25	3	57	80	5	15	51	77	109
103	Pd/TiO_2 (1 wt. %, 75 °C)	200	1.80	25	3	36	80	7	13	30	70	69
106	Pt/TiO_2 (1 wt. %, 1 °C)	200	1.81	25	3	19	95	5	0	32	110	66
107	AuPt/TiO_2 (1 wt. %, 1 °C)	200	1.79	25	3	8	94	6	0	21	122	30
108	AuPd/TiO_2 (1 wt. %, 1 °C)	200	1.79	25	3	6	95	5	0	19	130	17
104	Au/TiO_2 (1 wt. %, 1 °C)	200	1.81	25	3	4	97	3	0	17	123	14
105	Au/TiO_2 (1 wt. %, 75 °C)	200	1.79	25	3	4	96	4	0	15	107	16

Figure A. 20:Catalytic parameters and conditions for the screening of the TiO_2-supported nanoparticle catalysts in the aerobic oxidation of KA-oil; catalysts provided by S. Rogers from the UK Catalysis Hub at the Research Complex at Harwell, Oxford.

Appendix

Exp. #	Catalyst	Activation Temperature / °C	Reaction Temperature / °C	WHSV / hr^{-1}	Air Flow Rate / mL min^{-1}	Reaction Time / hr	Conversion / mol %	Cyclohexanone Selectivity / %	Cyclohexanone Yield / %	Mass Balance / %	TOF / hr^{-1}
35	7 wt. % AuPt/CuClP	300	200	2.12	25	3	89	> 99	63	71	53
136	3.5 wt. % Pt/CuClP	250	200	2.13	25	3	69	> 99	82	118	82
42	7 wt. % PtPd/CuClP	200	200	1.84	25	3	63	> 99	72	115	31
142	3.5 wt. % Au/CuClP	300	200	2.15	25	3	0	0	0	116	0
143	3.5 wt. % Pd/CuClP	200	200	2.11	25	3	0	0	0	94	0
85	7 wt. % AuPd/CuClP	200	200	2.16	25	3	0	0	0	127	0

Figure A. 21:Catalytic parameters and conditions for the screening of the CuClP catalysts in the aerobic oxidation of KA-oil.

Exp. #	Catalyst	Activation Temperature / °C	Reaction Temperature / °C	Reaction Time / hr	Oxidant	Solvent	Conversion / mol %
TJN43c	-	N/A	80	24	TBHP	*t*BuOH	2
TJN53a	7 wt. % Au/CuClP	150	80	24	TBHP	*t*BuOH	17
TJN53b		250	80	24	TBHP	*t*BuOH	22
TJN53c		350	80	24	TBHP	*t*BuOH	60
TJN59a	7 wt. % Pt/CuClP	150	80	24	TBHP	*t*BuOH	31
TJN59b		175	80	24	TBHP	*t*BuOH	31
TJN59c		250	80	24	TBHP	*t*BuOH	33
TJN54a	7 wt. % Pd/CuClP	150	80	24	TBHP	*t*BuOH	23
TJN54b		175	80	24	TBHP	*t*BuOH	39
TJN58a	7 wt. % AuPt/CuClP	200	80	24	TBHP	*t*BuOH	45
TJN58b	7 wt. % AuPd/CuClP	200	80	24	TBHP	*t*BuOH	44
TJN58c	7 wt. % PtPd/CuClP	200	80	24	TBHP	*t*BuOH	41

Figure A. 22: Catalytic parameters and conditions for the screening the CuClP catalysts for the oxidation of valerolactam; experiments conducted by T. Nimmo.

Exp. #	Catalyst	Activation Temperature / °C	Reaction Temperature / °C	Reaction Time / hr	Conversion / mol %	Selectivity / %	
						Caprolactam	Cyclohexanone
90	CuClP	-	130	6	94	0	> 99
91		200	130	6	95	0	> 99
SN7575_36†	7 wt. % Pt/CuClP	200	130	6	92	0	> 99

Figure A. 23:Catalytic parameters and conditions for the screening the CuClP catalysts for the Beckmann rearrangement of cyclohexanone oxime; † experiment conducted by S. Newland.

Exp. #	Catalyst	Activation Temperature / °C	Reaction Temperature / °C	Reaction Time / hr	Oxidant	Conversion / mol %	Cyclohexyl Lactone Selectivity / %
111	-	N/A	90	24	H_2O_2	0	0
112	CuClP	200	90	24	H_2O_2	0	0

Figure A. 24:Catalytic parameters and conditions for the screening the CuClP catalysts for the Baeyer-Villiger of cyclohexanone